Binder-free Tin (IV) Oxide Coated Vertically Aligned Carbon Nanotubes as Anode for Lithium-ion Batteries

Arun Thapa [a, c], Amin Rabiei Baboukani [b], Prahald Siwakoti [d], Katherine L. Jungjohann [e], Chinaza E. Nwanno [a], Jiandi Zhang [d], Chunlei Wang [b], Hongwei Gao [c], Wenzhi Li [a,*]

[a] *Department of Physics, Florida International University, Miami, FL 33199, USA*
[b] *Department of Mechanical and Materials Engineering, Florida International University, Miami, FL, 33174, USA*
[c] *Department of Electrical & Computer Engineering, Montana State University, Bozeman, MT 59717, United States*
[d] *Department of Physics & Astronomy, Louisiana State University, Baton Rouge, LA 70803, USA*
[e] *Center for Integrated Nanotechnologies, Sandia National Laboratories, Albuquerque, NM 87185, United States*

Abstract

Despite the tremendous potential of tin oxide (SnO_2) as an anode material, irreversible capacity loss due to the sluggish kinetics and structural pulverization as a result of the substantial volume alteration during redox reactions limits its use in lithium-ion batteries. The typical layered design of an electrode consisting of binder and conductive additive can lower the practical capacity of high-capacity electrode materials. We synthesized a binder and conductive additive-free, self-standing core-shell vertically-aligned carbon nanotubes (VACNTs)-SnO_2 anode (SnO_2-VACNTs) on 3D nickel foam using plasma-enhanced chemical vapor deposition and wet chemical method. The SnO_2-VACNTs exhibited excellent cyclability with a specific capacity of 1512 mAh g^{-1} at 0.1 A g^{-1} after 100 cycles and 800 mAh g^{-1} at 1 A g^{-1} after 200 cycles. The ultra-fine SnO_2 particles (< 5 nm) shortened the Li^+ diffusion paths into the bulk electrode and alleviated the volume alteration by lowering the strains during the redox reactions. Also, proper inter-tube distance between individual SnO_2-VACNTs buffered the volume instability and offered better electrolyte accessibility. Direct connection of VACNTs with the current collector ensured an uninterrupted electron conducting path between the current collector and active material, thus offering more efficient charge transportation kinetics at the electrode/electrolyte interfaces.

Keywords:

Lithium-ion batteries (LIBs); Vertically aligned CNTs; SnO_2 nanoparticles; Binder-free anode; Electrochemical Impedance Spectroscopy (EIS).

***Corresponding author:** Tel: +1 (305)348-7257**, E-mail:** Wenzhi.Li@fiu.edu (Wenzhi Li)

1. Introduction

The importance of lithium-ion batteries (LIBs) has increased ever since the commercialization of LIB comprised of lithium cobalt oxide ($LiCoO_2$) cathode paired with hard-carbon (C) anode by Sony Inc. in 1991 [1] due to their high energy and power density, broader operating temperature range, low self-discharge rate, and an absence of memory effect [2, 3]. Nonetheless, the ever-increasing use of LIBs in household appliances to sophisticated modern devices, including but not limited to electric vehicles (EVs), demands novel LIB electrodes with improved electrochemical properties and performances suitable for delivering high energy and power densities with negligible safety issues. Most commercial LIBs comprise graphite as an active anode material, which has a theoretical capacity of 372 mAh g^{-1} [4, 5]. However, the state-of-the-art LIBs have already attained the maximum specific capacity of graphite anodes and hence do not offer any significant improvement in energy density. Therefore, an alternate anode to the graphite is essential for high-performing LIBs.

Metal oxides such as tin oxide (SnO_2) [6], iron oxide (Fe_2O_3) [7], cobalt oxide (Co_3O_4) [8], copper oxide (CuO) [9], iron titanium oxide (Fe_2TiO_5) [10], and heterostructured nickel-iron oxide ($NiFe_2O_4/Fe_{0.64}Ni_{0.36}$) [11] are regarded as promising candidates to substitute the commercial graphite anode because of their high theoretical capacity. Among them, SnO_2 has attracted much attention recently due to its impressive theoretical specific capacity of 1493 mAh g^{-1} [12], cost-effectiveness, and good environmental compatibility. The Li^+ storage mechanism of SnO_2 comprises two stages. First, upon initial charge (conversion reaction), SnO_2 transforms to Sn and Li_2O according to the following reaction [13].

$$SnO_2 + 4Li^+ + 4e^- \rightarrow Sn + 2Li_2O \tag{1}$$

Subsequent lithiation of the SnO_2 (alloying reaction) corresponds to the following reversible phase transformation reactions [13].

$$Sn + xLi^+ + xe^- \leftrightarrow Li_xSn \qquad (0 \leq x \leq 4.4) \tag{2}$$

The first reaction (**Eq. 1**) is considered to be electrochemically irreversible. Hence, the maximum capacity of the SnO_2 is challenging to achieve. Some reports [14-16] suggested that the conversion reaction can become partially reversible if the SnO_2 size is reduced to less than 10 nm, while others [17, 18] reported that the SnO_2 nanoparticles are electrochemically irreversible. These findings indicate that the nano size of the SnO_2 particles is not solely responsible for the reversibility and cannot ensure a maximum reversible capacity. It is important to recognize other key factors closely linked to the electrochemical reactions that can facilitate optimum Li^+ storage; for example, creating an uninterrupted electron conducting path between the current collector and the active material can be a key to achieving high capacity, excellent rate capability, and cycling life. An easy access to electrolyte for the active material during lithiation/delithiation is another important factor affecting the Li^+ storage capacity of the active material. It is reported that nanoporous carbon matrix used as additives in metal oxide electrodes played important roles in rate capability and cycling life because of its high conductivity and its ability to facilitate easy electrolyte distribution due to the nanoporous structure [19, 20].

Carbon nanotubes (CNTs) are regarded as remarkable additive materials due to their excellent electrical and thermal conductivity for improving energy conversion, storage capacities, and charge transferability of active materials [21]. Furthermore, CNTs, including carbon nanofibers, have also been credited as excellent anode materials due to their one-dimensional tubular morphology, large surface area, short Li^+ diffusion path, and high electrical and thermal conductivity [22-25]. Moreover, due to their tubule structure and high flexibility, CNTs can be excellent hosts for high-capacity active materials. For instance, nanoparticles, including SnO_2, can be coated on the CNT's outer wall, creating a core (CNTs)-shell (layer of SnO_2) structure (SnO_2-CNTs) [26, 27]. Due to this unique structure, SnO_2-CNTs core-shell can absorb considerable stress resulting from active material pulverization during the lithiation/delithiation procedure. Several reports have shown excellent Li^+ storage properties of SnO_2-CNTs composite nanomaterial as the anode of LIBs [28-30]. However, the conventional bilayer design of the electrode, where a binder is used to glue active materials to a current collector, limits achieving the maximum capacity of SnO_2 electrodes. Reports have shown that the layered design of the LIB anode can reduce the practical capacity by ~47% [31]. Therefore, besides limiting the SnO_2 size below the critical threshold (<10 nm) and understanding the subsequent structural evolution during the electrochemical reaction, the electrode material's uninterrupted electron conducting path and high electrolyte accessibility are essential in achieving the maximum reversible capacity of SnO_2 and hence for the future commercialization of SnO_2-based anodes.

It is reported that tin (Sn), germanium (Ge), and silicon (Si) coated on free-standing vertically-aligned carbon nanotubes (VACNTs) can significantly improve the Li^+ storage by offering effective strain accommodation and electrolyte access due to the regular pore morphology and inter-tube space of the VACNTs array [32-35]. It is important to note that the VACNTs arrays in these reports were synthesized using catalyst-buffer bilayers on top of the current collector surface, and hence, the VACNT arrays cannot be classified as directly grown on the current collector. In addition, the bilayer materials add extra impurities to the active materials, which may complicate the electrochemical redox reaction by causing parasitic reactions. We proposed that a direct synthesis of VACNTs on current collectors (such as a Ni foam) and the high conductivities of VACNTs will reduce the electrical contact resistance between VACNTs and current collectors, which will enhance the charge transfer and facilitate effective heat dissipation caused by resistive heating. Furthermore, an array of VACNTs with a finite space between individual tubes can alleviate the stress resulting from volume alteration during the lithiation/delithiation reactions. Therefore, an electrode designed by growing VACNTs directly on the current collector and then coating the VACNTs with a layer of ultra-fine high-capacity electrode material such as SnO_2 nanoparticles without any binder could be an excellent LIB anode material with high energy capacity.

In this work, free-standing VACNT arrays have been grown directly on 3D nickel foam using a plasma-enhanced chemical vapor deposition method. The as-synthesized VACNTs have been coated with a layer of SnO_2 nanoparticles (SnO_2-VACNTs) to form core-shell structured hybrid material free of any binder. Then, the material was tested for its electrochemical lithiation property as the anode in coin-type lithium-ion half cells. The electrochemical Li^+ storage performance of the SnO_2-VACNTs anode has been measured, and assessed by comparing it with the SnO_2-coated Ni foam and pristine VACNTs synthesized on Ni foam. Furthermore, the excellent electrochemical Li^+ storage performance of the SnO_2-VACNTs anode has been explained in detail using electrode impedance evolution with the electrode cycle age. Moreover, the correlation between the microstructure and the electrochemical properties of the anode material has also been explained thoroughly.

2. Experimental

2.1 Electrodes preparation

Vertically aligned carbon nanotubes (VACNTs) were synthesized on nickel foam (Ni, 99.99% by wt., Alfa Aesar) using plasma-enhanced chemical vapor deposition (PECVD). The apparatus and synthesis procedure details are described in our previous work [36]. In brief, circular disks of a diameter of about 10 mm were punched out from as-received Ni foam (1.6 mm thick) and immersed sequentially in ultrasonic baths of isopropyl alcohol and acetone, each for 10 minutes. The cleaned Ni foam disks were placed into the PECVD system and then pumped down to the pressure of 0.01 Torr. The VACNT synthesis procedure was performed at 600 ºC for 6 minutes using C_2H_2 (25 sccm) as carbon precursor gas diluted with NH_3 (400 sccm). Also, the synthesis procedure was carried out at the pressure of 7 Torr and in the presence of a d.c. plasma of power 70 W to ensure the alignment of CNTs. Tin oxide (SnO_2) coated VACNTs (SnO_2-VACNTs) composite electrodes were fabricated using a wet-chemical method [26]. First, the VACNTs on Ni foam were functionalized using HNO_3 (20%) for 15 minutes. Before the final coating procedure, a precursor solution was formulated by dissolving 1 g of anhydrous tin (II) chloride ($SnCl_2$, 98%, Alfa Aesar) in 80 mL DI water and 1.4 mL HCl (38%). Then, the functionalized VACNTs were coated with SnO_2 nanoparticles by submerging them into the precursor solution for 9 hours. The weight of the SnO_2-VACNTs anodes (active material for Li^+ storage) was in the range of 1.02 – 1.21 mg cm^{-2}. This weight refers to the weight of VACNTs synthesized for 6 minutes and the weight of SnO_2 coated for 9 hours. However, in order to increase the areal capacity of the SnO_2-VACNTs anode for use in full cell performance test, the

VACNT growth time and SnO_2 coating time were increased to 20 minutes and 18 hours, respectively, which resulted in the SnO_2-VACNTs weight of ~1.7 mg cm^{-2}. For comparison purposes, bare Ni foams were coated with SnO_2 using a similar procedure, but the Ni foams were treated with Ozone for 30 minutes to remove any contaminants before being immersed in the precursor solution for SnO_2 coating. Finally, the SnO_2-coated electrodes were removed from the precursor solution and dried out overnight at 95 °C. The weight of the active material (SnO_2) coated on the Ni foam was ~1 mg cm^{-2} from a 9-hour coating process.

Furthermore, the cathode was fabricated by using commercial $LiNi_{0.8}Mn_{0.1}Co_{0.1}O_2$ (Lithium Nickel Manganese Cobalt Oxide, NMC811) microparticles. First, an N-methylpyrrolidone (NMP, anhydrous, 99.5%, Sigma-Aldrich)-based slurry composed of 90 wt% NMC (MTI Corp.), 2.5 wt% carbon nanotubes (ACS Materials), 2.5 wt% Super P conductive carbon (MTI Corp.), and 5 wt% polyvinylidene fluoride (PVDF) binder (MTI Corp.) was prepared by mixing at 320 rpm for 30 minutes using a vacuum mixture. Then, the resulting slurry was coated onto carbon-coated (thickness 1 μm) aluminum foil (thickness 15 μm) using a doctor blade calibrated to provide active material loading of ~15 mg cm^{-2}, an equivalent nominal areal capacity of ~3 mAh cm^{-2}. The electrode foil was dried at room temperature for 2 hours and 110 °C for 12 hours in a vacuum oven. The cathode was calendered at 90 °C to a target thickness of ~60 μm using a heated calendering machine.

2.2 Materials characterization

The surface morphology of VACNT arrays, SnO_2 layer coated on Ni foam (the sample will be termed as SnO_2 hereafter), and SnO_2-VACNTs were characterized using a field emission scanning electron microscope (SEM, JEOL JSM–6330F). The surface morphology of the Ni foam was analyzed using atomic force microscopy (AFM). The nanostructure, chemical composition, and crystal structure analysis of VACNTs and SnO_2-VACNTs were performed using a transmission electron microscope (TEM) operated at an accelerating voltage of 300 kV. Thermogravimetric analysis (TGA) of the materials was accomplished using the thermogravimetric-differential scanning calorimetry analysis (TG/DSC, SDT Q600 V20.9, USA). All experiments were performed under airflow and a temperature increase of 10 °C/min. In order to prepare the sample for the TGA experiments, the as-synthesized SnO_2-VACNTs were detached from the Ni foam using an IPA ultrasonic bath for 10 minutes. The possible Ni remanent in the SnO_2-VACNTs/IPA solution was carefully removed by using a strong bar magnet, and the SnO_2-VACNTs were filtered out from the resulting solution. Then, the SnO_2-VACNTs were dried overnight at 100 °C before the TGA experiment. Crystal structure and defect analysis of the as-synthesized materials were performed using X-ray diffraction (Siemens Diffraktometer D5000, Cu (Kα), $\lambda = 1.54$ Å, 0.02° step size, 20° to 80° range, 2°/min speed) and Raman spectroscopy (Ar^+, $\lambda = 632.8$ nm). A Fourier transform infrared spectrometer (Jasco, FTIR-4100) was used to analyze functional groups on the VACNTs and SnO_2-VACNTs. The chemical state of each element in the electrode was analyzed using X-ray photoelectron spectroscopy. The core level spectra were measured using a monochromated Al (Kα) X-ray source and a PHOIBOS 150 energy analyzer, both from SPECS.

2.3 Lithium-ion cell assembly and electrochemical measurements

Electrochemical properties of the as-synthesized materials were studied using CR2032 coin-type half cells with a lithium foil (3860 mAh g^{-1}) as the counter and reference electrode. Lithium hexafluorophosphate solution (1M $LiPF_6$) in ethylene carbonate and diethyl carbonate (EC:DEC, 1:1, vol. %) was used as an electrolyte, and Celgard polypropylene films were used as electrode separators. A symmetric test cell with identical working and counter electrodes of lithium foil (10 mm diameter) was used to evaluate and isolate the interfacial electrochemical properties of the working electrode from the counter/reference electrodes. In addition, a coin-type full cell was fabricated in an anode overhang configuration with a slightly bigger anode area (diameter 13 mm) compared to that of the cathode (diameter 12 mm) and electrodes overlapped area was used while calculating the areal capacity of the cell. However, the anode and cathode were of the same diameter (12 mm) in the case of the three-electrode cell. The specific capacities of the half cells were calculated based on the weight of active materials. For further clarification, the specific capacities of the SnO_2-VACNTs half cells were calculated based on the combined weight of VACNTs and SnO_2. The electrochemical properties were measured at room temperature (~23 °C) using a NEWARE battery tester, Gamry reference 3000 potentiostat, and Arbin battery cycler.

3. Results and discussion

3.1 Structural and compositional properties

3.1.1 AFM analysis

Vertically aligned carbon nanotube (VACNT) arrays were grown directly on catalytic 3D Ni foam without any external catalysts. The use of catalytic metal substrates such as Ni foam for synthesizing VACNTs facilitates the evolution of the catalytically active growth spots (nano-hills) on the substrate surface, which further initiates on-site disintegration of hydrocarbon precursor gas and the diffusion of carbon atoms into the catalytic sites, i.e., nano-hills [36]. Carbon atoms precipitate on the nano-sized catalyst surface upon supersaturation and lead to the formation of CNTs after graphitization [37]. To understand the growth of VACNTs on the catalytic substrate, the surface evolution of the Ni foam due to the heat treatment, under similar conditions used for VACNTs growth except carbon precursor gas, was analyzed using SEM and

AFM images (see **Figs. S1(a-c)**). Three-dimensional AFM images (**Fig. S1(b)**) revealed a relatively smooth surface of the pristine Ni foam with a mean roughness R_a = 53.68 nm, whereas the AFM image (**Fig. S1(c)**) after the heat treatment revealed a much rougher surface with R_a = 105 nm. This result confirmed that uniform catalyst sites (nano-hills) formed on the Ni foam surface due to the application of heat in the presence of reducing gas (NH_3) catalyzed the nucleation and growth of VACNT arrays.

3.1.2 SEM analysis

Figs. 1(a-c) show low to high magnification SEM images of Ni foam coated with SnO_2. The SEM images revealed the rough surface of Ni foam due to the non-uniform coating with macroscopic SnO_2 particles. As shown in the inset of **Fig. 1(c)**, the energy-dispersive X-ray

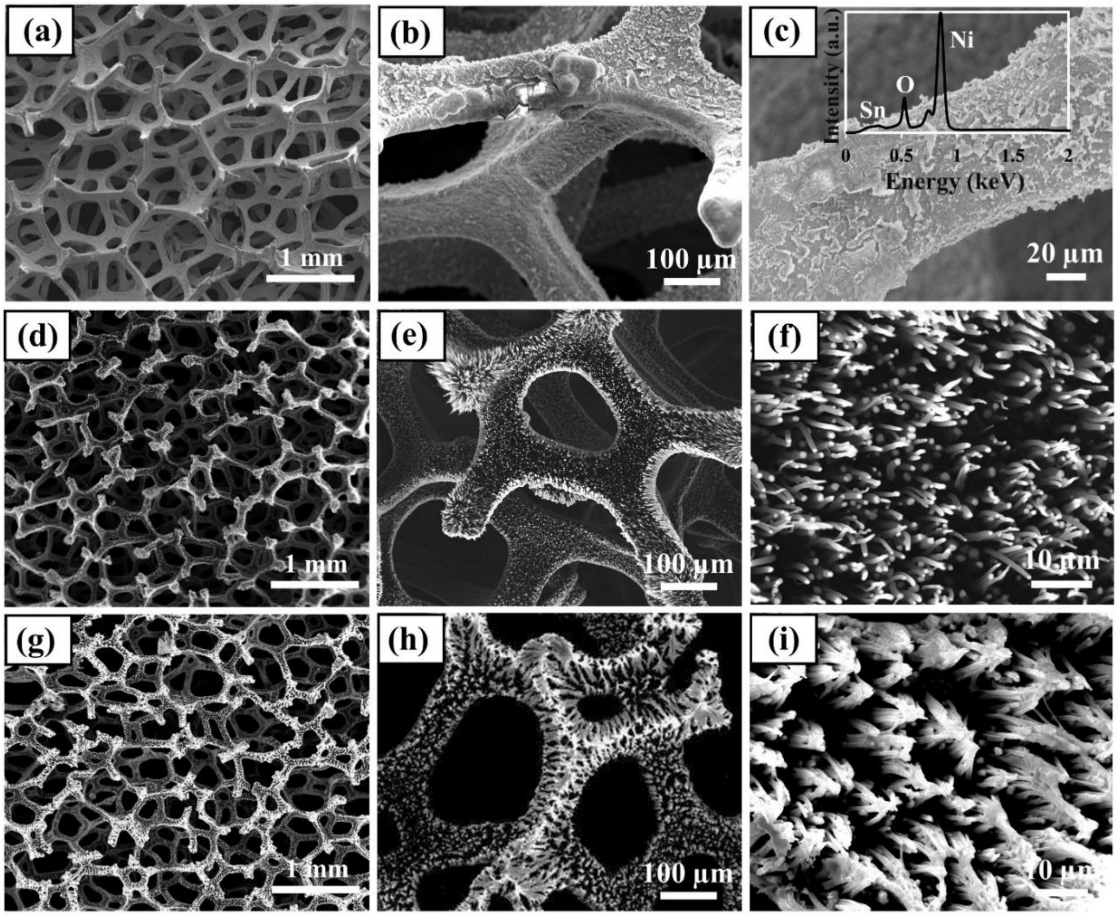

Fig. 1. SEM images of SnO_2 and SnO_2-VACNTs on Ni foam at low to high magnification. (a-c) SnO_2 coated on Ni foam, (d-f) VACNTs grown on Ni foam, and (g-i) SnO_2 coated on VACNTs. The inset in panel **(c)** represents the EDS spectrum measured on the surface of SnO_2 coated on Ni foam.

spectroscopy (EDS) measured on the surface of Ni foam confirmed that the particles on the surface are SnO_2. The Ni signal in the spectrum is from the Ni foam substrate. The ozone treatment of the Ni foam may have assisted in creating some functional groups on the surface, which could facilitate the coating of SnO_2 on the Ni foam. **Figs. 1(d-f)** show low to high magnification SEM images of vertically aligned and uniform arrays of CNTs grown on the Ni foam. The diameter of VACNTs was in the range of 150-270 nm, whereas the length was ~5 µm long. **Figs. 1(g-i)** display low to high magnification SEM images of uniquely bundled SnO_2-VACNT arrays in which the VACNT tips touch each other. These bundles were formed by the solution phase SnO_2 coating process.

3.1.3 TEM analysis

TEM image, as shown in **Figs. 2(a, b)**, revealed a “bamboo-like” morphology of as-synthesized VACNTs with a catalyst nanoparticle anchored at the top end of the tubular structure [37]. As shown in the inset of **Fig. 2(b),** the lattice fringes in the CNT wall are separated by 0.34 nm in the VACNT wall, suggesting the multi-walled structure of CNTs. The high-resolution TEM image of the tip of VACNT, as shown in **Fig. 2(c)**, revealed crystal lattice planes separated by 0.21 nm, which corresponds to the (111) lattice plane of face-centered cubic Ni crystal, as expected. This result indicates that the VACNTs were grown directly from the Ni foam. The direct connection between the VACNTs and Ni foam is expected to benefit the electron transfer between them. When poor electrical conducting material, such as SnO_2, is coated on the VACNTs’ surface, the VACNTs will also improve the electron transfer between the SnO_2 and Ni substrate. The distinct diffraction spots of the particle entrapped at the VACNT apex (upper-right inset of **Fig. 2(c)**) can be assigned to $(0\bar{2}0)$, $(\bar{1}\bar{1}1)$, and $(\bar{1}11)$ planes of face-centered cubic Ni crystal along the [101] zonal axis, which confirmed that the nanoparticle encapsulated inside the CNT is a single crystalline Ni particle. The EDS spectrum displayed in the inset of **Fig. 2(c)** further corroborated the particle at the CNT tip as a Ni metal. Furthermore, the peaks related to C and Cu in the spectrum occurred due to the VACNT wall and TEM holder, respectively.

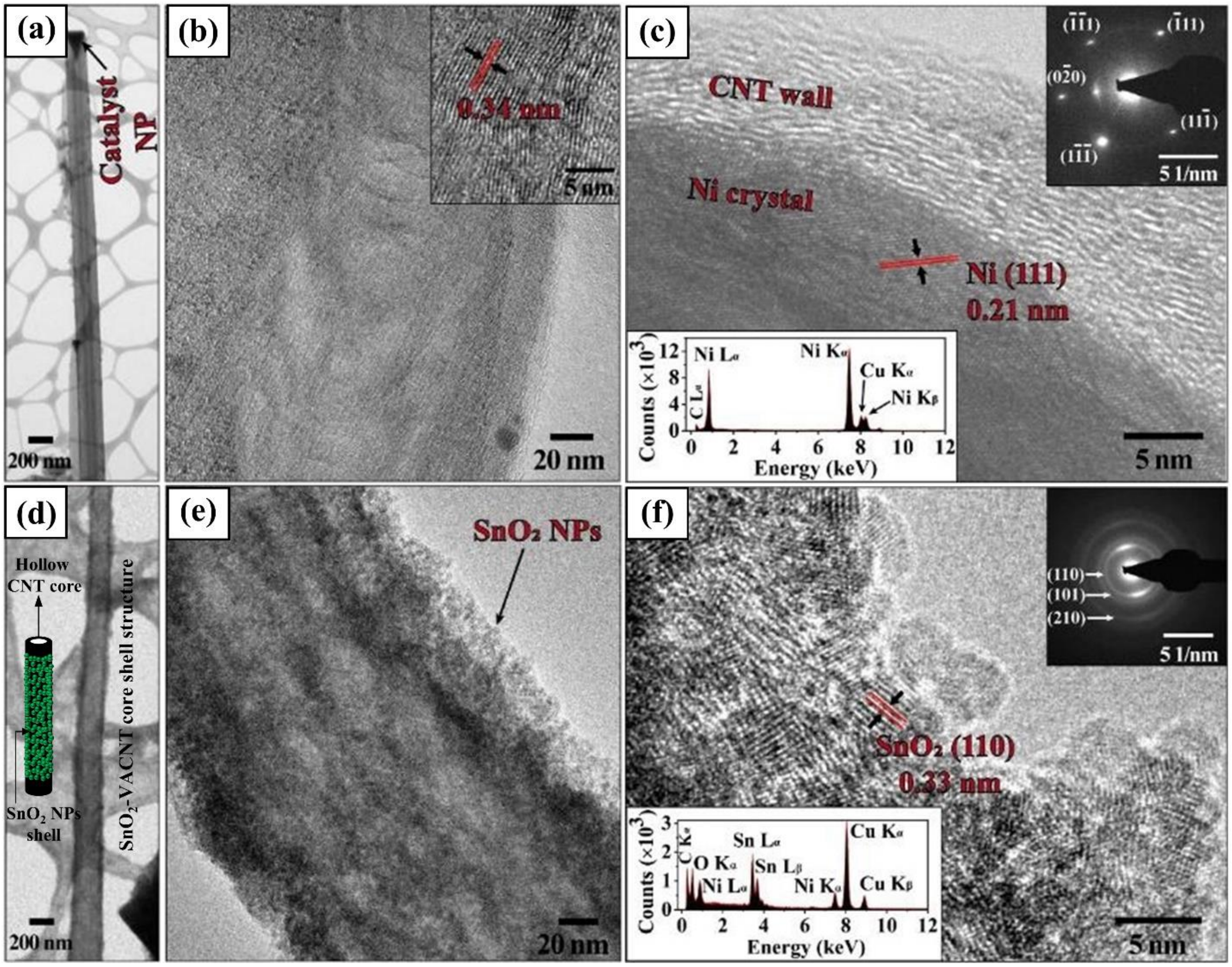

Fig. 2. TEM characterization of the as-synthesized VACNT (a-c) and SnO$_2$-VACNT (d-f) samples. (a) and (b) are low and high magnification images of a VACNT. The inset in panel (b) represents a high-resolution TEM image of the VACNT wall. (c) High-resolution TEM image showing an interfacial region between the VACNT wall and the catalyst particle. The upper-right and lower-left insets in panel (c)

represent the SAD and EDS of the Ni anchored at the VACNT apex. (d, e) Low and high magnification TEM images of a SnO_2-VACNT showing that the VACNT was coated with a layer of SnO_2-nanoparticles. The inset in panel (d) represents a schematic showing the core-shell structure of the SnO_2-VACNT. (f) High-resolution TEM image of the SnO_2 nanoparticles of a SnO_2-VACNT. The upper-right and lower-left insets in panel (f) are the SAD and EDS of the SnO_2 nanoparticles.

TEM images, as shown in **Figs. 2(d, e),** show a core-shell structure formed with the core of VACNT and a shell of a thin layer (~20 nm) of SnO_2 nanoparticles. For clarity, a schematic showing the core-shell structure of the SnO_2-VACNT is presented in the inset of **Fig. 2(d)**. The TEM images (**Figs. 2(e, f)**) clearly show that the coating consists of a multilayer of SnO_2 nanoparticles. A single layer of SnO_2 nanoparticles coating can be considered ideal regarding an efficient reversible electrochemical lithiation/delithiation of the SnO_2 nanoparticles. However, it is desirable to increase the content of the SnO_2 nanoparticles for practical applications, such as for high-energy-density LIBs. This means that there should be a fine balance between the coating thickness and the content of the SnO_2 nanoparticles for optimum performance of the SnO_2-VACNTs electrode. Although it is out of the scope of this work, it is imperative to determine the optimal content of the SnO_2 nanoparticles in the SnO_2-VACNTs electrode for future practical applications. The high-resolution TEM image in **Fig. 2(f)** confirmed the crystalline phase of SnO_2 nanoparticles with distinct crystal planes isolated by 0.33 nm, which can be assigned to the (110) lattice plane of the tetragonal SnO_2 (t-SnO_2) crystal. Furthermore, the EDS of the SnO_2-VACNT, the upper-right inset of **Fig. 2(f),** shows circular diffraction rings which can be indexed as (110), (101), and (210) lattice planes associated with the polycrystalline t-SnO_2. The occurrence of EDS peaks related to Sn, O, and C (lower-left inset of **Fig. 2(f)**) further confirmed the specimen as the SnO_2-VACNT core-shell. Moreover, the EDS peaks related to Ni and Cu can be assigned to the catalyst particle (Ni from Ni foam) anchored at the VACNT tip and TEM grid, respectively.

3.1.4 TGA analysis

In order to determine the weight percentage of SnO_2 nanoparticles on the SnO_2-VACNTs composite electrode, TGA analysis was performed, and the results are presented in **Fig. 3(a)**. The TGA profiles of VACNTs and SnO_2-VACNTs demonstrated weight loss as a result of moisture elimination up to 400 °C. However, SnO_2-VACNTs exhibited more significant weight loss, attributed to the solution-based SnO_2 coating process. The VACNTs demonstrated a slight weight reduction at ~435 °C due to the oxidation of amorphous carbon formed on the VACNTs during the synthesis process. Most of the weight loss of the VACNTs occurred in the temperature range of 520 °C – 605 °C. On the other hand, the SnO_2-VACNTs material showed a significant weight reduction at ~537 °C corresponding to the loss of the VACNTs. This result suggests that pristine VACNTs were more stable than the VACNTs in the SnO_2-VACNTs because the VACNTs in the SnO_2-VACNTs have more defects suffered from the SnO_2-coating process [38]. It has been verified that SnO_2 (~10 nm) nanopowder can show thermal stability up to 900 °C [39]. Therefore, the final residual after 800 °C of both samples should include only the dry mass of SnO_2, any impurities, and Ni particles initially encapsulated in the VACNTs tip, as all the carbonaceous species, such as CNTs and amorphous carbon, should be burnt off by 700 °C [40]. The TGA spectra revealed that the weight percentage of SnO_2 nanoparticles was ~40% of the total weight of SnO_2-VACNTs, which was obtained by subtracting the final remaining weight of the VACNTs from the final residual weight of SnO_2-VACNTs after 800 °C.

3.1.5 Raman spectroscopy and XRD analysis

Raman spectra displayed in **Fig. 3(b)** revealed an increase in the I_D/I_G ratio from 1.12 to 1.18, where I_D and I_G represent the intensity of D-band and G-band, respectively. This result indicates that the SnO_2 coating increased the defects on the VACNTs [41]. The defects were created on the VACNTs of the SnO_2-VACNTs sample due to the acid treatment of the VACNTs prior to SnO_2 coating. It has been reported that the presence of defects on the surfaces and tips of CNTs, such as vacancies, dangling bonds, edge dislocations, and functionalization sites, can serve as extra sites for Li^+ intercalation and adsorption, thereby increasing their lithium storage capacity [42]. In addition, it has also been reported that defects in the CNTs can lower the energy barrier for the Li^+ diffusion process [43]. These results indicate that the defective VACNTs in the SnO_2-VACNTs anode can potentially improve the overall electrochemical lithiation properties of the SnO_2-VACNTs anode. Furthermore, the functionalization of the VACNTs with oxygen-containing functional groups was essential for promoting the SnO_2 coating procedure. Moreover, as shown in **Fig. 3(c),** the crystal structure of VACNTs and SnO_2-VACNTs was investigated by XRD. The XRD spectrum of the SnO_2-VACNTs demonstrates the peaks related to crystal planes at 2θ positions of ~26.6°, 33.9°, 42.6°, and 51.4°. These peak positions can be assigned to (110), (101), (210), and (211) planes of the t-SnO_2 crystal. This result is consistent with the above TEM results and those reported in a publication [44]. In the XRD spectra shown in **Fig. 3(c)**, the peaks at ~26° and 42° correspond to the graphitic C signal from VACNTs.

3.1.6 FTIR analysis

As shown in **Fig. 3(d)**, FTIR spectra were used to determine the functional groups present on the VACNTs treated with HNO_3 only and coated with SnO_2 nanoparticles. It has been reported that treatment with a strong oxidizing agent such as HNO_3 can create different functional groups at the defect sites of CNTs [45]. The wide-survey FTIR spectra between 4000

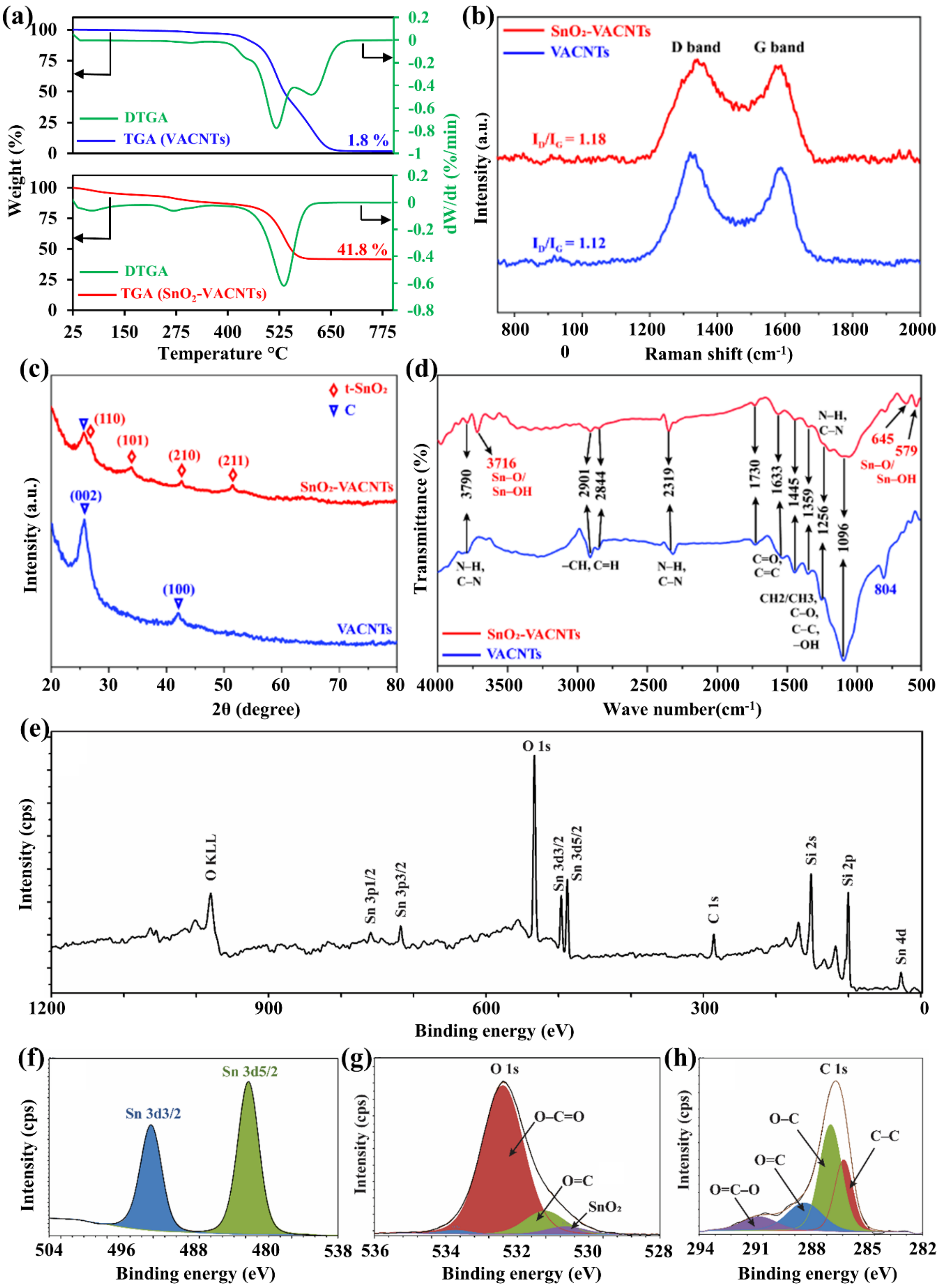

Fig. 3. (a) TGA, (b) Raman, (c) XRD, and (d) FTIR spectra of VACNTs and SnO_2-VACNTs. (e) The wide-survey and (f-h) high-resolution XPS spectra of SnO_2-VACNTs.

cm^{-1} and 500 cm^{-1} of both samples exhibited signals related to the C=C, C=O, C–N, and N–H stretching vibrations. In detail, peaks at wave number positions ~3790 cm^{-1}, 2319 cm^{-1}, and 1256 cm^{-1} are related to N–H and C–N bonds and can be accredited to adsorbed H_2O and NH_3 on the VACNT wall [46]. Moreover, the signals related to the –CH and C=H band stretching vibrations can be observed at 2901 cm^{-1} and 2844 cm^{-1}, respectively [47]. The peaks at ~1730 cm^{-1} and 1633 cm^{-1} can be assigned to the carboxyl (C=O) group and graphene layer (C=C) of VACNTs [45, 48, 49]. Furthermore, the band stretching signals at 1445 cm^{-1}, 1359 cm^{-1}, 1096 cm^{-1}, and 804 cm^{-1} are related to the CH_2/CH_3, C–C, C–O, and –OH group, respectively [50]. The composite material comprised of SnO_2 and carbon materials was further confirmed by the presence of signals at ~3716 cm^{-1}, 645 cm^{-1}, and 579 cm^{-1} [47, 51].

3.1.7 XPS analysis

The surface chemical constituents of the SnO_2-VACNTs were studied using XPS, as shown in **Figs. 3(e-h)**. A wide-survey XPS spectrum of the SnO_2-VACNTs (**Fig. 3(e)**) revealed the presence of C, O, and Sn (3p, 3d, and 4d). The prominent peaks of Sn and O suggested the existence of SnO_2 nanoparticles, whereas the C signal can be attributed to the VACNTs. In addition, the intense peaks of Si are ascribed to the Si substrate on which a thin layer of the SnO_2-VACNTs was deposited for the XPS measurements. The high-resolution Sn, O, and C peaks were analyzed to explain the chemical valence of elements in the SnO_2-VACNTs. As shown in **Fig. 3(f)**, the Sn 3d core level spectrum of SnO_2 demonstrated two distinct peaks centered at 487.7 and 496.2 eV corresponding to Sn $3d_{5/2}$ and Sn $3d_{3/2}$ levels of the energy splitting reported for SnO_2 [52], respectively. This result can be attributed to the Sn^{4+} valence state in the tetragonal rutile structure of the SnO_2 crystal [53]. The binding energy values for the spin-orbit splitting of the Sn 3d level are in close agreement with the binding energy values reported in the literature [52-55]. Detailed analysis of XPS spectra of O 1s for the SnO_2-VACNTs is shown in **Fig. 3(g)**. The high-resolution spectra revealed the presence of oxygen in three chemically nonequivalent states, represented by three well-fitted peaks in the spectrum of O 1s. The peak at a binding energy of 531.3 eV can be ascribed to oxygen in the composition of SnO_2 (i.e., O^{2-} of SnO_2) [53]. Furthermore, the XPS peaks at 532 and 533.5 eV correspond to oxygen in the O=C and O–C=O bonds, respectively, which can be attributed to the oxidation of VACNT sections uncoated by SnO_2 nanoparticles [53]. **Fig. 3(h)** shows the high-resolution XPS spectrum of C 1s, which consists of four well-fitting peaks centered at 284.9, 285.7, 287.4, and 290.2 eV corresponding to the C–C, O–C, C=O, and O=C–O groups, which are in agreement with the previous reports [52, 56].

3.2 Electrochemical lithiation properties

3.2.1 Electrochemical properties test in half-cell configuration

The electrochemical Li^+ storage properties of SnO_2 and SnO_2-VACNTs were investigated using cyclic voltammetry (CV) between 0.01 and 3 V (vs. Li/Li^+) for five cycles, as shown in **Figs. 4(a, b)**. The cell potential was swept at a constant scan rate of 0.2 mV s^{-1}, and the corresponding current was recorded. Sharp irreversible reduction peak at ~1.08 V for SnO_2 and ~0.81 V for SnO_2-VACNTs during the first cycle suggested the solid electrolyte interphase (SEI) formation on the electrode surface due to the decomposition of organic solvents such as EC and DEC. The reduction peaks can also be related to the initial irreversible reduction of SnO_2 to Sn and Li_2O (**Eq. 1**) [57]. The reversible reduction peak at ~0.56 V for the SnO_2 can be attributed to the alloying of Li with Sn. However, this reduction peak emerged at a much lower voltage of ~0.27 V for the SnO_2-VACNTs anode. Another reduction peak for the SnO_2 anode was detected in the range of ~1.5 – 1.67 V, and interestingly, both the peak position and intensity were decreased with the CV cycles. The reversible oxidation peaks at ~1.05 V, 1.41 V, and 2.29 V for the SnO_2 anode can be assigned to the dealloying of Li_xSn (**Eq. 2**) [58] and oxidation of Sn^{+2}. Similar to the reversible reduction peak, these reversible oxidation peaks for the SnO_2-VACNTs anode were observed at lower potentials of ~0.67, 1.32, and 2.01 V, respectively, compared to those for the SnO_2 anode. The shift of these peak positions toward the lower potential side for the SnO_2-VACNTs anode may be attributed to the lower impedance of the anode compared to the SnO_2 anode, as shown in the 1st and 5th impedance spectra in **Figs. 5(a, b)**. The SnO_2-VACNTs anode exhibited stable CV cycles after the first cycle in terms of peak positions and area under the curves, which may indicate long-term cycle stability with good capacity retention. It is well known that CNTs are also electrochemically active materials for Li^+ storage. A detailed description of the CV and galvanostatic charge/discharge potential profiles of VACNTs anodes measured in half-cell configurations is provided in **Fig. S2** (Supplementary Information). Furthermore, we also conducted an in-situ TEM experiment to understand the lithiation process of the SnO_2-VACNTs anode and a detailed explanation is provided in **Fig. S3** and **S4** (Supplementary Information).

Figs. 4(c, d) show the galvanostatic lithiation/delithiation potential profiles of SnO_2 and SnO_2-VACNTs at different cycles measured at a current density of 0.1 A g^{-1} between cut-off potentials of 0.01 V and 3 V (vs. Li/Li^+). The first lithiation and delithiation capacities for the SnO_2 electrode were 3080 mAh g^{-1} and 2160 mAh g^{-1}, respectively. Also, the first lithiation and delithiation capacities for the SnO_2-VACNTs anode were 3530 mAh g^{-1} and 2360 mAh g^{-1}, respectively. Theoretical calculations have implied that reversible capacity exceeding a LiC_2 stoichiometry [59, 60], which is equivalent to ≥1116 mAh g^{-1}, is achievable for CNTs [61]. Also, considering the theoretical specific capacity of SnO_2 as 1493 mAh g^{-1} [12], the theoretical specific capacity of the SnO_2-VACNTs can be calculated as 1267 mAh g^{-1}. That means that the experimental capacities of the SnO_2-VACNTs exceeded the theoretical limit significantly. It is strange, in general, for an electrode to show a higher capacity than the theoretical limit; however,

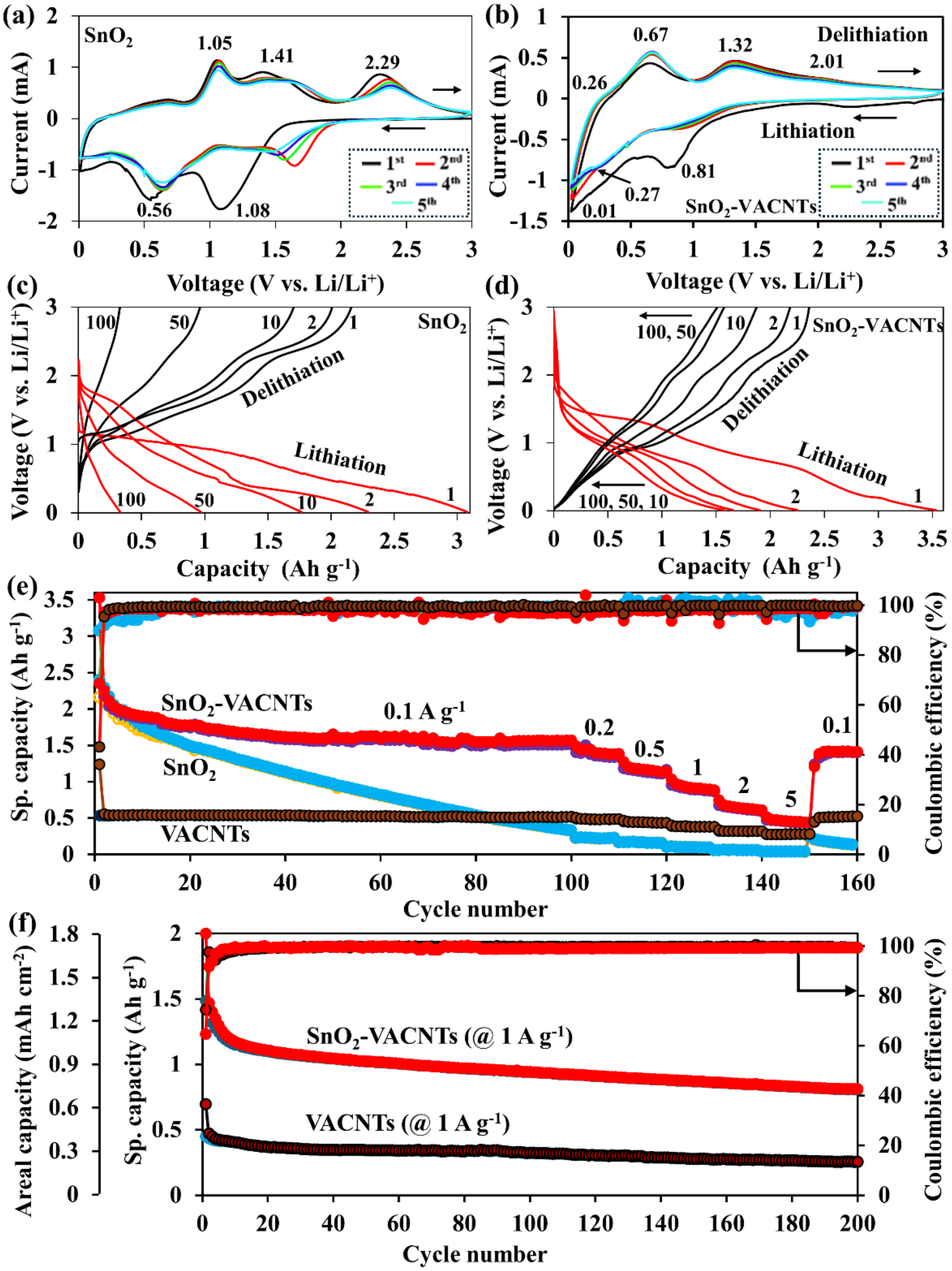

Fig. 4. (a, b) Cyclic voltammograms of SnO_2 and SnO_2-VACNTs scanned at 0.2 mV s^{-1} between 0.01 and 3 V. (c, d) Galvanostatic charge/discharge potential profiles of SnO_2 and SnO_2-VACNTs at the current density of 0.1 A g^{-1} between 0.01 to 3 V. (e) Cyclability and rate performance tests of SnO_2, VACNTs, and SnO_2-VACNTs anodes. (f) Cycling performance of the VACNTs and SnO_2-VACNTs anodes at a high current density of 1 A g^{-1}.

such an anomaly has been encountered in the past only in the case of ultrafine (typically ≤ 10 nm) SnO_2 nanoparticle-based anodes [62, 63]. This anomaly can be accredited to the interfacial storage of Li^+ at the phase boundaries of ultrafine SnO_2 nanoparticles. Theoretical calculations and experimental results have shown that nanocomposites composed of extremely fine nanoparticles with high surface area-to-volume ratios can demonstrate extra lithium storage capacity [64, 65]. Because the size of the SnO_2 nanoparticles in the SnO_2-VACNTs composite was only ~5 nm, they possess an extremely high interfacial surface-to-volume ratio and, thus, a great potential for interfacial Li^+ storage. Furthermore, it should also be noted that the defects on the VACNTs created due to the acid treatment (see **Section 3.1.5**) and the high surface-to-volume ratio of the VACNTs may have provided extra lithium storage capacity. On the other hand, the absence of VACNTs and the difference in SnO_2 morphology may have led to a lower initial capacity of the SnO_2 anode compared to the SnO_2-VACNTs composite anode.

Both electrodes showed initial coulombic efficiencies of about 70%. The specific capacities of both electrodes dropped significantly in the second cycle, suggesting poor capacity retention due to irreversible capacity loss. A plateau at ~1.1 V in the first lithiation curve of the SnO_2 anode is associated with the SEI and amorphous Li_2O matrix formation, and another plateau at ~0.5 V can be related to the alloying of Li with Sn metal [66-68]. In contrast, a plateau at ~1.4 V in the first lithiation curve of the SnO_2-VACNTs anode may be ascribed to the irreversible reduction of oxygen-containing surface species on VACNTs [67]. Also, the plateau that emerged at ~0.8 V can be accredited to the formation of SEI and amorphous Li_2O. These results agree well with the results obtained from the CV measurement, although a reduction peak related to the plateau at ~1.4 V in the first lithiation curve of the SnO_2-VACNTs was not observed in the first CV cycle. The potential profiles at different cycles for the SnO_2 anode displayed continuous capacity degradation as the cycle increased. However, the SnO_2-VACNTs anode exhibited improved stability compared to the SnO_2 anode.

The long-term cycle stability test of the pristine VACNTs, SnO_2, and SnO_2-VACNTs anodes was assessed for 100 cycles of lithiation and delithiation at a current density of 0.1 A g^{-1} followed by rate performance tests after 100 cycles, and the results are shown in **Fig. 4(e)**. The VACNTs anode displayed excellent cyclability with a delithiation capacity of ~535 mAh g^{-1} after 100 cycles, which is ~4% degradation in delithiation capacity with respect to the first cycle. In contrast, the SnO_2 anode showed continuous capacity decay with a low delithiation capacity of ~327 mAh g^{-1} after 100 cycles. The SnO_2-VACNTs anode displayed considerably more stable cycle performance than the SnO_2 anode with a high delithiation capacity of ~1512 mAh g^{-1} after 100 cycles. It should be noted that the SnO_2-VACNTs anode also suffered significant capacity fading during the first 20 cycles, but it became stable after the first 20 cycles. The initial poor cyclability of the SnO_2-VACNTs anode may be attributed to the significant volume alteration and pulverization of SnO_2 nanoparticles, which led to the detachment of the SnO_2 nanoparticles poorly bonded to the VACNT wall. In addition, this significant capacity fading during the initial cycles may also be attributed to the coating of SnO_2 on the bare area of Ni foam where VACNTs were not present. The SnO_2 coated on Ni foam can be easily detached from the Ni foam due to the pulverization during the lithiation/delithiation process. The poor cycle stability of the SnO_2

anode, as shown in **Fig. 4(e)**, further supports this hypothesis. Furthermore, VACNTs and SnO_2-VACNTs anode materials demonstrated excellent rate capability, as shown in **Fig. 4(e)**. At current densities of 0.2, 0.5, 1, 2, and 5 A g^{-1}, the reversible capacities of the SnO_2-VACNTs were ~1382, 1137, 895, 625, and 449 mAh g^{-1}, respectively. Also, the rate performance exhibited that the SnO_2-VACNTs anode retained ~83 % of its reversible capacity at 0.1 A g^{-1} compared to the specific capacity at the 100th cycle at the same rate, as shown in **Fig. 4(e)**. In contrast, the SnO_2 anode exhibited poor rate performance, as shown in **Fig. 4(e)**. In addition, the SnO_2-VACNTs anode showed a stable long-term cycling test with a capacity retention of ~60% and a specific capacity of 813 mAh g^{-1} at a high rate of 1 A g^{-1} after 200 cycles, as shown in **Fig. 4(f)**. Although the capacity retention is lower, the specific capacity of the SnO_2-VACNTs anode at the 200th cycle at the current rate of 1 A g^{-1} is better or comparable compared to similar electrodes reported in the literature [69-71]. Furthermore, **Table 1** compares the half-cell performance of the SnO_2-VACNTs anode with similar anodes reported in various literature.

Table 1. Half-cell performance comparison of the SnO_2-VACNTs anode with similar anodes reported in various literature.

Active material	SnO_2 size (nm)	Half cell performance			Ref.
		Cycle number (n)	Sp. capacity (mAh g^{-1}) at nth cycle	Current rate	
SnO_2	3-8	200	1425	0.1 A g^{-1}	[12]
SnO_2	3-8	350	1062	1 A g^{-1}	[12]
SnO_2	3-10	40	760	0.1 A g^{-1}	[72]
Sn-CNF	100	200	774	0.8 A g^{-1}	[73]
SnO_2@CNTs	4	200	1192	0.223 A g^{-1}	[74]

Fe-doped SnO_2	7-8	50	600	0.05 A g^{-1}	[63]
Sb-doped SnO_2-rGO	3	100	813	1.249 A g^{-1}	[75]
F-doped SnO_2-rGO	5	200	1439	0.2 A g^{-1}	[62]
SnO_2-VACNTs	5	100	1512	0.1 A g^{-1}	This work
SnO_2-VACNTs	5	200	813	1 A g^{-1}	This work

AC impedance measurements of the different electrodes were carried out using electrochemical impedance spectroscopy (EIS). The impedance measurements were conducted in the potentiostatic mode using a sine wave of 5 mV amplitude between 100 kHz and 50 mHz frequency range. The impedance measurements were carried out at different lithiation/delithiation cycles to understand the impedance evolution of electrodes with cycle age. For a fair comparison between different cycles and samples, cells were completely delithiated first and rested for three hours for cell stabilization before the EIS measurements. **Figs. 5(a, b)** show Nyquist plots of the SnO_2 and SnO_2-VACNTs at different cycle ages. The intercept by the EIS spectrum on the Z' axis at high frequencies corresponds to the equivalent series resistance (R_s) related to the total resistance of the electrolyte, separator, and electrical contacts. The spectra also comprise a small semicircle at high frequencies followed by a larger semicircle in the high-to-medium frequency region. Furthermore, the plots show another semicircle in the medium-to-low frequency region, which becomes more prominent as the cell ages (after the 5th cycle), and a straight line inclined to the real axis (Z' axis) at low frequencies. The high-frequency semicircle with a small diameter can be attributed to the impedance related to the SEI (C_{SEI}, R_{SEI}) developed on the electrode surface due to the electrolyte reduction, while the second semicircle with a larger diameter can be attributed to the impedance related to the charge transfer through double layer (C_{DL}, R_{CT}) during the lithiation/delithiation reaction [76-78]. An interesting feature of the impedance spectra shown in **Fig. 5(a, b)** is the presence of the third semicircle in the medium-to-low frequency region. The origin of this semicircle in the EIS spectra is discussed in detail in the following paragraphs. Also, the straight line at the low-frequency region of the impedance spectrum is related to the lithium diffusion process within the electrode [79]. In addition, it should be noted that the size of the semicircles, particularly those related to the charge transfer, decreased significantly until the 50th cycle for both electrodes. After the 50th cycle, it increased substantially up to the 100th cycle for the SnO_2 cell. However, for SnO_2-VACNTs, the semicircles related to the charge transfer and the SEI were almost unchanged from the 50th cycle

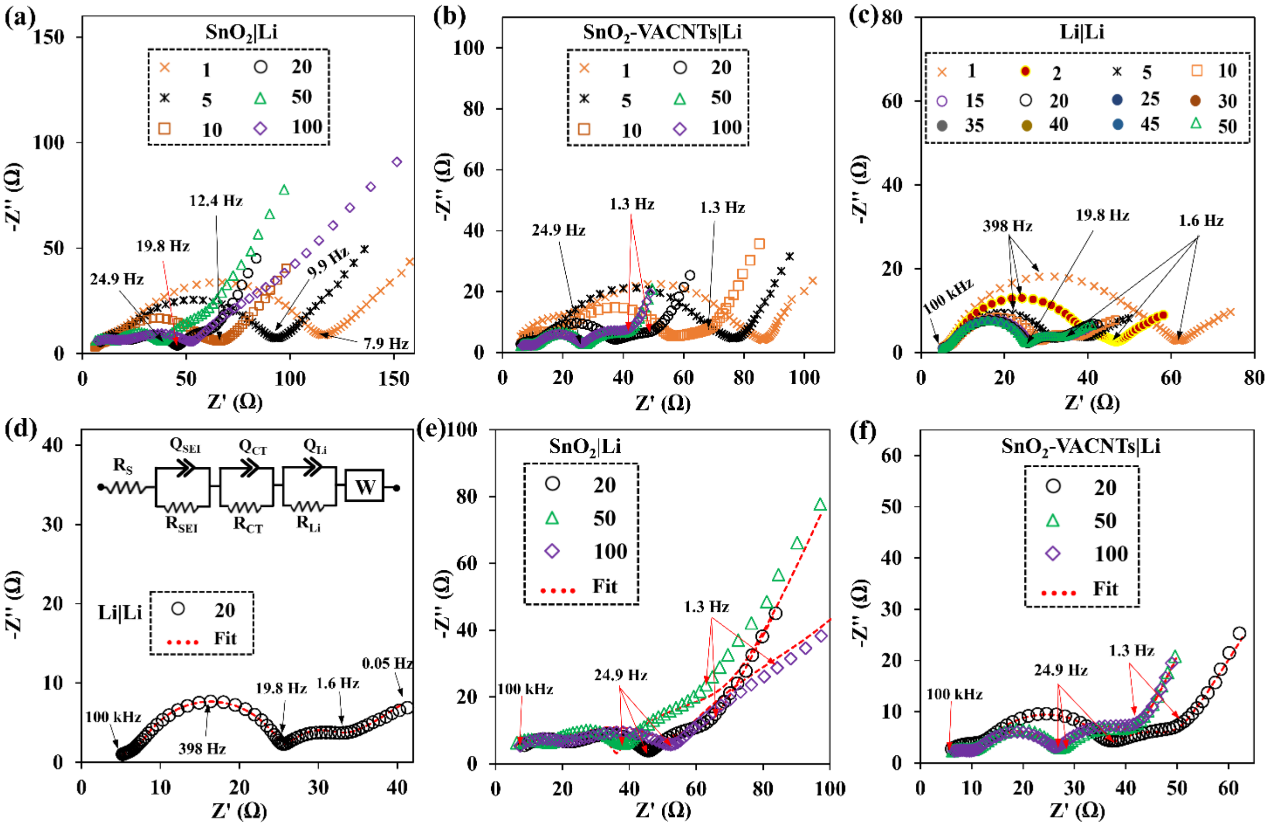

Fig. 5. EIS spectra of (a) SnO_2, (b) SnO_2-VACNTs, and (c) lithium-lithium symmetric cell measured at various cycles. Experimental and fitted EIS spectra of the (d) lithium-lithium symmetric cell at the 20th cycle, (e) SnO_2, and (f) SnO_2-VACNTs measured at the 20th, 50th, and 100th cycles. The inset in panel (d) represents an ECM for fitting measured EIS spectra.

to the 100th cycle, as shown in **Fig. 5(b)**, indicating stable SEI and efficient charge transfer process without a significant increase in the impedance. In this case, it should be noted that the half-cell impedance represents the combination of the interfacial properties of both the working electrode and the lithium counter electrode. Therefore, the EIS spectrum of a half cell does not correctly characterize the interfacial properties of a single working electrode [80, 81].

In order to accurately evaluate and isolate the interfacial electrochemical properties of the working electrode from the counter/reference electrode, a symmetric test cell with identical working and counter electrodes of lithium foil was used [80]. The lithium symmetric cell was polarized (charged and discharged for 30 minutes each) using a current density of 0.1 mA cm^{-2}, and EIS measurements were carried out at various cycles, as shown in **Fig. 5(c)**. The impedance spectra comprise a small semicircle at high frequencies related to the SEI, a large semicircle in the high-to-medium frequency region related to the charge transfer, another semicircle in the medium-to-low frequency (~20 – 1.6 Hz) region, and a Warburg diffusion region. Interestingly, the small semicircle in the medium-to-low frequency region emerged only after the first cycle and gradually evolved with the cell age. Regarding its frequency range and evolution with the cell aging, this result implies that the third semicircle in the EIS can be related to the surface morphology evolution-driven reaction kinetics on the lithium electrode. During the initial few cycles, lithium preferentially deposits on the lithium electrode surface as mossy dendrites that increase the surface area, offering lower-impedance pathways for charged particles [82]. As a result, charge transfer resistance significantly decreased until the 20th cycle (**Fig. 5(c)**). As the cell ages, these mossy dendrites can be mechanically detached and electrically isolated from the bulk lithium surface, creating a tortuous interphase layer (TIL) [54], different from the SEI, between the bulk lithium surface and electrolyte. This TIL can limit mass transport (observable at low frequencies) during cell cycling, and hence, the third semicircle in the EIS spectrum can be associated with this phenomenon.

In addition, the impedance of the symmetric cell stabilized after the 20th cycle and remained similar afterward. Therefore, the decrease in the overall impedance of SnO_2 and SnO_2-VACNTs half cells during the initial 20 cycles can be attributed partially to the lithium counter electrode. Furthermore, the EIS of the symmetric cell at the 20th cycle (**Fig. 5(d)**) is selected to estimate the contribution of the lithium counter electrode in the impedances of SnO_2 and SnO_2-VACNTs half cells. The symmetric cell consists of two similar lithium-electrolyte interfaces. Hence, the impedance of the symmetric cell represents a doubling of a single lithium electrode. The values of circuit components obtained by fitting the EIS spectrum of the symmetric cell at the 20th cycle using an equivalent circuit model (ECM) (inset of **Fig. 5(d))** are presented in **Table 2**.

The ECM comprises serial resistance (R_s), representing the cell's ohmic resistance, and three parallel resistor-constant phase element (R-Q) networks, corresponding to three semicircles in the measured EIS spectra. The ECM uses constant phase elements to simulate depressed semicircles in the EIS spectra [83]. An R-Q parallel network can be estimated with a resistor-capacitor (R-C) parallel network, and the capacitances related to the different electrochemical events in the electrode (C_{SEI}, C_{DL}, C_{Li}) can be calculated using the following equation.[

$$C = [(R*Q)^{1/\alpha}]/R \qquad (3)$$

where α is a constant with values between 0 and 1 [84].

Table 2. Element values obtained by fitting the EIS spectra of SnO_2, SnO_2-VACNTs, and Li-Li symmetric cells using the ECM shown in the inset of **Fig. 5(d)**.

Electrode	Cycle	R_S (Ω)	R_{SEI} (Ω)	C_{SEI} (μF)	R_{CT} (Ω)	C_{DL} (μF)	R_{Li} (Ω)	C_{Li} (mF)	D_{Li^+} (cm^2 s^{-1})
SnO_2									
	20	4.11	14.95	0.24	18.29	11.82	23.86	6.08	4.3×10^{-13}
	50	3.21	13.75	0.26	16.54	9.94	30.88	3.89	1.9×10^{-13}
	100	4.89	12.22	0.30	35.64	6.35	37.99	7.54	3.9×10^{-14}
SnO_2-VACNTs									
	20	3.81	8.10	0.48	25.33	12.57	10.73	4.53	1.2×10^{-12}
	50	4.16	5.56	0.46	17.65	18.08	12.37	6.80	2.2×10^{-12}
	100	4.34	5.38	0.42	18.49	21.29	13.44	7.03	2.5×10^{-12}
Li-Li									
	20	4.49	3.05	1.78	17.41	17.12	4.76	12.55	2.5×10^{-12}

Figs. 5(e, f) show the experimental and fitted impedance spectra of SnO_2 and SnO_2-VACNTs at the 20th, 50th, and 100th cycles using the ECM, and fitting parameters are shown in **Table 2**. The table shows that resistances, R_{SEI} and R_{CT}, decreased after the 20th cycle up to the 50th cycle for both electrodes, which can be ascribed to the decomposition of the electrolyte on the electrode surface that generates protons, which in turn enhances the conductivity, lowering the impedance of the passivated film and charge transfer [81]. After the 50th cycle, the R_{SEI} and R_{CT} increased significantly for the SnO_2 electrode. This increase can be attributed to the continuous SEI formation and the active material (SnO_2) detachment from the Ni foam due to continuous and significant volume alteration and pulverization during the lithiation/delithiation process [85]. The continuous capacity fading during the cyclability test and poor rate performance at the high current density, as shown in **Fig. 4(e)**, are in agreement with the increased SnO_2 electrode resistances.

On the other hand, the R_{SEI} and R_{CT} values remained nearly similar from the 50th to 100th cycles for the SnO_2-VACNTs electrode, and R_{CT} is significantly smaller compared to the SnO_2 electrode at the 100th cycle, indicating fast electron transport and faradaic reactions at the electrode surface assisted by highly conductive VACNTs, strong adhesion of SnO_2 nanoparticles on the VACNTs aided by the functional groups on the VACNTs wall, and direct connection of VACNTs to the current collector (Ni foam). As a result, the SnO_2-VACNTs electrode exhibited a much better cycle stability and rate performance than the SnO_2 electrode. Also, it should be noted that the capacity fading of the SnO_2-VACNTs during the first few cycles (**Figs. 4(e, f)**) can be ascribed to the resistance increase due to the formation and continuous thickening of SEI along with the loss of SnO_2 active materials. In contrast, the R_{Li} increased continuously from the 20th to the 100th cycle for both electrodes. Furthermore, it should also be noted that the time constants corresponding to the third semicircle ($R_{Li}*C_{Li}$) for the SnO_2 and SnO_2-VACNTs half cells are higher than that for the symmetric lithium-lithium cell. These results indicate that the third semicircles in the frequency range of ~20 – 1.6 Hz in EIS spectra of the SnO_2 and SnO_2-VACNTs may not have originated solely due to the lithium counter electrode, and working electrodes may have contributed to the evolution of the third semicircle. This complicates the isolation of the working electrode impedance entirely from the counter electrode impedance and requires more in-depth study.

Furthermore, the solid-state diffusion property of SnO_2 and SnO_2-VACNTs electrodes was studied using the Li^+ diffusion coefficient (D_{Li^+}) given by the following equations [86].

$$D_{Li^+} = (R^2 T^2)/(2A^2 n^4 F^4 C^2 \sigma_w^2) \qquad (4)$$

where R (8.314 J mol^{-1} K^{-1}) is the gas constant, T (298 K) is the absolute room temperature, A (0.785 cm^2) is the area of the electrode, n (4.4, regarding Sn alloying with Li up to a maximum theoretical limit of $Li_{22}Sn_5$ [87]) is the number of electrons per species reaction during the oxidation/reduction reaction, F (96500 C mol^{-1}) is the Faraday constant, σ_W is the Warburg's impedance coefficient, and C (0.001 mol cm^{-3}) is the molar concentration of Li^+ ions. The values of σ_W were determined by fitting the experimental data using Warburg's element in the ECM, as shown in the inset of **Fig. 5(d)**. The Li^+ diffusion coefficients of SnO_2, SnO_2-VACNTs, and lithium-lithium symmetric cells calculated using eq. (4) are presented in **Table 2**. The table shows that the Li^+ diffusion coefficients of the SnO_2-VACNTs electrode are significantly higher than that of the SnO_2 electrode. This result suggests that the ultra-fine SnO_2 particles (< 5 nm) coated on VACNTs with proper inter-tube distance and better electrolyte accessibility could provide more favorable Li^+ transportation kinetics and shorten the Li^+ diffusion pathway at the

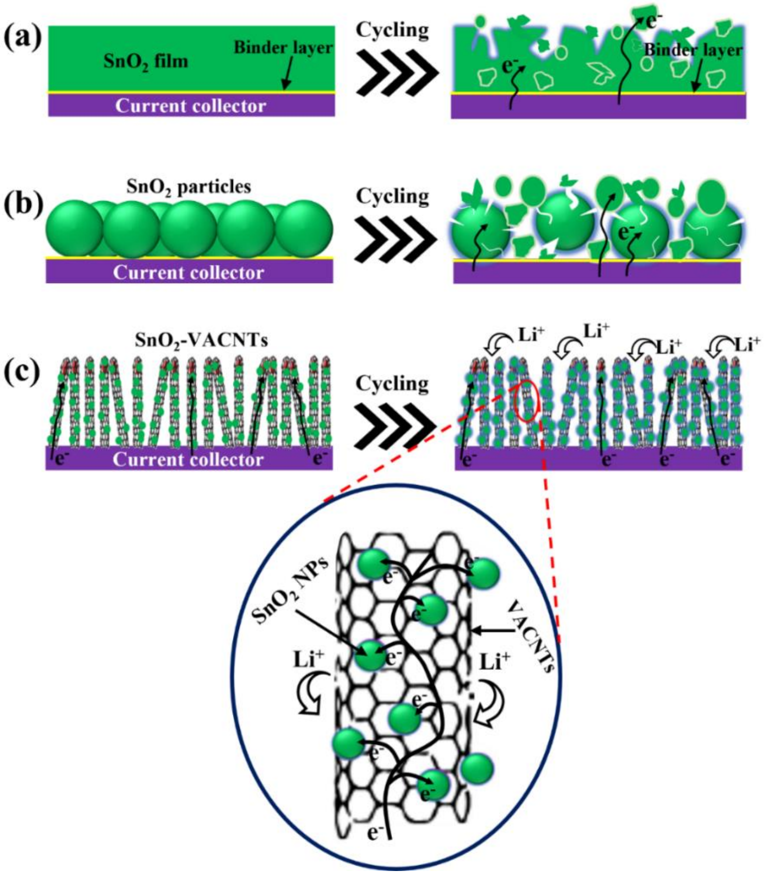

Fig. 6. Schematic representation of morphological changes in SnO_2 (thin film, macro-particles, and nanoparticles on VACNTs) electrodes due to electrochemical cycling.

electrode/electrolyte interfaces. Since Li^+ diffusion is directly related to the rate capability of the electrode, higher reversible capacities with remarkable stability of SnO_2-VACNTs at higher current densities (**Figs. 4(e, f)**) further indicate the faster Li^+ transportation kinetics and shorter Li^+ diffusion pathway compared to the SnO_2 electrode.

The Li^+ storage performance of the SnO_2-VACNTs anode can be described using a schematic, as shown in **Fig. 6**. The SnO_2 electrode undergoes a large volume change during the lithiation process, leading to fracture in bulk or micron/macro-sized materials (**Figs. 6(a, b)**) [88]. Due to this, materials lose connection with the current collector. As a result, electrodes face severe capacity decay as electronic charge carriers should move through interparticle contact areas, as shown in **Figs. 6(a, b)**. Previous reports have recommended a materials-dependent critical particle size below which particles do not pulverize upon lithiation [89]. In addition, binders used for active materials coating on the current collector can seriously undermine the electrode's overall conductivity and add extra weight (so-called dead weight) to the electrode. In contrast, in the case of SnO_2-VACNTs electrodes, VACNTs were synthesized directly on the catalytic metal current collector substrate (3D Ni foam). Each VACNT coated with SnO_2 NPs was electrically connected to the metallic current collector, so all the SnO_2-VACNT nanowires contributed to the capacity. Also, the VACNTs have direct one-dimensional electronic pathways (**Fig. 6(c)**), ensuring efficient charge transport to individual SnO_2 NPs, which can be very important for the high-rate performance of the electrode. Furthermore, an array structure with a regular space between the SnO_2-VACNT nanowires can effectively accommodate the large volume changes due to efficient strain relaxation and significantly improve the electrolyte accessibility during the lithiation/delithiation process.

3.2.2 Cycling test in full-cell configuration

In order to understand the practical applicability of the SnO_2-VACNTs as an anode for LIBs, we assembled a coin-type full cell composed of the SnO_2-VACNTs anode and a $LiNiMnCoO_2$ (NMC) cathode with the positive-to-negative electrode capacity ratio (P/N) of ~1.1. The physical morphology characterization of the NMC cathode by SEM and its electrochemical properties in the half-cell configuration are presented in Supplementary Information (**Section 4, Fig. S5**). A low initial coulombic efficiency (ICE ≤ 80%), which is most prevalent in alloying/dealloying-type electrodes, is one of the reasons for preventing these types of electrodes in practical applications. The low ICE requires an excessive amount of cathode materials (≥10%–15% even for typical graphite anodes) to overcome the low ICE of the anode, resulting in a significant decrease in energy density [90]. A few methods, such as electrolyte optimization and pre-lithiation of the anode by direct contact with lithium metal, have been proposed to improve the ICE of the alloying/dealloying-type anodes composed of nanoparticles [90, 91]. However, the SnO_2-VACNTs electrode in this work was pre-lithiated in a half-cell for three cycles prior to assembly of the full cell to reduce the effect of the poor ICE. Furthermore, the potential profiles of the SnO_2-VACNTs anode (vs. reference), NMC cathode (vs. reference), and full cell were measured using a three-electrode coin-type cell with a lithium reference electrode to determine the cutoff potentials of the full cell, as shown in **Fig. 7(a)**.

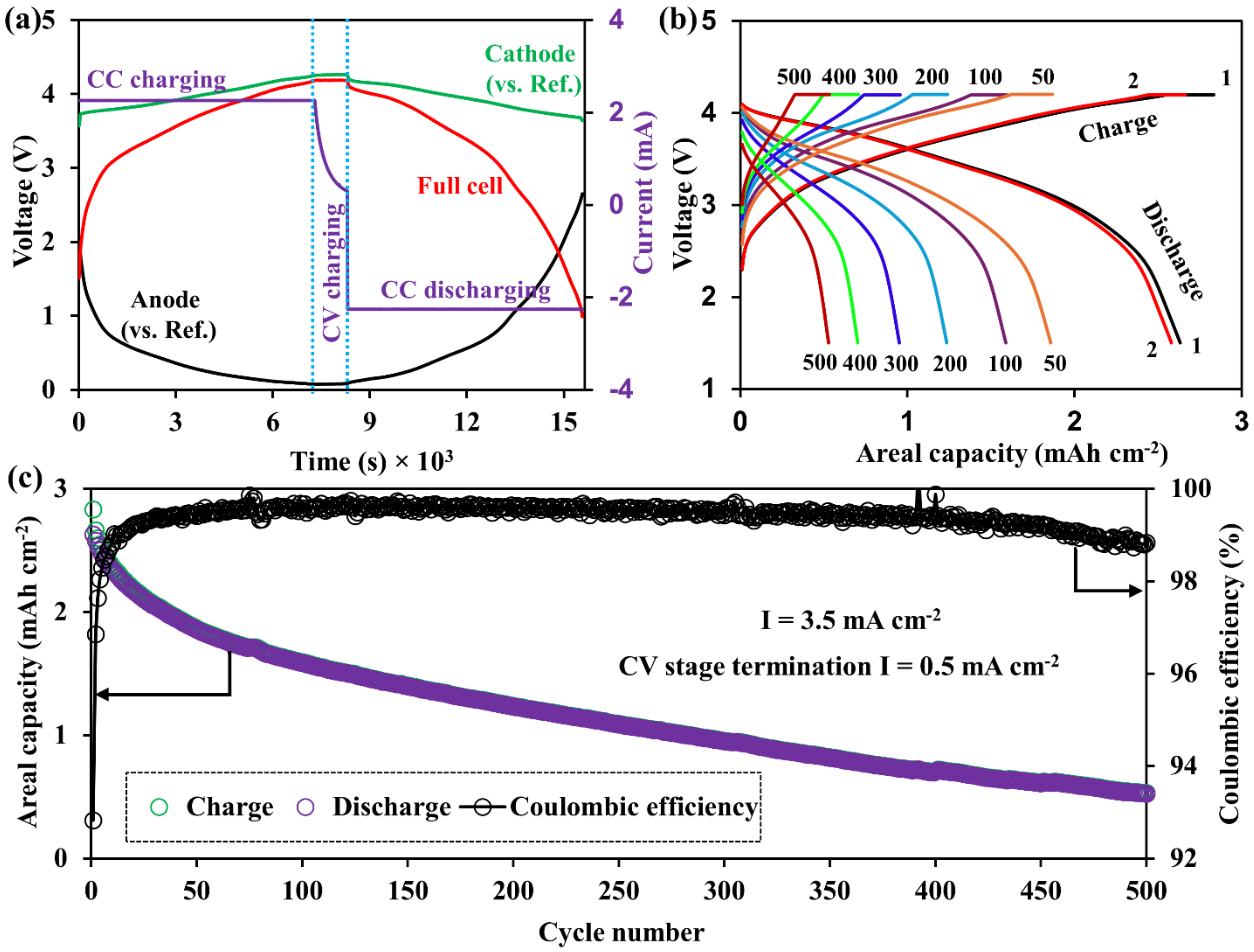

Fig. 7. (a) Current and potential profiles of the SnO_2-VACNTs anode (vs. Li reference), NMC cathode (vs. Li reference) and full cell during the charge/discharge of a three-electrode cell. (b) Charge/discharge potential profiles during different cycles and (c) long-term cycling test of the SnO_2-VACNTs/NMC full cell.

Fig. 7(b) shows the charging and discharging potential profiles of the full cell at different cycles within the potential range of 1.5–4.2 V. During the charging stage, a constant current (CC) of 3.5 mA cm^{-2} was applied until the cell potential reached 4.2 V and then the cell potential was kept constant (CV) until the current reduced to 0.5 mA cm^{-2}. In contrast, the cell was discharged using the constant current (CC) of 3.5 mA cm^{-2} until the cell potential decreased to 1.5 V. The first cycle areal charge and discharge capacities of the full cell were 2.83 mAh cm^{-2}

and 2.63 mAh cm^{-2}, respectively, with an ICE of ~91%, which is much higher than the ICE the SnO_2-VACNTs anode measured in half-cell and can be attributed to the prelithiation. Furthermore, the first areal discharge capacity of the cell is about an industrially acceptable areal capacity level (~3 mAh g^{-1}) [92]. However, the areal capacity rapidly decreased by ~29% after 50 cycles, retained the areal capacity of ~47% after 200 cycles and only ~20% after 500 cycles, as shown in **Figs. 7(c)**, which is significantly low and indicates that the cyclability of the SnO_2-VACNTs anode must be improved for future practical applications. One of the possible reasons for this rapid capacity fade of the SnO_2-VACNTs/NMC full cell can be the detachment of SnO_2 nanoparticles from the VACNTs due to the high charging rate of 2.06 A g^{-1} (or 3.5 mA cm^{-2}). The anode active material loading was significantly increased by increasing the VACNTs growth time and SnO_2 coating time for the full cell testing compared to the anode for half cell testing. The increase in coating time may have increased the SnO_2 coating thickness, making it weakly bonded to the VACNT and vulnerable to detaching from the host VACNT. In addition, it should be noted that the full cell achieved 80, 90, and 100% state of charge in 38, 43, and 56 minutes, respectively, as shown in **Fig. S6** (Supplementary Information). This result indicates that the SnO_2-VACNTs anode may have potential applications in future fast-charging high-energy-density LIBs.

3.3 Anode aging analysis

The SnO_2-VACNTs anode morphology after 500 fast-charged cycles in the full-cell configuration was examined using SEM spectroscopy. As shown in **Figs. 8(a, b)**, the spongy, porous, and aligned morphology of SnO_2-VACNTs remained intact on the Ni foam substrate even after the extended cycling test. This result suggests that VACNTs were strongly connected to the Ni foam current collector as they were directly synthesized on the Ni metal substrate. This inherent connection between the current collector (Ni foam) and active materials (SnO_2-VACNTs) is crucial for developing a binder-free anode. Furthermore, signals related to C, Sn, and O in the SEM-EDS elemental mapping (**Figs. 8(c-e)** and **Fig. 8(h)**) demonstrate the uniform

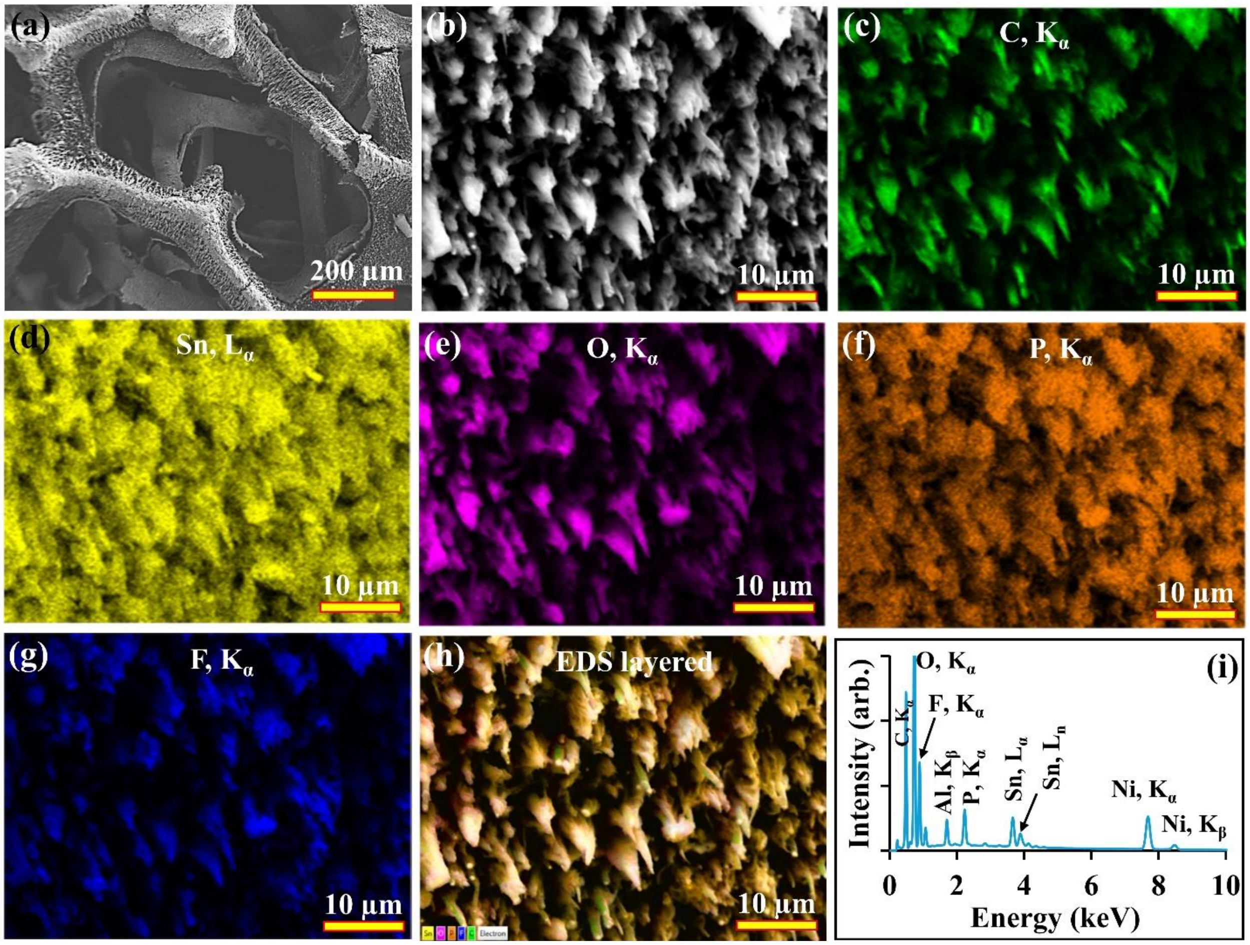

Fig. 8. (a, b) Low and high magnification SEM images, (c-h) SEM-EDS mapping (C, Sn, O, P, F, and their overlap) images, and (i) corresponding EDS spectrum of the SnO_2-VACNTs anode after 500 cycles tested in the full-cell.

distribution of the active materials and are still available in the electrode even after the long cycling for further electrochemical Li^+ storage reaction. As shown in **Figs. 8(f-h)**, the signals P and F should be from the SEI and $LiPF_6$ electrolyte remanents, although the electrode was thoroughly cleaned using DMC before taking SEM images. Also, the Ni and Al signals, as shown in **Fig. 8(i)**, can be attributed to the Ni foam substrate and SEM sample holder, respectively.

The excellent performance of the SnO_2-VACNTs anodes can be ascribed to the following factors: (1) 3D Ni foam host for 1D VACNTs array with the regular pore (inter-VACNTs space) for better electrolyte accessibility; (2) ultra-fine SnO_2 nanoparticles, facilitating the Li^+ diffusion and enhancing the reversible electrochemical lithiation/delithiation reaction; (3) highly conductive VACNTs host for high-capacity SnO_2 materials (SnO_2-VACNTs core-shell structure), increasing conductivity and alleviating electrode pulverization from volume expansion; and (4) innate connection between VACNTs and current collector (binder-free anode), facilitating uninterrupted electron conduction during charge/discharge cycling. Therefore, the SnO_2-VACNTs are promising anode materials for high energy and power density LIBs, although the large initial irreversible capacity loss and cycle instability require further improvement.

4. Conclusions

VACNT arrays have been synthesized directly on 3D Ni foam using the PECVD method to develop free-standing, binder-free VACNTs anode materials. The high-capacity SnO_2-VACNTs core-shell anode was developed by coating the VACNTs wall with ultrafine SnO_2 nanoparticles using a wet-chemical method. The electrochemical properties of the SnO_2 and SnO_2-VACNTs anodes were measured using lithium-ion coin cells in a half-cell configuration. The core-shell structured SnO_2-VACNTs exhibited excellent Li^+ storage properties with a high specific capacity of ~1512 mAh g^{-1} after 100 cycles at a current rate of 0.1 A g^{-1}. The SnO_2-VACNTs anode also demonstrated long-term cycle stability for 200 cycles at a current density of 1 A g^{-1} with a reversible capacity of about 800 mAh g^{-1} with excellent coulombic efficiencies.

The excellent Li^+ storage properties of the SnO_2-VACNTs can be attributed to the ultra-fine SnO_2 particles (< 5 nm) that shortened the diffusion routes of Li^+ and mitigated the volume alteration by minimizing the strains during the Li^+ alloying and dealloying. Also, proper inter-tube distance between individual SnO_2-VACNTs buffered the volume instability and offered better electrolyte accessibility during the lithiation/delithiation process. Furthermore, the direct connection of VACNTs to the Ni foam current collector ensured an uninterrupted electron conducting path between the current collector and active material, thereby offering more efficient charge transport kinetics at the electrode/electrolyte interfaces. Furthermore, the as-synthesized SnO_2-VACNTs anode was assessed in a full cell by pairing with an NMC cathode to understand its practical applications. The strategy presented in this work for synthesizing the three-dimensional SnO_2-VACNTs anode material may pave the way for developing high-performance LIBs.

CRediT authorship contribution statement

Arun Thapa: Conceptualization, Methodology, Investigation, Formal analysis, Writing - original draft, Review & Editing. **Amin Rabiei Baboukani:** Methodology, Discussion, Review & Editing. **Prahald Siwakoti**: Investigation, Discussion, Review & Editing. **Katherine L. Jungjohann:** Investigation, Discussion, Review & Editing. **Chinaza E. Nwanno:** Investigation, Discussion, Review & Editing. **Jiandi Zhang:** Investigation, Discussion, Review & Editing. **Chunlei Wang:** Funding acquisition, Supervision, Review & Editing. **Hongwei Gao:** Funding acquisition, Supervision, Review & Editing. **Wenzhi Li:** Conceptualization, Methodology, Discussion, Validation, Funding acquisition, Supervision, Review & Editing.

Declaration of competing interest

The authors declare the following financial interests/personal relationships which may be considered as potential competing interests:

Wenzhi Li and Arun Thapa have a patent, "**Coated vertically aligned carbon nanotubes on nickel foam**" (US patent 11,476,464). https://patents.google.com/patent/US11476464B1/en).

Acknowledgment

Synthesis of vertically aligned carbon nanotubes (VACNTs), Tin Oxide nanoparticles (SnO_2), and SnO_2 coated VACNTs, characterization of VACNTs and SnO_2-VACNTs by Atomic Force Microscopy, Scanning Electron Microscopy, X-ray Diffraction, Thermogravimetry, Fourier Transform Infrared Spectroscopy, Raman Spectroscopy, fabrication of coin cells at Florida International University, and Cyclic Voltammetry and Charge/Discharge testing of the coin cells were supported by the National Science Foundation under grants 1506640, 2134375, and 2213923 to Florida International University.

Fabrication of coin cells at Montana State University, Electrochemical Impedance Spectroscopy, Charge/Discharge, and Cyclic Voltammetry tests of the cells, and post-analysis of electrodes of the cells by Scanning Electron Microscopy were supported by the financial support from the DEVCOM Army Research Laboratory (ARL) under Cooperative Agreement (CA) Number W911NF-20-2-0284. The views and conclusions contained in this document are those of the authors and should not be interpreted as representing the official policies, either expressed or implied, of the DEVCOM Army Research Laboratory or the U.S. Government. The U.S. Government is authorized to reproduce and distribute reprints for Government purposes notwithstanding any copyright notation hereon.

Transmission Electron Microscopy was performed at the Center for Integrated Nanotechnologies, an Office of Science User Facility operated for the U.S. Department of Energy (DOE) Office of Science. Sandia National Laboratories is a multi-mission laboratory managed and operated by National Technology and Engineering Solutions of Sandia, LLC., a wholly owned subsidiary of Honeywell International, Inc., for the U.S. DOE's National Nuclear Security Administration under contract DE-NA-0003525. This paper describes objective technical results and analysis. Any subjective views or opinions that might be expressed in the paper do not necessarily represent the views of the U.S. Department of Energy or the United States Government.

Post-analysis of electrodes by Scanning Electron Microscopy was performed at the Montana Nanotechnology Facility, a member of the National Nanotechnology Coordinated Infrastructure (NNCI), which is supported by the National Science Foundation (Grant # ECCS-2025391). The authors would also like to acknowledge the support from the Advanced Materials Engineering Research Institutes (AMERI) at Florida International University (FIU).

Data availability

The raw/processed data required to reproduce these findings cannot be shared at this time as the data also forms part of an ongoing study.

References

1. M.V. Reddy, A. Mauger, C.M. Julien, A. Paolella, and K. Zaghib *Brief History of Early Lithium-Battery Development*. Materials, 2020. **13**. https://doi.org/10.3390/ma13081884
2. M. Li, J. Lu, Z. Chen, and K. Amine, *30 Years of Lithium-Ion Batteries.* **Advanced Materials**, **2018**. 30(33): p. 1800561. https://doi.org/10.1002/adma.201800561
3. T. Kim, W. Song, D.-Y. Son, L.K. Ono, and Y. Qi, *Lithium-ion batteries: outlook on present, future, and hybridized technologies.* **Journal of Materials Chemistry A**, **2019**. 7(7): p. 2942-2964. https://doi.org/10.1039/C8TA10513H

4. W. Cai, Y.-X. Yao, G.-L. Zhu, C. Yan, L.-L. Jiang, C. He, J.-Q. Huang, and Q. Zhang, *A review on energy chemistry of fast-charging anodes.* **Chemical Society Reviews**, **2020**. 49(12): p. 3806-3833. https://doi.org/10.1039/C9CS00728H

5. Y. Li, Y. Lu, P. Adelhelm, M.-M. Titirici, and Y.-S. Hu, *Intercalation chemistry of graphite: alkali metal ions and beyond.* **Chemical Society Reviews**, **2019**. 48(17): p. 4655-4687. https://doi.org/10.1039/C9CS00162J

6. B. Zhao, Z. Wang, S. Wang, J. Jiang, J. Si, S. Huang, Z. Chen, W. Li, and Y. Jiang, *Sandwiched spherical tin dioxide/graphene with a three-dimensional interconnected closed pore structure for lithium storage.* **Nanoscale**, **2018**. 10(34): p. 16116-16126. https://doi.org/10.1039/C8NR03776K

7. P. Wang, M. Gao, H. Pan, J. Zhang, C. Liang, J. Wang, P. Zhou, and Y. Liu, *A facile synthesis of Fe3O4/C composite with high cycle stability as anode material for lithium-ion batteries.* **Journal of Power Sources**, **2013**. 239: p. 466-474. https://doi.org/10.1016/j.jpowsour.2013.03.073

8. C.-L. Zhang, B.-R. Lu, F.-H. Cao, Z.-L. Yu, H.-P. Cong, and S.-H. Yu, *Hierarchically structured Co3O4@carbon porous fibers derived from electrospun ZIF-67/PAN nanofibers as anodes for lithium ion batteries.* **Journal of Materials Chemistry A**, **2018**. 6(27): p. 12962-12968. 10.1039/C8TA03397H

9. T. Chen, Y. Hu, B. Cheng, R. Chen, H. Lv, L. Ma, G. Zhu, Y. Wang, C. Yan, Z. Tie, Z. Jin, and J. Liu, *Multi-yolk-shell copper oxide@carbon octahedra as high-stability anodes for lithium-ion batteries.* **Nano Energy**, **2016**. 20: p. 305-314. https://doi.org/10.1016/j.nanoen.2015.12.024

10. F. Xie, M. Sun, X. Sheng, Q. Zhang, Z. Ling, S. Hao, F. Diao, and Y. Wang, *Graphene-wrapped Fe2TiO5 nanoparticles with enhanced performance as lithium-ion battery anode.* **Materials Letters**, **2024**. 358: p. 135877. https://doi.org/10.1016/j.matlet.2024.135877

11. S. Hao, X. Sheng, F. Xie, M. Sun, F. Diao, and Y. Wang, *Electrospun carbon nanofibers embedded with heterostructured NiFe2O4/Fe0.64Ni0.36 nanoparticles as an anode for high-performance lithium-ion battery.* **Journal of Energy Storage**, **2024**. 80: p. 110412. https://doi.org/10.1016/j.est.2023.110412

12. Y. Pang, J. Wang, J. Yang, F. Fang, D. Sun, and S. Zheng, *Fully reversible lithium storage of tin oxide enabled by self-doping and partial amorphization.* **Nanoscale**, **2019**. 11(27): p. 12915-12923. https://doi.org/10.1039/C9NR03445E

13. C.-M. Wang, W. Xu, J. Liu, J.-G. Zhang, L.V. Saraf, B.W. Arey, D. Choi, Z.-G. Yang, J. Xiao, and S. Thevuthasan, *In situ transmission electron microscopy observation of microstructure and phase evolution in a SnO2 nanowire during lithium intercalation.* **Nano Letters**, **2011**. 11(5): p. 1874-1880. https://doi.org/10.1021/nl200272n

14. R. Demir-Cakan, Y.-S. Hu, M. Antonietti, J. Maier, and M.-M. Titirici, *Facile One-Pot Synthesis of Mesoporous SnO2 Microspheres via Nanoparticles Assembly and Lithium Storage Properties.* **Chemistry of Materials**, **2008**. 20(4): p. 1227-1229. https://doi.org/10.1021/cm7031288

15. Z. Chen, M. Zhou, Y. Cao, X. Ai, H. Yang, and J. Liu, *In Situ Generation of Few-Layer Graphene Coatings on SnO2-SiC Core-Shell Nanoparticles for High-Performance*

Lithium-Ion Storage. **Advanced Energy Materials**, **2012**. 2(1): p. 95-102. https://doi.org/10.1002/aenm.201100464

16. B. Huang, X. Li, Y. Pei, S. Li, X. Cao, R.C. Massé, and G. Cao, *Novel Carbon-Encapsulated Porous SnO2 Anode for Lithium-Ion Batteries with Much Improved Cyclic Stability.* **Small**, **2016**. 12(14): p. 1945-1955. https://doi.org/10.1002/smll.201503419

17. X. Wang, X. Cao, L. Bourgeois, H. Guan, S. Chen, Y. Zhong, D.-M. Tang, H. Li, T. Zhai, L. Li, Y. Bando, and D. Golberg, *N-Doped Graphene-SnO2 Sandwich Paper for High-Performance Lithium-Ion Batteries.* **Advanced Functional Materials**, **2012**. 22(13): p. 2682-2690. https://doi.org/10.1002/adfm.201103110

18. L. Zhang, H.B. Wu, B. Liu, and X.W. Lou, *Formation of porous SnO2 microboxes via selective leaching for highly reversible lithium storage.* **Energy & Environmental Science**, **2014**. 7(3): p. 1013-1017. https://doi.org/10.1039/C3EE43305F

19. W. Yue, S. Jiang, W. Huang, Z. Gao, J. Li, Y. Ren, X. Zhao, and X. Yang, *Sandwich-structural graphene-based metal oxides as anode materials for lithium-ion batteries.* **Journal of Materials Chemistry A**, **2013**. 1(23): p. 6928-6933. https://doi.org/10.1039/C3TA11012E

20. X. Han, X. Wu, Y. Deng, J. Liu, J. Lu, C. Zhong, and W. Hu, *Ultrafine Pt Nanoparticle-Decorated Pyrite-Type CoS2 Nanosheet Arrays Coated on Carbon Cloth as a Bifunctional Electrode for Overall Water Splitting.* **Advanced Energy Materials**, **2018**. 8(24): p. 1800935. https://doi.org/10.1002/aenm.201800935

21. J.-H. Lee, G.-S. Kim, Y.-M. Choi, W.I. Park, J.A. Rogers, and U. Paik, *Comparison of multiwalled carbon nanotubes and carbon black as percolative paths in aqueous-based natural graphite negative electrodes with high-rate capability for lithium-ion batteries.* **Journal of power sources**, **2008**. 184(1): p. 308. https://doi.org/10.1016/j.jpowsour.2008.05.090

22. X.M. Liu, Z.D. Huang, S.W. Oh, B. Zhang, P.C. Ma, M.M. Yuen, and J.K. Kim, *Carbon nanotube (CNT)-based composites as electrode material for rechargeable Li-ion batteries: a review.* **Composites Science and Technology**, **2012**. 72(2): p. 121. https://doi.org/10.1016/j.compscitech.2011.11.019

23. W. Zhang, Y. Liu, Z.-q. Ye, M. Yang, Q. Luo, J. Dai, Q.-f. Wang, and L. Liu, *Porous nitrogen-doped FeP/C nanofibers as promising anode for potassium-ion batteries.* **Journal of Central South University**, **2023**. 30(10): p. 3248-3259. https://doi.org/10.1007/s11771-023-5380-y

24. C.E. Nwanno and W. Li, *Aligned carbon nanotubes for lithium-ion batteries: A review.* **Nano Research**, **2023**. 16(11): p. 12384-12410. https://doi.org/10.1007/s12274-023-6006-2

25. T. Li, S. Gao, K. Li, G. Liu, X. Sheng, D. Shang, L. Wu, S. Chen, Y. Wang, and S. Wu, *Tailoring the phase evolution of molybdenum-based nanocrystals in carbon nanofibers for enhanced performance of lithium-ion batteries.* **Journal of Alloys and Compounds**, **2023**. 934: p. 168042. https://doi.org/10.1016/j.jallcom.2022.168042

26. W.-Q. Han and A. Zettl, *Coating Single-Walled Carbon Nanotubes with Tin Oxide.* **Nano Letters**, **2003**. 3(5): p. 681-683. https://doi.org/10.1021/nl034142d

27. J. Wang, X. Sheng, S. Hao, G. Liu, R. Cai, X. Xue, and Y. Wang, *Construction of Fe0.64Ni0.36@graphite nanoparticles via corrosion-like transformation from NiFe2O4 and surface graphitization in flexible carbon nanofibers to achieve strong wideband microwave absorption.* **Journal of Colloid and Interface Science**, **2024**. 657: p. 193-207. https://doi.org/10.1016/j.jcis.2023.11.145

28. L. Noerochim, J.Z. Wang, S.L. Chou, D. Wexler, and H.K. Liu, *Free-standing single-walled carbon nanotube/SnO2 anode paper for flexible lithium-ion batteries.* **Carbon**, **2012**. 50(3): p. 1289. https://doi.org/10.1016/j.carbon.2011.10.049

29. B. Zhang, J. Huang, and J.K. Kim, *Ultrafine Amorphous SnOx Embedded in Carbon Nanofiber/Carbon Nanotube Composites for Li-Ion and Na-Ion Batteries.* **Advanced Functional Materials**, **2015**. 25(32): p. 5222. https://doi.org/10.1002/adfm.201501498

30. C. Ma, W. Zhang, Y.-S. He, Q. Gong, H. Che, and Z.-F. Ma, *Carbon coated SnO 2 nanoparticles anchored on CNT as a superior anode material for lithium-ion batteries.* **Nanoscale**, **2016**. 8(7): p. 4121. https://doi.org/10.1039/C5NR07996A

31. B.J. Landi, M.J. Ganter, C.D. Cress, R.A. DiLeo, and R.P. Raffaelle, *Carbon nanotubes for lithium ion batteries.* **Energy & Environmental Science**, **2009**. 2(6): p. 638. https://doi.org/10.1039/B904116H

32. L. Sun, X. Wang, R.A. Susantyoko, and Q. Zhang, *High performance binder-free Sn coated carbon nanotube array anode.* **Carbon**, **2015**. 82: p. 282-287. https://doi.org/10.1016/j.carbon.2014.10.072

33. R.A. Susantyoko, X. Wang, L. Sun, K.L. Pey, E. Fitzgerald, and Q. Zhang, *Germanium coated vertically-aligned multiwall carbon nanotubes as lithium-ion battery anodes.* **Carbon**, **2014**. 77: p. 551-559. https://doi.org/10.1016/j.carbon.2014.05.060

34. Y. Fan, Q. Zhang, Q. Xiao, X. Wang, and K. Huang, *High performance lithium ion battery anodes based on carbon nanotube–silicon core–shell nanowires with controlled morphology.* **Carbon**, **2013**. 59: p. 264-269. https://doi.org/10.1016/j.carbon.2013.03.017

35. J. Xia, L. Liu, S. Jamil, J. Xie, H. Yan, Y. Yuan, Y. Zhang, S. Nie, J. Pan, X. Wang, and G. Cao, *Free-standing SnS/C nanofiber anodes for ultralong cycle-life lithium-ion batteries and sodium-ion batteries.* **Energy Storage Materials**, **2019**. 17: p. 1-11. https://doi.org/10.1016/j.ensm.2018.08.005

36. A. Thapa, S. Neupane, R. Guo, K.L. Jungjohann, D. Pete, and W. Li, *Direct growth of vertically aligned carbon nanotubes on stainless steel by plasma enhanced chemical vapor deposition.* **Diamond and Related Materials**, **2018**. 90: p. 144. https://doi.org/10.1016/j.diamond.2018.10.012

37. S. Talapatra, S. Kar, S.K. Pal, R. Vajtai, L. Ci, P. Victor, M.M. Shaijumon, S. Kaur, O. Nalamasu, and P.M. Ajayan, *Direct growth of aligned carbon nanotubes on bulk metals.* **Nature Nanotechnology**, **2006**. 1(2): p. 112-116. https://doi.org/10.1038/nnano.2006.56

38. E. Piperopoulos, L. Calabrese, A. Khaskhoussi, E. Proverbio, and C. Milone *Thermo-Physical Characterization of Carbon Nanotube Composite Foam for Oil Recovery Applications*. Nanomaterials, 2020. **10**. https://doi.org/10.3390/nano10010086

39. L. Noerochim, J.-Z. Wang, S.-L. Chou, H.-J. Li, and H.-K. Liu, *SnO2-coated multiwall carbon nanotube composite anode materials for rechargeable lithium-ion batteries.* **Electrochimica Acta**, **2010**. 56(1): p. 314-320. https://doi.org/10.1016/j.electacta.2010.08.078

40. R.S. Hsu, D. Higgins, and Z. Chen, *Tin-oxide-coated single-walled carbon nanotube bundles supporting platinum electrocatalysts for direct ethanol fuel cells.* **Nanotechnology**, **2010**. 21(16): p. 165705. https://doi.org/10.1088/0957-4484/21/16/165705

41. M.S. Dresselhaus, G. Dresselhaus, R. Saito, and A. Jorio, *Raman spectroscopy of carbon nanotubes.* **Physics reports**, **2005**. 409(2): p. 47. https://doi.org/10.1016/j.physrep.2004.10.006

42. Z. Xiong, Y.S. Yun, and H.-J. Jin *Applications of Carbon Nanotubes for Lithium Ion Battery Anodes*. Materials, 2013. **6**, 1138-1158. https://doi.org/10.3390/ma6031138

43. C. Garau, A. Frontera, D. Quiñonero, A. Costa, P. Ballester, and P.M. Deyà, *Lithium diffusion in single-walled carbon nanotubes: a theoretical study.* **Chemical Physics Letters**, **2003**. 374(5): p. 548-555. https://doi.org/10.1016/S0009-2614(03)00748-6

44. K.M. Lee, D.J. Lee, and H. Ahn, *XRD and TEM studies on tin oxide (II) nanoparticles prepared by inert gas condensation.* **Materials Letters**, **2004**. 58(25): p. 3122. https://doi.org/10.1016/j.matlet.2004.06.002

45. T.W. Ebbesen, H. Hiura, M.E. Bisher, M.M. Treacy, J.L. Shreeve-Keyer, and R.C. Haushalter, *Decoration of carbon nanotubes.* **Advanced Materials**, **1996**. 8(2): p. 155. https://doi.org/10.1002/adma.19960080212

46. K. Balasubramanian and M. Burghard, *Chemically functionalized carbon nanotubes.* **small**, **2005**. 1(2): p. 180. https://doi.org/10.1002/smll.200400118

47. R. Pandiyan, S. Mahalingam, and Y.H. Ahn, *Antibacterial and photocatalytic activity of hydrothermally synthesized SnO2 doped GO and CNT under visible light irradiation.* **Journal of Photochemistry and Photobiology B: Biology**, **2019**. 191: p. 18. https://doi.org/10.1016/j.jphotobiol.2018.12.007

48. Z. Ling, F. Diao, X. Sheng, T. Li, R. Cai, and Y. Wang, *Chemical reaction and phase transformation mechanism of electrospun iron (III) acetylacetonate-polyacrylonitrile fibers during pre-oxidation process.* **Chemical Physics Letters**, **2023**. 832: p. 140866. https://doi.org/10.1016/j.cplett.2023.140866

49. F. Xie, X. Sheng, Z. Ling, S. Hao, Q. Zhang, M. Sun, G. Liu, F. Diao, and Y. Wang, *Flexible electrospun iron/manganese-based compounds/carbon fibers: Phase transformation and electrochemical properties.* **Electrochimica Acta**, **2023**. 470: p. 143288. https://doi.org/10.1016/j.electacta.2023.143288

50. S. Motshekga, S.K. Pillai, and S.S. Ray, *Conventional wet impregnation versus microwave-assisted synthesis of SnO 2/CNT composites.* **Journal of Nanoparticle Research**, **2011**. 13(3): p. 1093. https://doi.org/10.1007/s11051-010-0098-9

51. J. Zhu, Z. Lu, S. Aruna, D. Aurbach, and A. Gedanken, *Sonochemical synthesis of SnO2 nanoparticles and their preliminary study as Li insertion electrodes.* **Chemistry of Materials**, **2000**. 12(9): p. 2557. https://doi.org/10.1021/cm990683l

52. B. Huang, J. Yang, Y. Zou, L. Ma, and X. Zhou, *Sonochemical synthesis of SnO2/carbon nanotubes encapsulated in graphene sheets composites for lithium ion batteries with superior electrochemical performance.* **Electrochimica Acta**, **2014**. 143: p. 63-69. https://doi.org/10.1016/j.electacta.2014.07.119

53. V. Kumar, V. Kumar, S. Som, J.H. Neethling, E. Olivier, O.M. Ntwaeaborwa, and H.C. Swart, *The role of surface and deep-level defects on the emission of tin oxide quantum dots.* **Nanotechnology**, **2014**. 25(13): p. 135701. https://doi.org/10.1088/0957-4484/25/13/135701

54. X. Liu, Y. Jiang, K. Li, F. Xu, P. Zhang, and Y. Ding, *Electrospun free-standing N-doped C@SnO2 anode paper for flexible Li-ion batteries.* **Materials Research Bulletin**, **2019**. 109: p. 41-48. https://doi.org/10.1016/j.materresbull.2018.09.023

55. Q. Tian, F. Zhang, W. Zhang, and L. Yang, *Non-smooth carbon coating porous SnO2 quasi-nanocubes towards high lithium storage.* **Electrochimica Acta**, **2019**. 307: p. 393-402. https://doi.org/10.1016/j.electacta.2019.04.004

56. B. Zhou, S. Yang, L. Wu, W. Wu, W. Wei, L. Chen, H. Zhang, J. Pan, and X. Xiong, *Amorphous carbon framework stabilized SnO2 porous nanowires as high performance Li-ion battery anode materials.* **RSC Advances**, **2015**. 5(62): p. 49926-49932. https://doi.org/10.1039/C5RA05372B

57. D. Hernandez, F. Mendoza, E. Febus, B.R. Weiner, and G. Morell, *Binder free SnO2-CNT composite as anode material for Li-Ion battery.* **Journal of Nanotechnology**, **2014**. 2014: p. 381273. https://doi.org/10.1155/2014/381273

58. J. Zhang, Y. Zhu, C. Cao, and F.K. Butt, *Microwave-assisted and large-scale synthesis of SnO 2/carbon-nanotube hybrids with high lithium storage capacity.* **RSC Advances**, **2015**. 5(72): p. 58568. https://doi.org/10.1039/C5RA10314B

59. J. Zhao, A. Buldum, J. Han, and J. Ping Lu, *First-Principles Study of Li-Intercalated Carbon Nanotube Ropes.* **Physical Review Letters**, **2000**. 85(8): p. 1706-1709. https://doi.org/10.1103/PhysRevLett.85.1706

60. K. Nishidate and M. Hasegawa, *Energetics of lithium ion adsorption on defective carbon nanotubes.* **Physical Review B**, **2005**. 71(24): p. 245418. https://doi.org/10.1103/PhysRevB.71.245418

61. B.J. Landi, M.J. Ganter, C.D. Cress, R.A. DiLeo, and R.P. Raffaelle, *Carbon nanotubes for lithium ion batteries.* **Energy & Environmental Science**, **2009**. 2(6): p. 638-654. https://doi.org/10.1039/B904116H

62. H. Xu, L. Shi, Z. Wang, J. Liu, J. Zhu, Y. Zhao, M. Zhang, and S. Yuan, *Fluorine-Doped Tin Oxide Nanocrystal/Reduced Graphene Oxide Composites as Lithium Ion Battery Anode Material with High Capacity and Cycling Stability.* **ACS Applied Materials & Interfaces**, **2015**. 7(49): p. 27486-27493. https://doi.org/10.1021/acsami.5b09538

63. F. Mueller, D. Bresser, V.S.K. Chakravadhanula, and S. Passerini, *Fe-doped SnO2 nanoparticles as new high capacity anode material for secondary lithium-ion batteries.* **Journal of Power Sources**, **2015**. 299: p. 398-402. https://doi.org/10.1016/j.jpowsour.2015.08.018

64. Y.F. Zhukovskii, E.A. Kotomin, P. Balaya, and J. Maier, *Enhanced interfacial lithium storage in nanocomposites of transition metals with LiF and Li2O: Comparison of DFT calculations and experimental studies.* **Solid State Sciences**, **2008**. 10(4): p. 491-495. https://doi.org/10.1016/j.solidstatesciences.2007.12.030

65. M.R. Smith, P.L. Johnson, and D. Teeters, *Interfacial storage of lithium in the nanostructure of SnO2 nanobaskets for capacities exceeding theoretical values.* **Solid State Ionics**, **2012**. 225: p. 680-684. https://doi.org/10.1016/j.ssi.2011.11.022

66. L. Ji, Z. Tan, T. Kuykendall, E.J. An, Y. Fu, V. Battaglia, and Y. Zhang, *Multilayer nanoassembly of Sn-nanopillar arrays sandwiched between graphene layers for high-capacity lithium storage.* **Energy & Environmental Science**, **2011**. 4(9): p. 3611. https://doi.org/10.1039/C1EE01592C

67. W. Lu, A. Goering, L. Qu, and L. Dai, *Lithium-ion batteries based on vertically-aligned carbon nanotube electrodes and ionic liquid electrolytes.* **Physical Chemistry Chemical Physics**, **2012**. 14(35): p. 12099. https://doi.org/10.1039/c2cp40726d

68. Z. Wang, G. Chen, and D. Xia, *Coating of multi-walled carbon nanotube with SnO2 films of controlled thickness and its application for Li-ion battery.* **Journal of power sources**, **2008**. 184(2): p. 432. https://doi.org/10.1016/j.jpowsour.2008.03.028

69. J. Gao, R. Huang, D. Yang, K. Wu, D. Xiong, Z. Feng, M. He, and Y. Feng, *Molybdenum-fluorine-doped SnO2 nanoparticles based on 3D interconnected carbon structure as matrix as high-performance lithium-ion anode material.* **Ionics**, **2022**. 28(10): p. 4587-4597. https://doi.org/10.1007/s11581-022-04717-x

70. Y. Guo, Y. Hu, Q. Zhang, G. Ruan, Y. Mao, H. Zhang, R. Wang, P. Zhao, M. Li, H. Tang, D. Zhang, L. Xu, M. Jin, K. Ding, and B. Wang, *Fabrication of SnO2 micron-rods embedding in 3D composite of graphene oxide@MWNTs as high-performance anode for lithium-ion batteries.* **Journal of Energy Storage**, **2023**. 74: p. 109479. https://doi.org/10.1016/j.est.2023.109479

71. C. Zhao, Z. Wei, J. Zhang, P. He, X. Huang, X. Duan, D. Jia, and Y. Zhou, *Ultrafine SnO2 nanoparticles on delaminated MXene nanosheets as an anode for lithium-ion batteries.* **Journal of Alloys and Compounds**, **2022**. 907: p. 164428. https://doi.org/10.1016/j.jallcom.2022.164428

72. D. Jiang, C. Wang, L. Sun, X. Xu, B. Wu, and X. Chen, *Facile Hydrothermal Synthesis of SnO2 Nanoparticles with Enhanced Lithium Storage Performance.* **Chemistry Letters**, **2017**. 46(11): p. 1639-1642. https://doi.org/10.1246/cl.170757

73. Z. Shen, Y. Hu, Y. Chen, X. Zhang, K. Wang, and R. Chen, *Tin nanoparticle-loaded porous carbon nanofiber composite anodes for high current lithium-ion batteries.* **Journal of Power Sources**, **2015**. 278: p. 660-667. https://doi.org/10.1016/j.jpowsour.2014.12.106

74. B. Han, W. Zhang, D. Gao, C. Zhou, K. Xia, Q. Gao, and J. Wu, *Encapsulating tin oxide nanoparticles into holey carbon nanotubes by melt infiltration for superior lithium and*

sodium ion storage. **Journal of Power Sources**, **2020**. 449: p. 227564. https://doi.org/10.1016/j.jpowsour.2019.227564

75. F. Zoller, K. Peters, P.M. Zehetmaier, P. Zeller, M. Döblinger, T. Bein, Z.k. Sofer, and D. Fattakhova-Rohlfing, *Making Ultrafast High-Capacity Anodes for Lithium-Ion Batteries via Antimony Doping of Nanosized Tin Oxide/Graphene Composites.* **Advanced Functional Materials**, **2018**. 28(23): p. 1706529. https://doi.org/10.1002/adfm.201706529

76. F. Kenji, K. Kazuhiko, I. Kennichi, and Y. Masaki, *Foliated natural graphite as the anode material for rechargeable lithium-ion cells.* **Journal of Power Sources**, **1997**. 69(1): p. 165-168. https://doi.org/10.1016/S0378-7753(97)02568-8

77. S. Zhang and P. Shi, *Electrochemical impedance study of lithium intercalation into MCMB electrode in a gel electrolyte.* **Electrochimica Acta**, **2004**. 49(9): p. 1475-1482. https://doi.org/10.1016/j.electacta.2003.10.033

78. D. Chen, S. Sun, G. Yu, L. Qin, W. Wang, M. Jiang, and J. Chen, *In-situ thermally fabricated porous and heterogeneous yolk-shell selenides wrapped in carbon as anode for high-performance hybrid lithium-ion capacitors.* **Carbon**, **2020**. 166: p. 91-100. https://doi.org/10.1016/j.carbon.2020.05.008

79. L.G. Bulusheva, A.V. Okotrub, A.G. Kurenya, H. Zhang, H. Zhang, X. Chen, and H. Song, *Electrochemical properties of nitrogen-doped carbon nanotube anode in Li-ion batteries.* **Carbon**, **2011**. 49(12): p. 4013. https://doi.org/10.1016/j.carbon.2011.05.043

80. J. Guo, A. Sun, X. Chen, C. Wang, and A. Manivannan, *Cyclability study of silicon–carbon composite anodes for lithium-ion batteries using electrochemical impedance spectroscopy.* **Electrochimica Acta**, **2011**. 56(11): p. 3981-3987. https://doi.org/10.1016/j.electacta.2011.02.014

81. J.Y. Song, H.H. Lee, Y.Y. Wang, and C.C. Wan, *Two- and three-electrode impedance spectroscopy of lithium-ion batteries.* **Journal of Power Sources**, **2002**. 111(2): p. 255-267. https://doi.org/10.1016/S0378-7753(02)00310-5

82. K.-H. Chen, K.N. Wood, E. Kazyak, W.S. LePage, A.L. Davis, A.J. Sanchez, and N.P. Dasgupta, *Dead lithium: mass transport effects on voltage, capacity, and failure of lithium metal anodes.* **Journal of Materials Chemistry A**, **2017**. 5(23): p. 11671-11681. https://doi.org/10.1039/C7TA00371D

83. C.-H. Kim, S.-I. Pyun, and J.-H. Kim, *An investigation of the capacitance dispersion on the fractal carbon electrode with edge and basal orientations.* **Electrochimica Acta**, **2003**. 48(23): p. 3455-3463. https://doi.org/10.1016/S0013-4686(03)00464-X

84. V.J. Ovejas and A. Cuadras *Impedance Characterization of an LCO-NMC/Graphite Cell: Ohmic Conduction, SEI Transport and Charge-Transfer Phenomenon*. Batteries, 2018. **4**. https://doi.org/10.3390/batteries4030043

85. L. Wang, B. Zhang, Y. Hu, X. Li, and T. Zhao, *Failure analysis of LiNi0·83Co0·12Mn0·05O2/graphite–SiOx pouch batteries cycled at high temperature.* **Journal of Power Sources**, **2021**. 482: p. 228978. https://doi.org/10.1016/j.jpowsour.2020.228978

86. M. Ma, A.N. Mansour, J.K. Ko, G.H. Waller, and C.E. Hendricks, *Characterization of Li Diffusion and Solid Electrolyte Interface for Li4Ti5O12 Electrode Cycled with an Organosilicon Additive Electrolyte.* **Journal of The Electrochemical Society**, **2020**. 167(11): p. 110549. https://doi.org/10.1149/1945-7111/aba5d3

87. I.A. Courtney and J. Dahn, *Electrochemical and in situ X-ray diffraction studies of the reaction of lithium with tin oxide composites.* **Journal of the Electrochemical Society**, **1997**. 144(6): p. 2045. https://doi.org/10.1149/1.1837740

88. T. Brousse, R. Retoux, U. Herterich, and D.M. Schleich, *Thin-Film Crystalline SnO2-Lithium Electrodes.* **Journal of The Electrochemical Society**, **1998**. 145(1): p. 1. https://doi.org/10.1149/1.1838201

89. R.A. Huggins and W.D. Nix, *Decrepitation model for capacity loss during cycling of alloys in rechargeable electrochemical systems.* **Ionics**, **2000**. 6(1): p. 57-63. https://doi.org/10.1007/BF02375547

90. X. Li, X. Sun, X. Hu, F. Fan, S. Cai, C. Zheng, and G.D. Stucky, *Review on comprehending and enhancing the initial Coulombic efficiency of anode materials in lithium-ion/sodium-ion batteries.* **Nano Energy**, **2020**. 77: p. 105143. https://doi.org/10.1016/j.nanoen.2020.105143

91. C. Zhao, Z. Yang, X. Zhou, Z. Hao, J. Chen, Z. Wang, X. Chen, X. Wu, L. Li, L. Li, L. Jiao, and S. Chou, *Recent Progress on Electrolyte Boosting Initial Coulombic Efficiency in Lithium-Ion Batteries.* **Advanced Functional Materials**, **2024**. 34(5): p. 2303457. https://doi.org/10.1002/adfm.202303457

92. M. Ge, C. Cao, G.M. Biesold, C.D. Sewell, S.-M. Hao, J. Huang, W. Zhang, Y. Lai, and Z. Lin, *Recent Advances in Silicon-Based Electrodes: From Fundamental Research toward Practical Applications.* **Advanced Materials**, **2021**. 33(16): p. 2004577. https://doi.org/10.1002/adma.202004577

Graphical Abstract

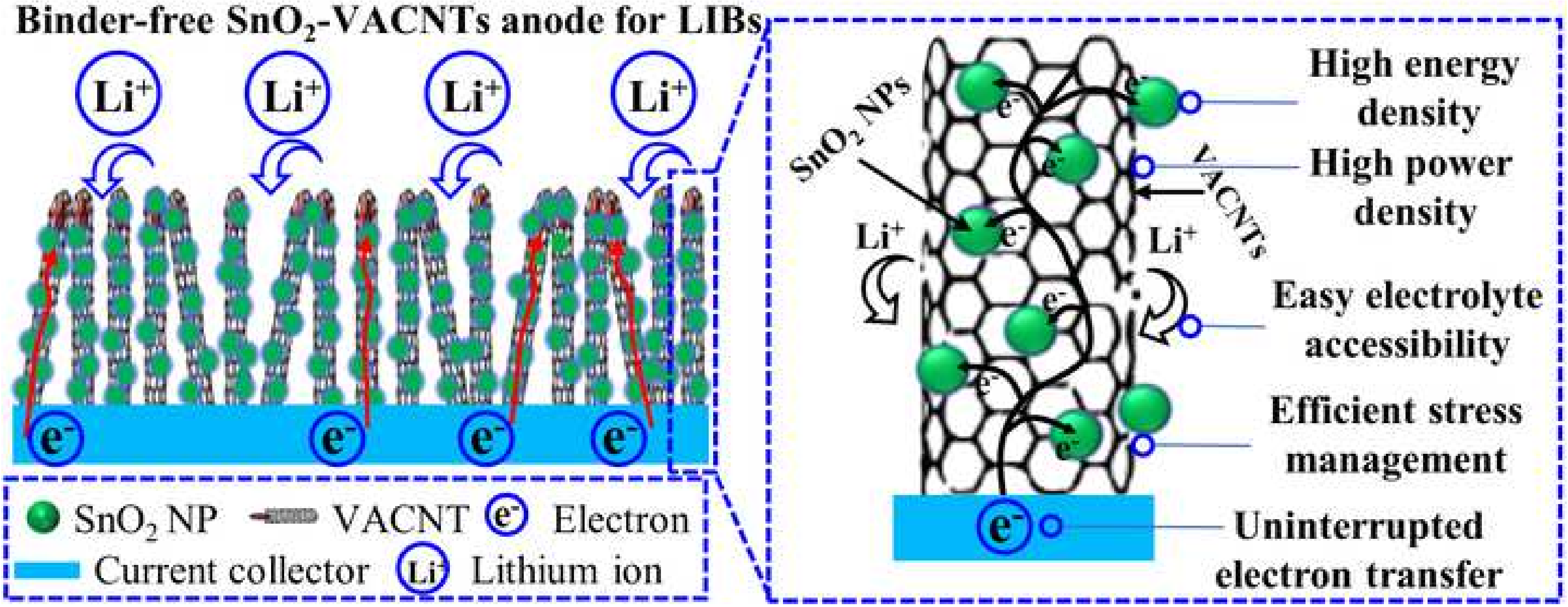

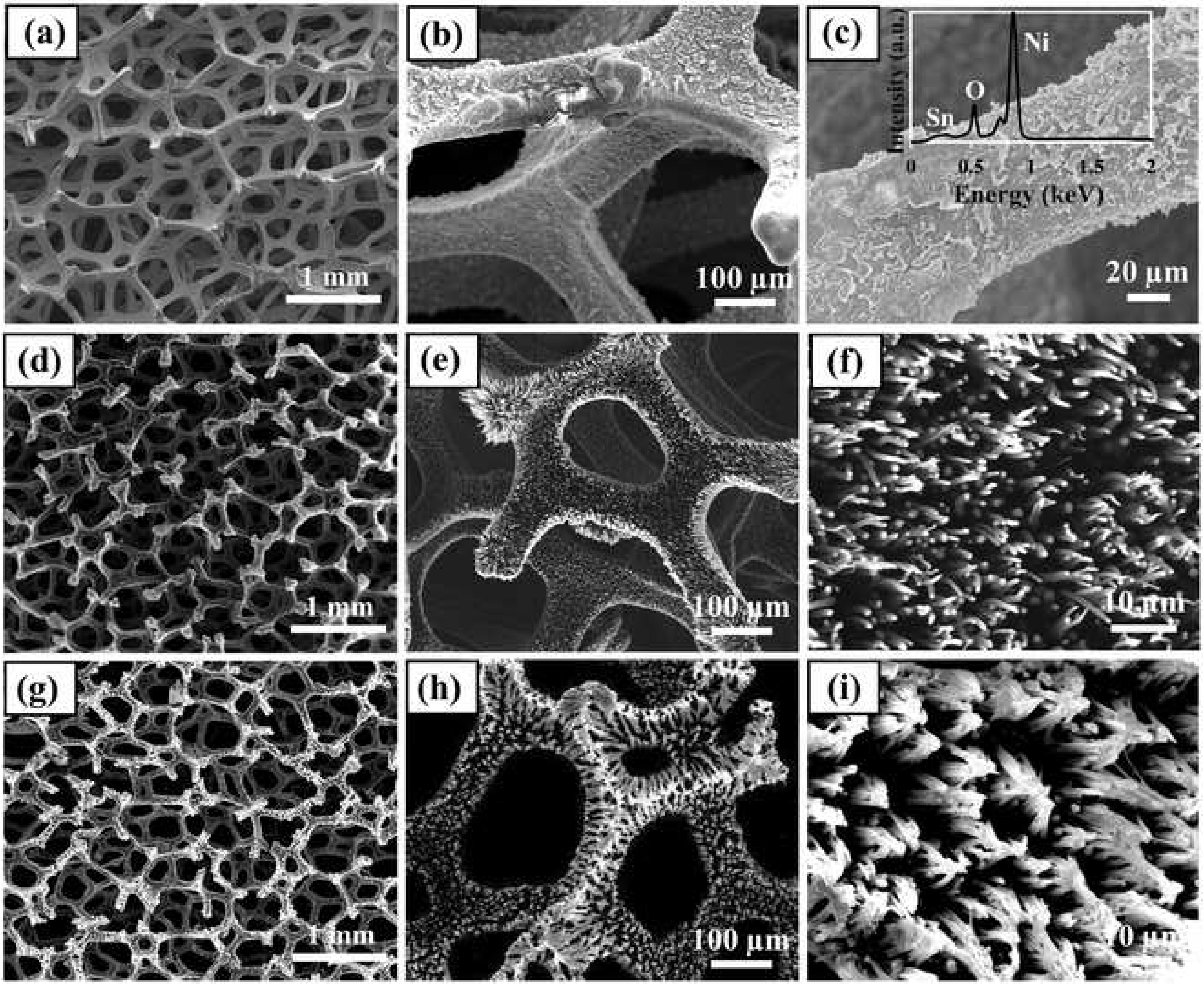
(a)
1 mm
(b)
100 μm
(c)
Intensity (a.u.)
Ni
O
Sn
0
0.5
1
1.5
2
Energy (keV)
20 μm
(d)
1 mm
(e)
100 μm
(f)
10 μm
(g)
1 mm
(h)
100 μm
(i)
0 μm

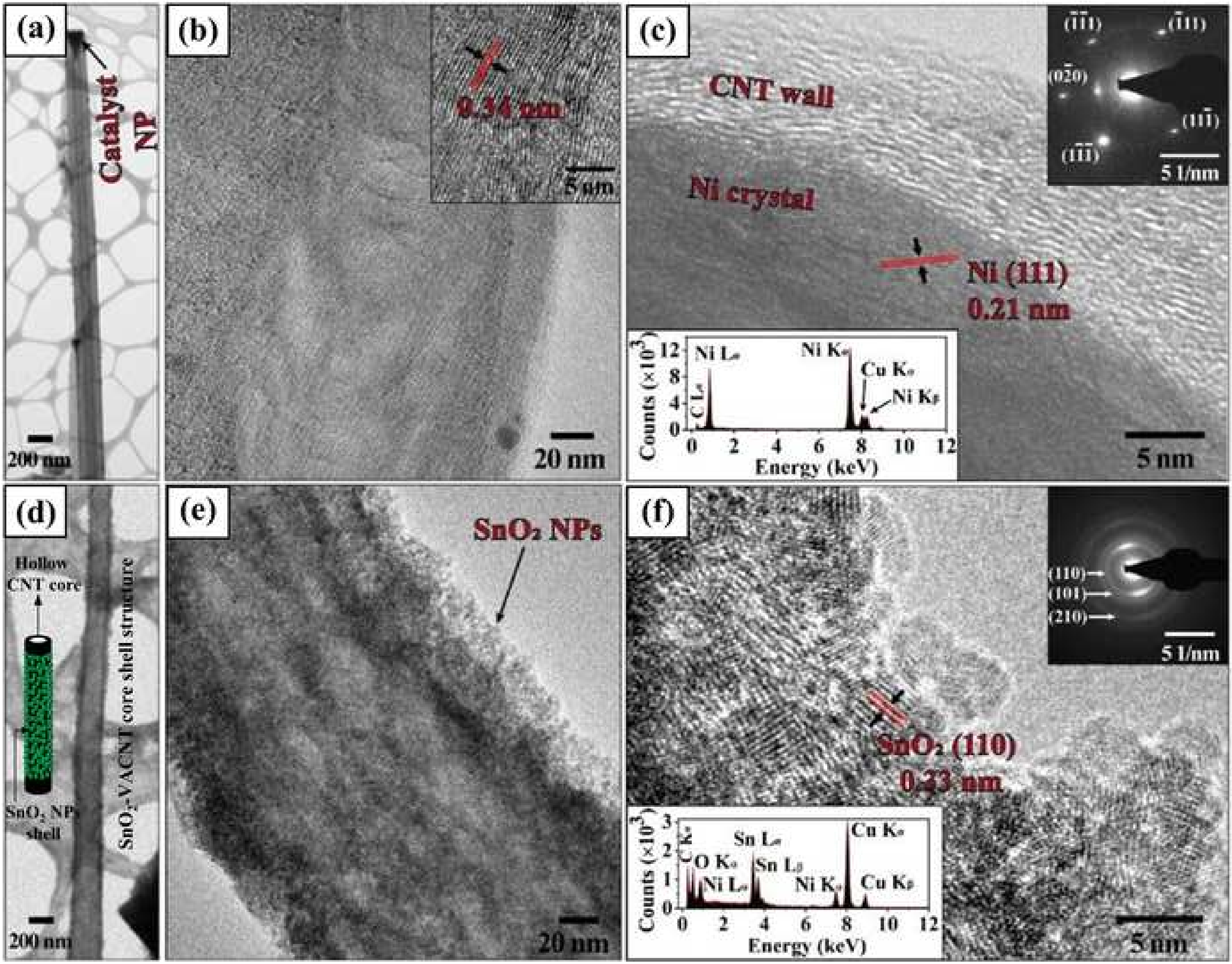
(a)
Catalyst NP
200 nm
(b)
0.34 nm
5 nm
20 nm
(c)
CNT wall
Ni crystal
Ni (111)
0.21 nm
(1̄1̄1)
(1̄11)
(02̄0)
(111̄)
(11̄1̄)
5 1/nm
Counts (×10³)
Ni Lα
Ni Kα
Cu Kα
Ni Kβ
C Kα
Energy (keV)
0 2 4 6 8 10 12
0 4 8 12
5 nm
(d)
Hollow CNT core
SnO₂ NPs shell
SnO₂-VACNT core shell structure
200 nm
(e)
SnO₂ NPs
20 nm
(f)
(110)
(101)
(210)
5 1/nm
SnO₂ (110)
0.33 nm
Counts (×10³)
C Kα
O Kα
Ni Lα
Sn Lα
Sn Lβ
Ni Kα
Cu Kα
Cu Kβ
Energy (keV)
0 2 4 6 8 10 12
0 1 2 3
5 nm

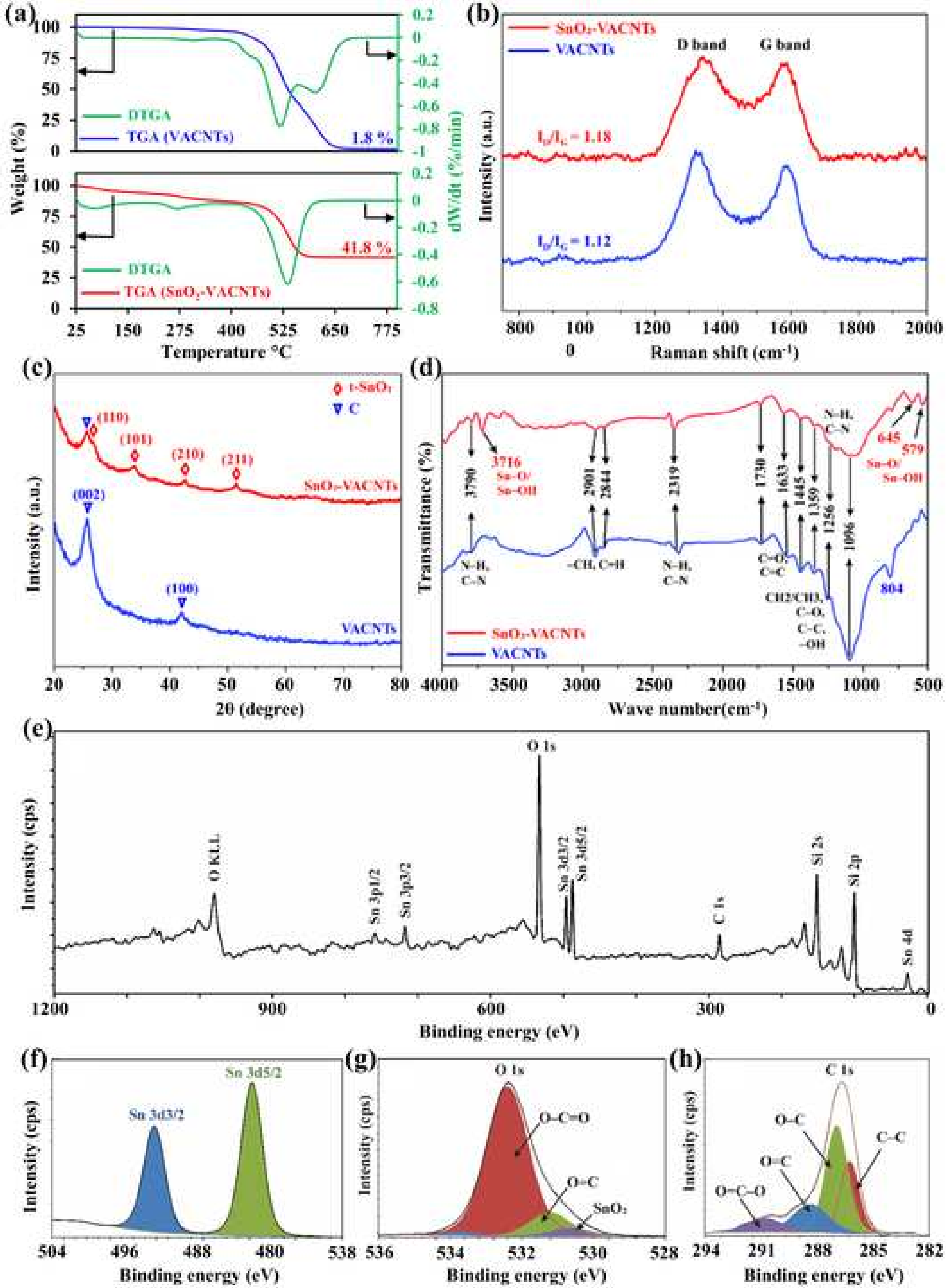
(a)
Weight (%)
dW/dt (%/min)
DTGA
TGA (VACNTs)
1.8 %
DTGA
TGA (SnO₂-VACNTs)
41.8 %
Temperature °C
25 150 275 400 525 650 775
(b)
SnO₂-VACNTs
VACNTs
D band
G band
I_D/I_G = 1.18
I_D/I_G = 1.12
Intensity (a.u.)
Raman shift (cm⁻¹)
800 1000 1200 1400 1600 1800 2000
(c)
t-SnO₂
C
(110)
(101)
(210)
(211)
(002)
(100)
SnO₂-VACNTs
VACNTs
Intensity (a.u.)
2θ (degree)
20 30 40 50 60 70 80
(d)
Transmittance (%)
3790
3716
Sn-O/
Sn-OH
2901
2844
2319
1730
1633
1445
1359
1256
1096
645
579
Sn-O/
Sn-OH
N-H,
C-N
N-H,
C-N
-CH, C=H
N-H,
C-N
C=O,
C=C
CH2/CH3,
C-O,
C-C,
-OH
804
SnO₂-VACNTs
VACNTs
Wave number(cm⁻¹)
4000 3500 3000 2500 2000 1500 1000 500
(e)
Intensity (cps)
O KLL
Sn 3p1/2
Sn 3p3/2
O 1s
Sn 3d3/2
Sn 3d5/2
C 1s
Si 2s
Si 2p
Sn 4d
Binding energy (eV)
1200 900 600 300 0
(f)
Intensity (cps)
Sn 3d3/2
Sn 3d5/2
Binding energy (eV)
504 496 488 480
(g)
Intensity (cps)
O 1s
O-C=O
O=C
SnO₂
Binding energy (eV)
538 536 534 532 530 528
(h)
Intensity (cps)
C 1s
O-C
C-C
O=C
O=C-O
Binding energy (eV)
294 291 288 285 282

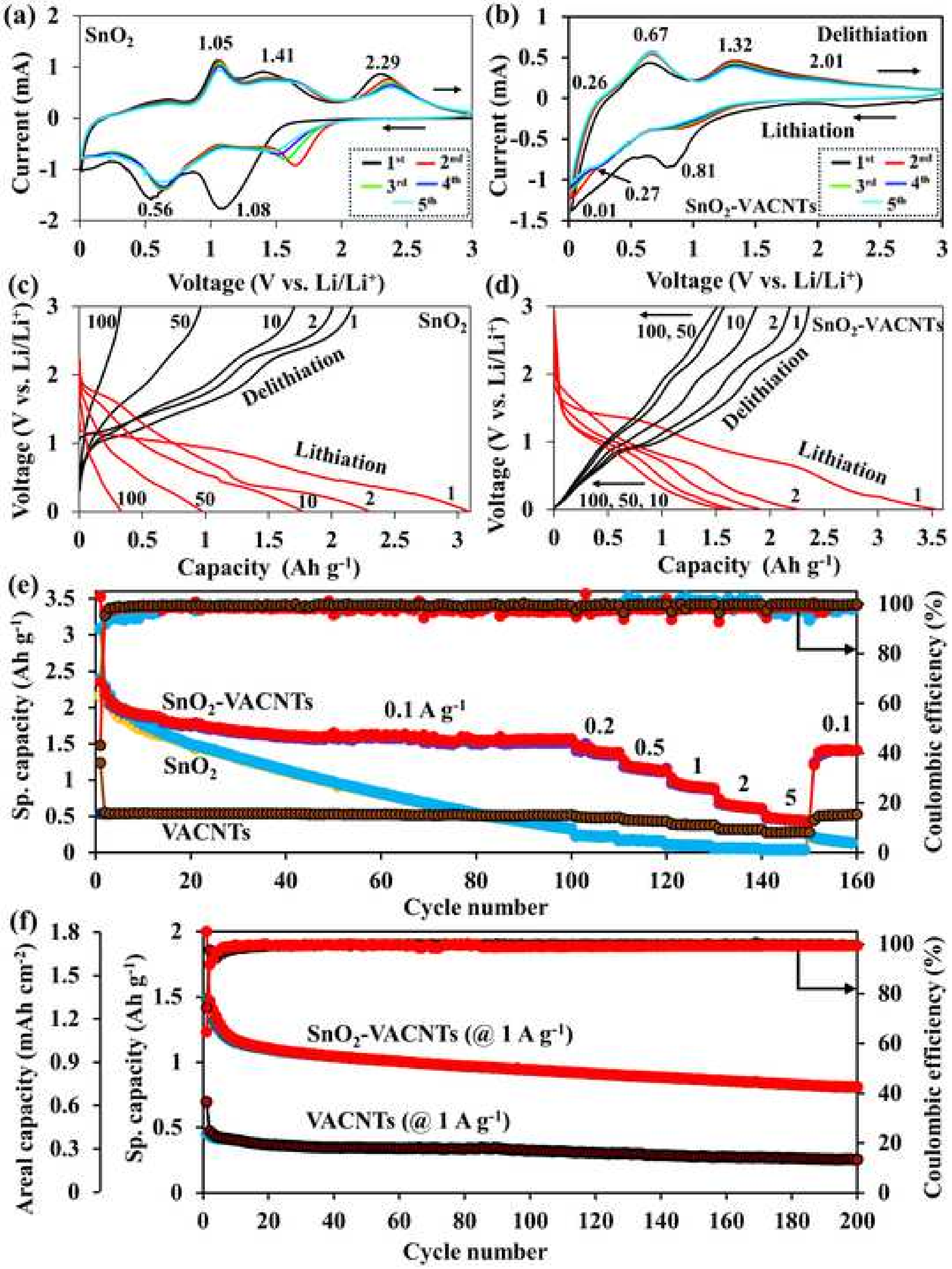
(a)
SnO2
1.05
1.41
2.29
0.56
1.08
1st 2nd 3rd 4th 5th
Current (mA)
Voltage (V vs. Li/Li+)
(b)
0.67
1.32
2.01
0.26
Delithiation
Lithiation
0.81
0.27
0.01
SnO2-VACNTs
1st 2nd 3rd 4th 5th
Current (mA)
Voltage (V vs. Li/Li+)
(c)
100 50 10 2 1
SnO2
Delithiation
Lithiation
100 50 10 2 1
Voltage (V vs. Li/Li+)
Capacity (Ah g-1)
(d)
100, 50 10 2 1
SnO2-VACNTs
Delithiation
Lithiation
100, 50, 10 2 1
Voltage (V vs. Li/Li+)
Capacity (Ah g-1)
(e)
SnO2-VACNTs
0.1 A g-1
0.2
0.5
1
2
5
0.1
SnO2
VACNTs
Sp. capacity (Ah g-1)
Coulombic efficiency (%)
Cycle number
(f)
SnO2-VACNTs (@ 1 A g-1)
VACNTs (@ 1 A g-1)
Areal capacity (mAh cm-2)
Sp. capacity (Ah g-1)
Coulombic efficiency (%)
Cycle number

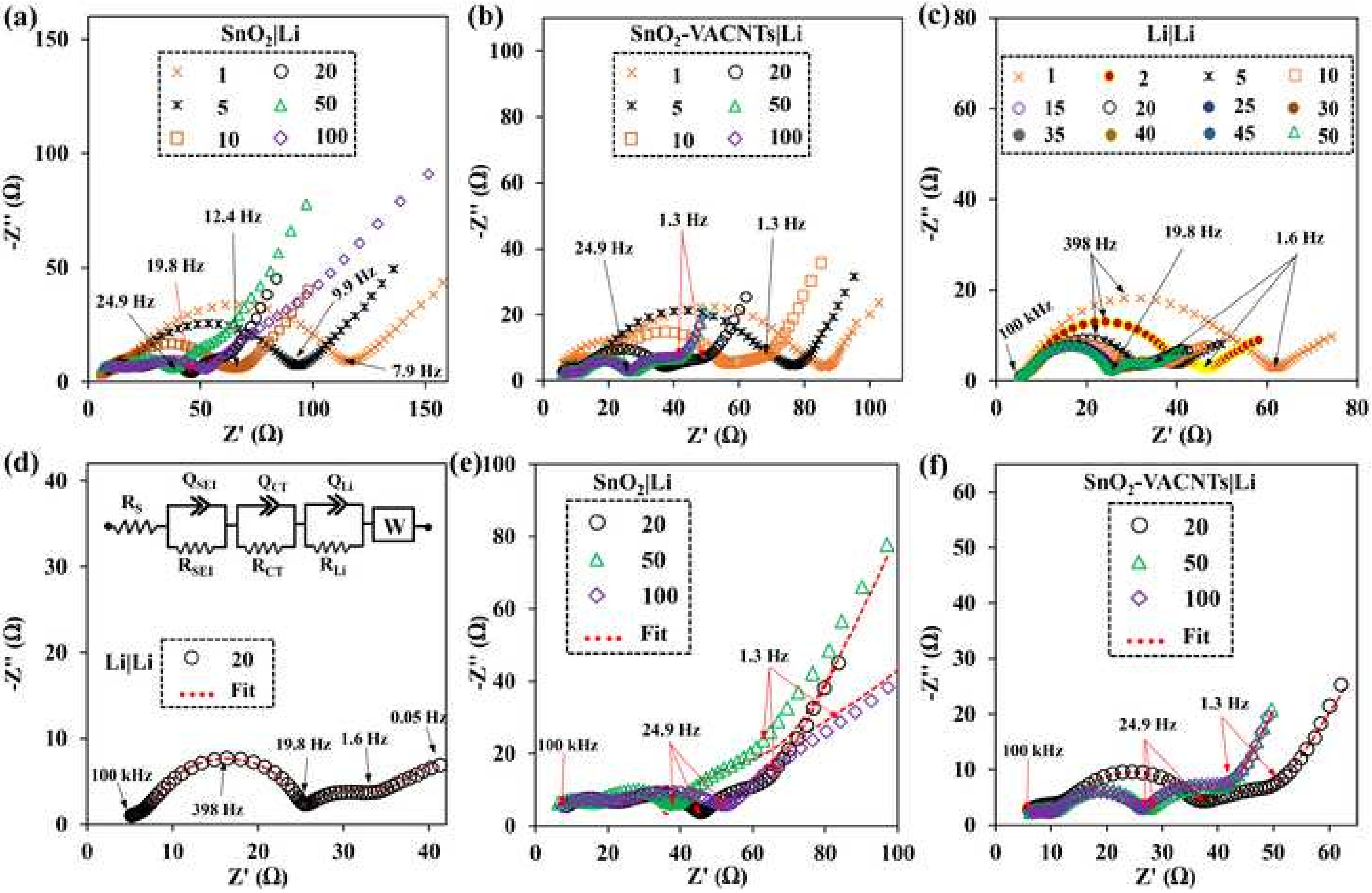
(a)
SnO$_2$|Li
1
5
10
20
50
100
12.4 Hz
19.8 Hz
24.9 Hz
9.9 Hz
7.9 Hz
-Z'' (Ω)
Z' (Ω)
(b)
SnO$_2$-VACNTs|Li
1
5
10
20
50
100
24.9 Hz
1.3 Hz
1.3 Hz
-Z'' (Ω)
Z' (Ω)
(c)
Li|Li
1
2
5
10
15
20
25
30
35
40
45
50
398 Hz
19.8 Hz
1.6 Hz
100 kHz
-Z'' (Ω)
Z' (Ω)
(d)
R$_S$
Q$_{SEI}$
Q$_{CT}$
Q$_{Li}$
R$_{SEI}$
R$_{CT}$
R$_{Li}$
W
Li|Li
20
Fit
100 kHz
398 Hz
19.8 Hz
1.6 Hz
0.05 Hz
-Z'' (Ω)
Z' (Ω)
(e)
SnO$_2$|Li
20
50
100
Fit
1.3 Hz
24.9 Hz
100 kHz
-Z'' (Ω)
Z' (Ω)
(f)
SnO$_2$-VACNTs|Li
20
50
100
Fit
1.3 Hz
24.9 Hz
100 kHz
-Z'' (Ω)
Z' (Ω)

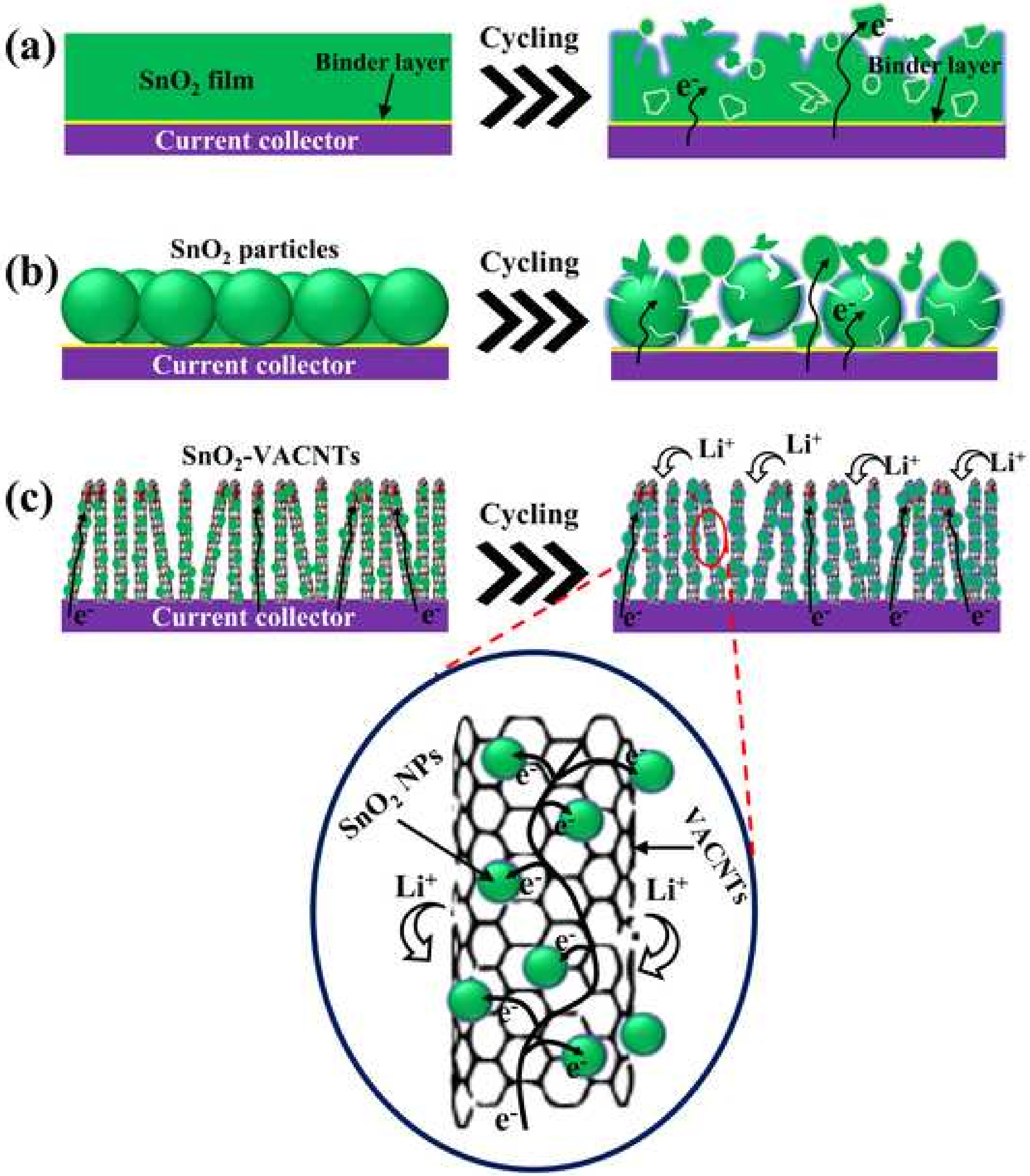
(a)
SnO$_2$ film
Binder layer
Current collector
Cycling
e$^-$
e$^-$
Binder layer
(b)
SnO$_2$ particles
Current collector
Cycling
e$^-$
(c)
SnO$_2$-VACNTs
Current collector
e$^-$
e$^-$
Cycling
Li$^+$
Li$^+$
Li$^+$
Li$^+$
e$^-$
e$^-$
e$^-$
e$^-$
SnO$_2$ NPs
VACNTs
Li$^+$
Li$^+$
e$^-$
e$^-$
e$^-$
e$^-$
e$^-$
e$^-$
e$^-$
e$^-$

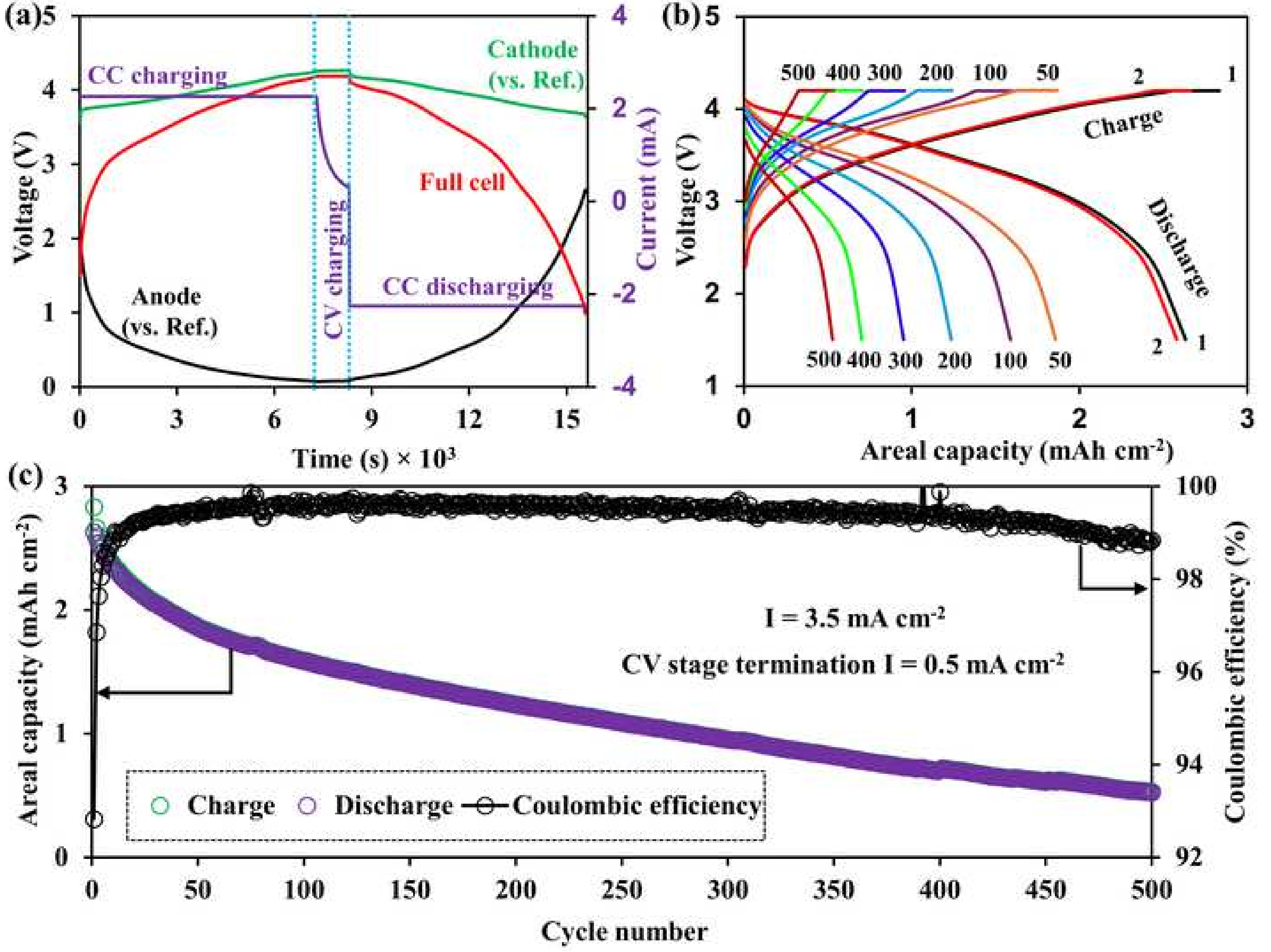
(a)
Voltage (V)
0
1
2
3
4
5
Current (mA)
-4
-2
0
2
4
Time (s) × 10^3
0
3
6
9
12
15
CC charging
Cathode
(vs. Ref.)
Full cell
CV charging
CC discharging
Anode
(vs. Ref.)
(b)
Voltage (V)
1
2
3
4
5
Areal capacity (mAh cm^{-2})
0
1
2
3
500
400
300
200
100
50
2
1
Charge
Discharge
500
400
300
200
100
50
2
1
(c)
Areal capacity (mAh cm^{-2})
0
1
2
3
Coulombic efficiency (%)
92
94
96
98
100
Cycle number
0
50
100
150
200
250
300
350
400
450
500
I = 3.5 mA cm^{-2}
CV stage termination I = 0.5 mA cm^{-2}
Charge
Discharge
Coulombic efficiency

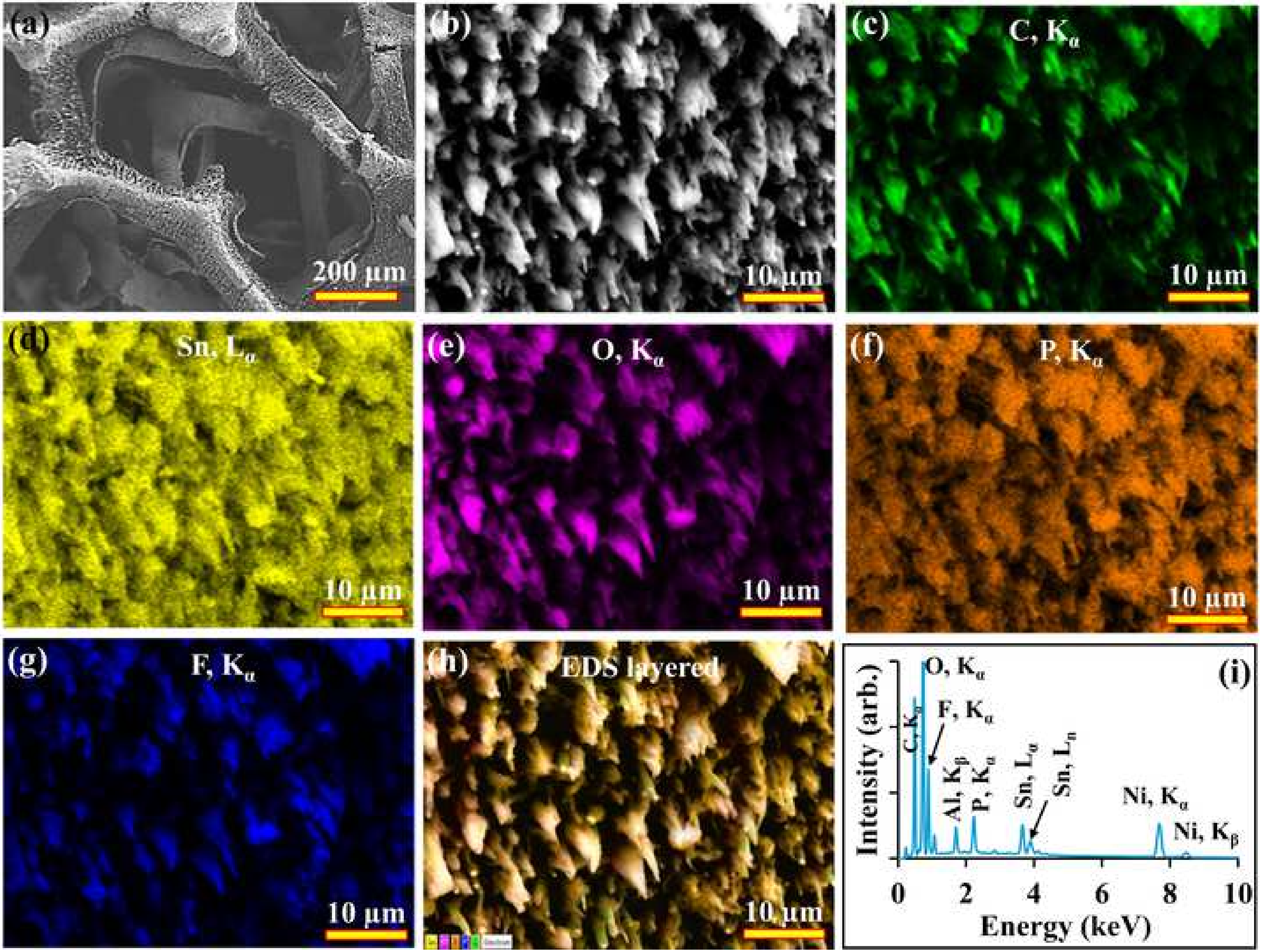
(a)
200 μm
(b)
10 μm
(c)
C, K_{α}
10 μm
(d)
Sn, L_{α}
10 μm
(e)
O, K_{α}
10 μm
(f)
P, K_{α}
10 μm
(g)
F, K_{α}
10 μm
(h)
EDS layered
10 μm
(i)
O, K_{α}
C, K_{α}
F, K_{α}
Al, K_{β}
P, K_{α}
Sn, L_{α}
Sn, L_{η}
Ni, K_{α}
Ni, K_{β}
Intensity (arb.)
Energy (keV)
0
2
4
6
8
10

Click here to access/download

Video

HR_TEM_SnO2-CNT_Li.mp4

Highlights

- We developed a binder and conductive additive-free anode for lithium-ion batteries.
- The anode is a core-shell VACNTs-SnO_2 array directly coupled to a current collector.
- The anode exhibited a high sp. capacity of ~1.5Ah g^{-1} at a rate of 0.1 A g^{-1}.
- A high rate cyclability was tested for 200 cycles at a rate of 1 A g^{-1}.
- The reason for excellent performance was the special morphology of the anode.

Declaration of interests

☐The authors declare that they have no known competing financial interests or personal relationships that could have appeared to influence the work reported in this paper.

☒The authors declare the following financial interests/personal relationships which may be considered as potential competing interests:

Wenzhi Li (Corresponding author) and Arun Thapa (Co-author) has patent Coated Vertically Aligned Carbon Nanotubes On Nickel Foam issued to Florida International University. If there are other authors, they declare that they have no known competing financial interests or personal relationships that could have appeared to influence the work reported in this paper.

Binder-free Tin (IV) Oxide Coated Vertically Aligned Carbon Nanotubes as Anode for Lithium-ion Batteries

Arun Thapa [a, c], Amin Rabiei Baboukani [b], Prahald Siwakoti [d], Katherine L. Jungjohann [e], Chinaza E. Nwanno [a], Jiandi Zhang [d], Chunlei Wang [b], Hongwei Gao [c], Wenzhi Li [a,*]

[a] *Department of Physics, Florida International University, Miami, FL 33199, USA*

[b] *Department of Mechanical and Materials Engineering, Florida International University, Miami, FL, 33174, USA*

[c] *Department of Electrical & Computer Engineering, Montana State University, Bozeman, MT 59717, United States*

[d] *Department of Physics & Astronomy, Louisiana State University, Baton Rouge, LA 70803, USA*

[e] *Center for Integrated Nanotechnologies, Sandia National Laboratories, Albuquerque, NM 87185, United States*

Abstract

Despite the tremendous potential of tin oxide (SnO_2) as an anode material, irreversible capacity loss due to the sluggish kinetics and structural pulverization as a result of the substantial volume alteration during redox reactions limits its use in lithium-ion batteries. The typical layered design of an electrode consisting of binder and conductive additive can lower the practical capacity of high-capacity electrode materials. We synthesized a binder and conductive additive-free, self-standing core-shell vertically-aligned carbon nanotubes (VACNTs)-SnO_2 anode (SnO_2-VACNTs) on 3D nickel foam using plasma-enhanced chemical vapor deposition and wet chemical method. The SnO_2-VACNTs exhibited excellent cyclability with a specific capacity of 1512 mAh g^{-1} at 0.1 A g^{-1} after 100 cycles and 800 mAh g^{-1} at 1 A g^{-1} after 200 cycles. The ultra-fine SnO_2 particles (< 5 nm) shortened the Li^+ diffusion paths into the bulk electrode and alleviated the volume alteration by lowering the strains during the redox reactions. Also, proper inter-tube distance between individual SnO_2-VACNTs buffered the volume instability and offered better electrolyte accessibility. Direct connection of VACNTs with the current collector ensured an uninterrupted electron conducting path between the current collector and active material, thus offering more efficient charge transportation kinetics at the electrode/electrolyte interfaces.

Keywords:

Lithium-ion batteries (LIBs); Vertically aligned CNTs; SnO_2 nanoparticles; Binder-free anode; Electrochemical Impedance Spectroscopy (EIS).

***Corresponding author:** Tel: +1 (305)348-7257**, E-mail:** Wenzhi.Li@fiu.edu (Wenzhi Li)

1. Introduction

The importance of lithium-ion batteries (LIBs) has increased ever since the commercialization of LIB comprised of lithium cobalt oxide ($LiCoO_2$) cathode paired with hard-carbon (C) anode by Sony Inc. in 1991 [1] due to their high energy and power density, broader operating temperature range, low self-discharge rate, and an absence of memory effect [2, 3]. Nonetheless, the ever-increasing use of LIBs in household appliances to sophisticated modern devices, including but not limited to electric vehicles (EVs), demands novel LIB electrodes with improved electrochemical properties and performances suitable for delivering high energy and power densities with negligible safety issues. Most commercial LIBs comprise graphite as an active anode material, which has a theoretical capacity of 372 mAh g^{-1} [4, 5]. However, the state-of-the-art LIBs have already attained the maximum specific capacity of graphite anodes and hence do not offer any significant improvement in energy density. Therefore, an alternate anode to the graphite is essential for high-performing LIBs.

Metal oxides such as tin oxide (SnO_2) [6], iron oxide (Fe_2O_3) [7], cobalt oxide (Co_3O_4) [8], copper oxide (CuO) [9], iron titanium oxide (Fe_2TiO_5) [10], and heterostructured nickel-iron oxide ($NiFe_2O_4/Fe_{0.64}Ni_{0.36}$) [11] are regarded as promising candidates to substitute the commercial graphite anode because of their high theoretical capacity. Among them, SnO_2 has attracted much attention recently due to its impressive theoretical specific capacity of 1493 mAh g^{-1} [12], cost-effectiveness, and good environmental compatibility. The Li^+ storage mechanism of SnO_2 comprises two stages. First, upon initial charge (conversion reaction), SnO_2 transforms to Sn and Li_2O according to the following reaction [13].

$$SnO_2 + 4Li^+ + 4e^- \rightarrow Sn + 2Li_2O \qquad (1)$$

Subsequent lithiation of the SnO_2 (alloying reaction) corresponds to the following reversible phase transformation reactions [13].

$$Sn + xLi^+ + xe^- \leftrightarrow Li_xSn \qquad (0 \leq x \leq 4.4) \qquad (2)$$

The first reaction (**Eq. 1**) is considered to be electrochemically irreversible. Hence, the maximum capacity of the SnO_2 is challenging to achieve. Some reports [14-16] suggested that the conversion reaction can become partially reversible if the SnO_2 size is reduced to less than 10 nm, while others [17, 18] reported that the SnO_2 nanoparticles are electrochemically irreversible. These findings indicate that the nano size of the SnO_2 particles is not solely responsible for the reversibility and cannot ensure a maximum reversible capacity. It is important to recognize other key factors closely linked to the electrochemical reactions that can facilitate optimum Li^+ storage; for example, creating an uninterrupted electron conducting path between the current collector and the active material can be a key to achieving high capacity, excellent rate capability, and cycling life. An easy access to electrolyte for the active material during lithiation/delithiation is another important factor affecting the Li^+ storage capacity of the active material. It is reported that nanoporous carbon matrix used as additives in metal oxide electrodes played important roles in rate capability and cycling life because of its high conductivity and its ability to facilitate easy electrolyte distribution due to the nanoporous structure [19, 20].

Carbon nanotubes (CNTs) are regarded as remarkable additive materials due to their excellent electrical and thermal conductivity for improving energy conversion, storage capacities, and charge transferability of active materials [21]. Furthermore, CNTs, including carbon nanofibers, have also been credited as excellent anode materials due to their one-dimensional tubular morphology, large surface area, short Li^+ diffusion path, and high electrical and thermal conductivity [22-25]. Moreover, due to their tubule structure and high flexibility, CNTs can be excellent hosts for high-capacity active materials. For instance, nanoparticles, including SnO_2, can be coated on the CNT's outer wall, creating a core (CNTs)-shell (layer of SnO_2) structure (SnO_2-CNTs) [26, 27]. Due to this unique structure, SnO_2-CNTs core-shell can absorb considerable stress resulting from active material pulverization during the lithiation/delithiation procedure. Several reports have shown excellent Li^+ storage properties of SnO_2-CNTs composite nanomaterial as the anode of LIBs [28-30]. However, the conventional bilayer design of the electrode, where a binder is used to glue active materials to a current collector, limits achieving the maximum capacity of SnO_2 electrodes. Reports have shown that the layered design of the LIB anode can reduce the practical capacity by ~47% [31]. Therefore, besides limiting the SnO_2 size below the critical threshold (<10 nm) and understanding the subsequent structural evolution during the electrochemical reaction, the electrode material's uninterrupted electron conducting path and high electrolyte accessibility are essential in achieving the maximum reversible capacity of SnO_2 and hence for the future commercialization of SnO_2-based anodes.

It is reported that tin (Sn), germanium (Ge), and silicon (Si) coated on free-standing vertically-aligned carbon nanotubes (VACNTs) can significantly improve the Li^+ storage by offering effective strain accommodation and electrolyte access due to the regular pore morphology and inter-tube space of the VACNTs array [32-35]. It is important to note that the VACNTs arrays in these reports were synthesized using catalyst-buffer bilayers on top of the current collector surface, and hence, the VACNT arrays cannot be classified as directly grown on the current collector. In addition, the bilayer materials add extra impurities to the active materials, which may complicate the electrochemical redox reaction by causing parasitic reactions. We proposed that a direct synthesis of VACNTs on current collectors (such as a Ni foam) and the high conductivities of VACNTs will reduce the electrical contact resistance between VACNTs and current collectors, which will enhance the charge transfer and facilitate effective heat dissipation caused by resistive heating. Furthermore, an array of VACNTs with a finite space between individual tubes can alleviate the stress resulting from volume alteration during the lithiation/delithiation reactions. Therefore, an electrode designed by growing VACNTs directly on the current collector and then coating the VACNTs with a layer of ultra-fine high-capacity electrode material such as SnO_2 nanoparticles without any binder could be an excellent LIB anode material with high energy capacity.

In this work, free-standing VACNT arrays have been grown directly on 3D nickel foam using a plasma-enhanced chemical vapor deposition method. The as-synthesized VACNTs have been coated with a layer of SnO_2 nanoparticles (SnO_2-VACNTs) to form core-shell structured hybrid material free of any binder. Then, the material was tested for its electrochemical lithiation property as the anode in coin-type lithium-ion half cells. The electrochemical Li^+ storage performance of the SnO_2-VACNTs anode has been measured, and assessed by comparing it with the SnO_2-coated Ni foam and pristine VACNTs synthesized on Ni foam. Furthermore, the excellent electrochemical Li^+ storage performance of the SnO_2-VACNTs anode has been explained in detail using electrode impedance evolution with the electrode cycle age. Moreover, the correlation between the microstructure and the electrochemical properties of the anode material has also been explained thoroughly.

2. Experimental

2.1 Electrodes preparation

Vertically aligned carbon nanotubes (VACNTs) were synthesized on nickel foam (Ni, 99.99% by wt., Alfa Aesar) using plasma-enhanced chemical vapor deposition (PECVD). The apparatus and synthesis procedure details are described in our previous work [36]. In brief, circular disks of a diameter of about 10 mm were punched out from as-received Ni foam (1.6 mm thick) and immersed sequentially in ultrasonic baths of isopropyl alcohol and acetone, each for 10 minutes. The cleaned Ni foam disks were placed into the PECVD system and then pumped down to the pressure of 0.01 Torr. The VACNT synthesis procedure was performed at 600 ºC for 6 minutes using C_2H_2 (25 sccm) as carbon precursor gas diluted with NH_3 (400 sccm). Also, the synthesis procedure was carried out at the pressure of 7 Torr and in the presence of a d.c. plasma of power 70 W to ensure the alignment of CNTs. Tin oxide (SnO_2) coated VACNTs (SnO_2-VACNTs) composite electrodes were fabricated using a wet-chemical method [26]. First, the VACNTs on Ni foam were functionalized using HNO_3 (20%) for 15 minutes. Before the final coating procedure, a precursor solution was formulated by dissolving 1 g of anhydrous tin (II) chloride ($SnCl_2$, 98%, Alfa Aesar) in 80 mL DI water and 1.4 mL HCl (38%). Then, the functionalized VACNTs were coated with SnO_2 nanoparticles by submerging them into the precursor solution for 9 hours. The weight of the SnO_2-VACNTs anodes (active material for Li^+ storage) was in the range of 1.02 – 1.21 mg cm^{-2}. This weight refers to the weight of VACNTs synthesized for 6 minutes and the weight of SnO_2 coated for 9 hours. However, in order to increase the areal capacity of the SnO_2-VACNTs anode for use in full cell performance test, the

VACNT growth time and SnO_2 coating time were increased to 20 minutes and 18 hours, respectively, which resulted in the SnO_2-VACNTs weight of ~1.7 mg cm^{-2}. For comparison purposes, bare Ni foams were coated with SnO_2 using a similar procedure, but the Ni foams were treated with Ozone for 30 minutes to remove any contaminants before being immersed in the precursor solution for SnO_2 coating. Finally, the SnO_2-coated electrodes were removed from the precursor solution and dried out overnight at 95 °C. The weight of the active material (SnO_2) coated on the Ni foam was ~1 mg cm^{-2} from a 9-hour coating process.

Furthermore, the cathode was fabricated by using commercial $LiNi_{0.8}Mn_{0.1}Co_{0.1}O_2$ (Lithium Nickel Manganese Cobalt Oxide, NMC811) microparticles. First, an N-methylpyrrolidone (NMP, anhydrous, 99.5%, Sigma-Aldrich)-based slurry composed of 90 wt% NMC (MTI Corp.), 2.5 wt% carbon nanotubes (ACS Materials), 2.5 wt% Super P conductive carbon (MTI Corp.), and 5 wt% polyvinylidene fluoride (PVDF) binder (MTI Corp.) was prepared by mixing at 320 rpm for 30 minutes using a vacuum mixture. Then, the resulting slurry was coated onto carbon-coated (thickness 1 μm) aluminum foil (thickness 15 μm) using a doctor blade calibrated to provide active material loading of ~15 mg cm^{-2}, an equivalent nominal areal capacity of ~3 mAh cm^{-2}. The electrode foil was dried at room temperature for 2 hours and 110 °C for 12 hours in a vacuum oven. The cathode was calendered at 90 °C to a target thickness of ~60 μm using a heated calendering machine.

2.2 Materials characterization

The surface morphology of VACNT arrays, SnO_2 layer coated on Ni foam (the sample will be termed as SnO_2 hereafter), and SnO_2-VACNTs were characterized using a field emission scanning electron microscope (SEM, JEOL JSM–6330F). The surface morphology of the Ni foam was analyzed using atomic force microscopy (AFM). The nanostructure, chemical composition, and crystal structure analysis of VACNTs and SnO_2-VACNTs were performed using a transmission electron microscope (TEM) operated at an accelerating voltage of 300 kV. Thermogravimetric analysis (TGA) of the materials was accomplished using the thermogravimetric-differential scanning calorimetry analysis (TG/DSC, SDT Q600 V20.9, USA). All experiments were performed under airflow and a temperature increase of 10 °C/min. In order to prepare the sample for the TGA experiments, the as-synthesized SnO_2-VACNTs were detached from the Ni foam using an IPA ultrasonic bath for 10 minutes. The possible Ni remanent in the SnO_2-VACNTs/IPA solution was carefully removed by using a strong bar magnet, and the SnO_2-VACNTs were filtered out from the resulting solution. Then, the SnO_2-VACNTs were dried overnight at 100 °C before the TGA experiment. Crystal structure and defect analysis of the as-synthesized materials were performed using X-ray diffraction (Siemens Diffraktometer D5000, Cu (Kα), $\lambda = 1.54$ Å, 0.02° step size, 20° to 80° range, 2°/min speed) and Raman spectroscopy (Ar^+, $\lambda = 632.8$ nm). A Fourier transform infrared spectrometer (Jasco, FTIR-4100) was used to analyze functional groups on the VACNTs and SnO_2-VACNTs. The chemical state of each element in the electrode was analyzed using X-ray photoelectron spectroscopy. The core level spectra were measured using a monochromated Al (Kα) X-ray source and a PHOIBOS 150 energy analyzer, both from SPECS.

2.3 Lithium-ion cell assembly and electrochemical measurements

Electrochemical properties of the as-synthesized materials were studied using CR2032 coin-type half cells with a lithium foil (3860 mAh g^{-1}) as the counter and reference electrode. Lithium hexafluorophosphate solution (1M $LiPF_6$) in ethylene carbonate and diethyl carbonate (EC:DEC, 1:1, vol. %) was used as an electrolyte, and Celgard polypropylene films were used as electrode separators. A symmetric test cell with identical working and counter electrodes of lithium foil (10 mm diameter) was used to evaluate and isolate the interfacial electrochemical properties of the working electrode from the counter/reference electrodes. In addition, a coin-type full cell was fabricated in an anode overhang configuration with a slightly bigger anode area (diameter 13 mm) compared to that of the cathode (diameter 12 mm) and electrodes overlapped area was used while calculating the areal capacity of the cell. However, the anode and cathode were of the same diameter (12 mm) in the case of the three-electrode cell. The specific capacities of the half cells were calculated based on the weight of active materials. For further clarification, the specific capacities of the SnO_2-VACNTs half cells were calculated based on the combined weight of VACNTs and SnO_2. The electrochemical properties were measured at room temperature (~23 °C) using a NEWARE battery tester, Gamry reference 3000 potentiostat, and Arbin battery cycler.

3. Results and discussion

3.1 Structural and compositional properties

3.1.1 AFM analysis

Vertically aligned carbon nanotube (VACNT) arrays were grown directly on catalytic 3D Ni foam without any external catalysts. The use of catalytic metal substrates such as Ni foam for synthesizing VACNTs facilitates the evolution of the catalytically active growth spots (nano-hills) on the substrate surface, which further initiates on-site disintegration of hydrocarbon precursor gas and the diffusion of carbon atoms into the catalytic sites, i.e., nano-hills [36]. Carbon atoms precipitate on the nano-sized catalyst surface upon supersaturation and lead to the formation of CNTs after graphitization [37]. To understand the growth of VACNTs on the catalytic substrate, the surface evolution of the Ni foam due to the heat treatment, under similar conditions used for VACNTs growth except carbon precursor gas, was analyzed using SEM and

AFM images (see **Figs. S1(a-c)**). Three-dimensional AFM images (**Fig. S1(b)**) revealed a relatively smooth surface of the pristine Ni foam with a mean roughness R_a = 53.68 nm, whereas the AFM image (**Fig. S1(c)**) after the heat treatment revealed a much rougher surface with R_a = 105 nm. This result confirmed that uniform catalyst sites (nano-hills) formed on the Ni foam surface due to the application of heat in the presence of reducing gas (NH_3) catalyzed the nucleation and growth of VACNT arrays.

3.1.2 SEM analysis

Figs. 1(a-c) show low to high magnification SEM images of Ni foam coated with SnO_2. The SEM images revealed the rough surface of Ni foam due to the non-uniform coating with macroscopic SnO_2 particles. As shown in the inset of **Fig. 1(c)**, the energy-dispersive X-ray

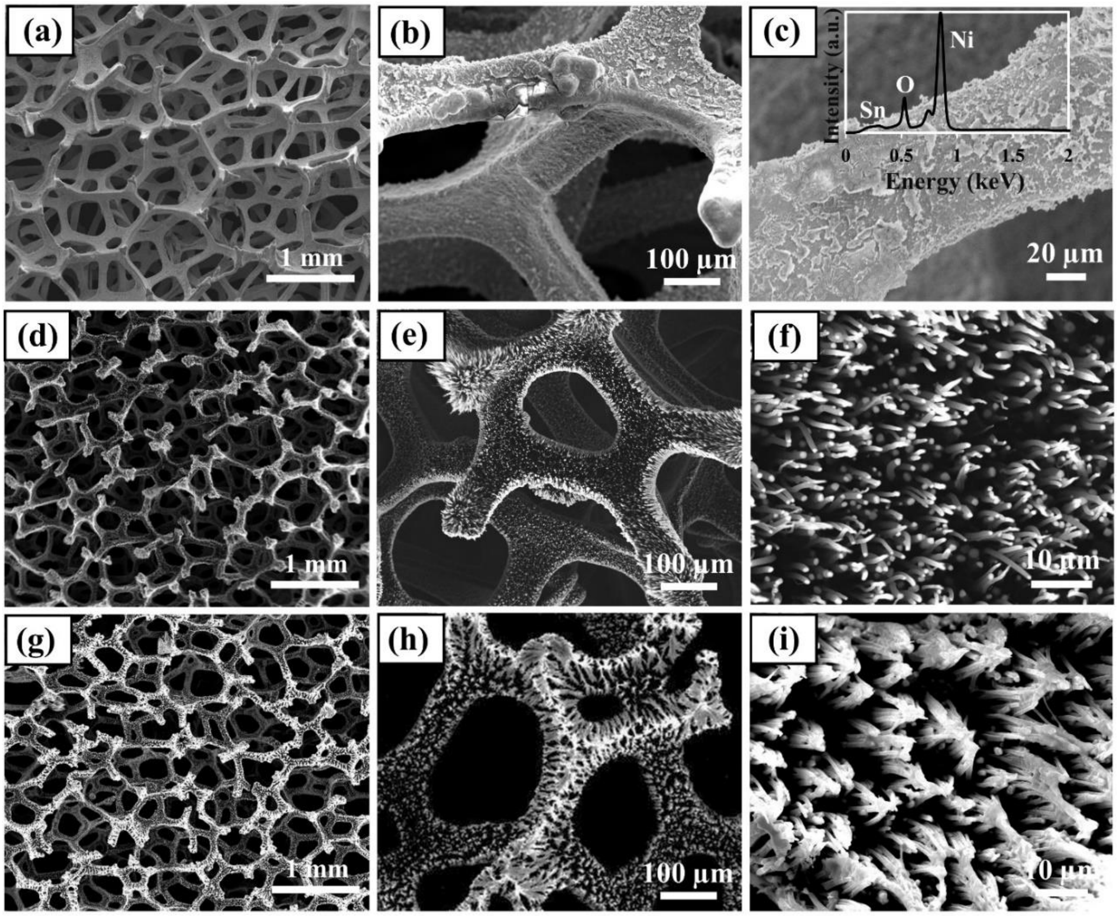

Fig. 1. SEM images of SnO_2 and SnO_2-VACNTs on Ni foam at low to high magnification. (a-c) SnO_2 coated on Ni foam, (d-f) VACNTs grown on Ni foam, and (g-i) SnO_2 coated on VACNTs. The inset in panel **(c)** represents the EDS spectrum measured on the surface of SnO_2 coated on Ni foam.

spectroscopy (EDS) measured on the surface of Ni foam confirmed that the particles on the surface are SnO_2. The Ni signal in the spectrum is from the Ni foam substrate. The ozone treatment of the Ni foam may have assisted in creating some functional groups on the surface, which could facilitate the coating of SnO_2 on the Ni foam. **Figs. 1(d-f)** show low to high magnification SEM images of vertically aligned and uniform arrays of CNTs grown on the Ni foam. The diameter of VACNTs was in the range of 150-270 nm, whereas the length was ~5 µm long. **Figs. 1(g-i)** display low to high magnification SEM images of uniquely bundled SnO_2-VACNT arrays in which the VACNT tips touch each other. These bundles were formed by the solution phase SnO_2 coating process.

3.1.3 TEM analysis

TEM image, as shown in **Figs. 2(a, b)**, revealed a "bamboo-like" morphology of as-synthesized VACNTs with a catalyst nanoparticle anchored at the top end of the tubular structure [37]. As shown in the inset of **Fig. 2(b),** the lattice fringes in the CNT wall are separated by 0.34 nm in the VACNT wall, suggesting the multi-walled structure of CNTs. The high-resolution TEM image of the tip of VACNT, as shown in **Fig. 2(c)**, revealed crystal lattice planes separated by 0.21 nm, which corresponds to the (111) lattice plane of face-centered cubic Ni crystal, as expected. This result indicates that the VACNTs were grown directly from the Ni foam. The direct connection between the VACNTs and Ni foam is expected to benefit the electron transfer between them. When poor electrical conducting material, such as SnO_2, is coated on the VACNTs' surface, the VACNTs will also improve the electron transfer between the SnO_2 and Ni substrate. The distinct diffraction spots of the particle entrapped at the VACNT apex (upper-right inset of **Fig. 2(c)**) can be assigned to (0$\bar{2}$0), ($\bar{1}\bar{1}$1), and ($\bar{1}$11) planes of face-centered cubic Ni crystal along the [101] zonal axis, which confirmed that the nanoparticle encapsulated inside the CNT is a single crystalline Ni particle. The EDS spectrum displayed in the inset of **Fig. 2(c)** further corroborated the particle at the CNT tip as a Ni metal. Furthermore, the peaks related to C and Cu in the spectrum occurred due to the VACNT wall and TEM holder, respectively.

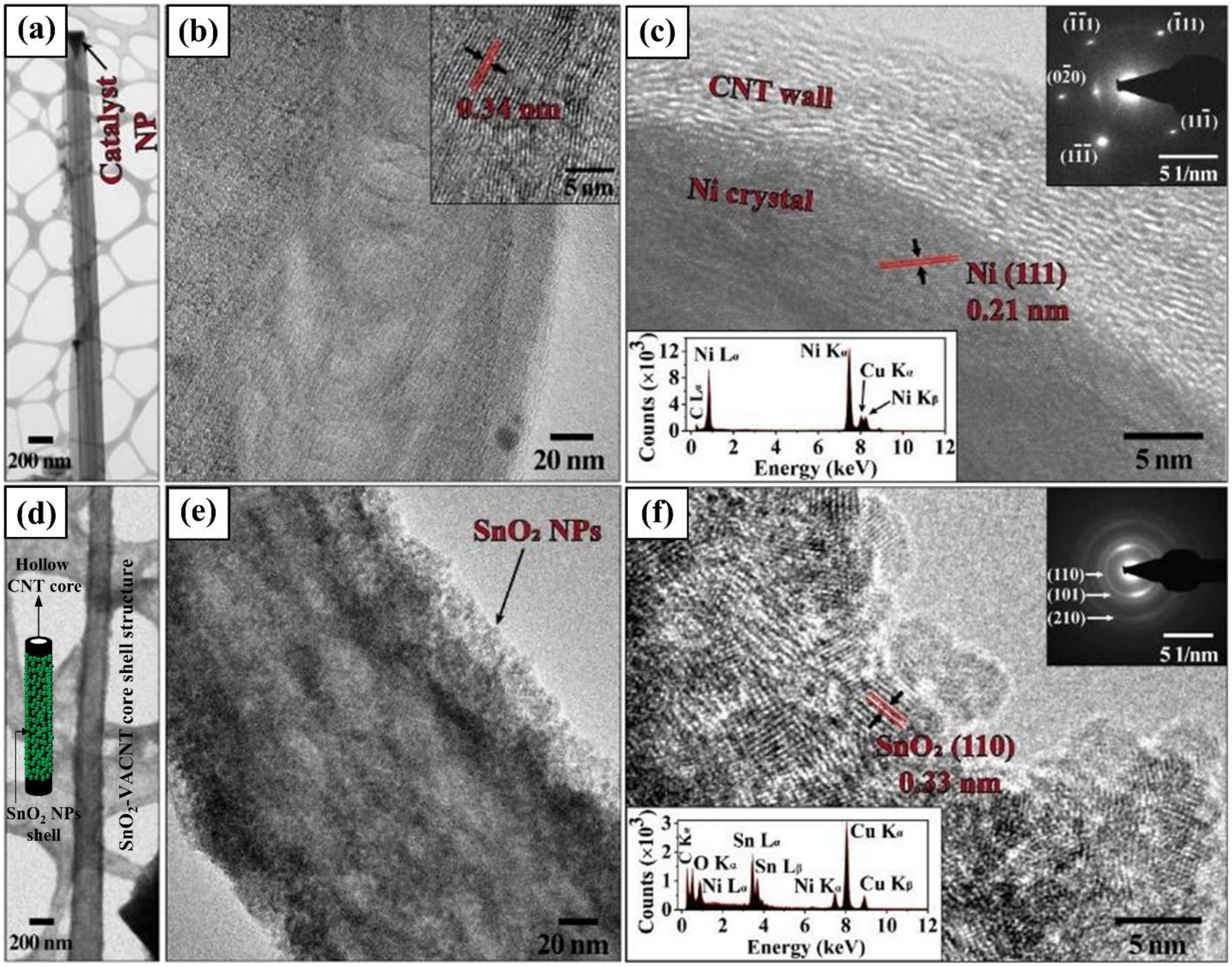

Fig. 2. TEM characterization of the as-synthesized VACNT (a-c) and SnO_2-VACNT (d-f) samples. (a) and (b) are low and high magnification images of a VACNT. The inset in panel (b) represents a high-resolution TEM image of the VACNT wall. (c) High-resolution TEM image showing an interfacial region between the VACNT wall and the catalyst particle. The upper-right and lower-left insets in panel (c)

represent the SAD and EDS of the Ni anchored at the VACNT apex. (d, e) Low and high magnification TEM images of a SnO_2-VACNT showing that the VACNT was coated with a layer of SnO_2-nanoparticles. The inset in panel (d) represents a schematic showing the core-shell structure of the SnO_2-VACNT. (f) High-resolution TEM image of the SnO_2 nanoparticles of a SnO_2-VACNT. The upper-right and lower-left insets in panel (f) are the SAD and EDS of the SnO_2 nanoparticles.

TEM images, as shown in **Figs. 2(d, e),** show a core-shell structure formed with the core of VACNT and a shell of a thin layer (~20 nm) of SnO_2 nanoparticles. For clarity, a schematic showing the core-shell structure of the SnO_2-VACNT is presented in the inset of **Fig. 2(d)**. The TEM images (**Figs. 2(e, f)**) clearly show that the coating consists of a multilayer of SnO_2 nanoparticles. A single layer of SnO_2 nanoparticles coating can be considered ideal regarding an efficient reversible electrochemical lithiation/delithiation of the SnO_2 nanoparticles. However, it is desirable to increase the content of the SnO_2 nanoparticles for practical applications, such as for high-energy-density LIBs. This means that there should be a fine balance between the coating thickness and the content of the SnO_2 nanoparticles for optimum performance of the SnO_2-VACNTs electrode. Although it is out of the scope of this work, it is imperative to determine the optimal content of the SnO_2 nanoparticles in the SnO_2-VACNTs electrode for future practical applications. The high-resolution TEM image in **Fig. 2(f)** confirmed the crystalline phase of SnO_2 nanoparticles with distinct crystal planes isolated by 0.33 nm, which can be assigned to the (110) lattice plane of the tetragonal SnO_2 (t-SnO_2) crystal. Furthermore, the EDS of the SnO_2-VACNT, the upper-right inset of **Fig. 2(f),** shows circular diffraction rings which can be indexed as (110), (101), and (210) lattice planes associated with the polycrystalline t-SnO_2. The occurrence of EDS peaks related to Sn, O, and C (lower-left inset of **Fig. 2(f)**) further confirmed the specimen as the SnO_2-VACNT core-shell. Moreover, the EDS peaks related to Ni and Cu can be assigned to the catalyst particle (Ni from Ni foam) anchored at the VACNT tip and TEM grid, respectively.

3.1.4 TGA analysis

In order to determine the weight percentage of SnO_2 nanoparticles on the SnO_2-VACNTs composite electrode, TGA analysis was performed, and the results are presented in **Fig. 3(a)**. The TGA profiles of VACNTs and SnO_2-VACNTs demonstrated weight loss as a result of moisture elimination up to 400 °C. However, SnO_2-VACNTs exhibited more significant weight loss, attributed to the solution-based SnO_2 coating process. The VACNTs demonstrated a slight weight reduction at ~435 °C due to the oxidation of amorphous carbon formed on the VACNTs during the synthesis process. Most of the weight loss of the VACNTs occurred in the temperature range of 520 °C – 605 °C. On the other hand, the SnO_2-VACNTs material showed a significant weight reduction at ~537 °C corresponding to the loss of the VACNTs. This result suggests that pristine VACNTs were more stable than the VACNTs in the SnO_2-VACNTs because the VACNTs in the SnO_2-VACNTs have more defects suffered from the SnO_2-coating process [38]. It has been verified that SnO_2 (~10 nm) nanopowder can show thermal stability up to 900 °C [39]. Therefore, the final residual after 800 °C of both samples should include only the dry mass of SnO_2, any impurities, and Ni particles initially encapsulated in the VACNTs tip, as all the carbonaceous species, such as CNTs and amorphous carbon, should be burnt off by 700 °C [40]. The TGA spectra revealed that the weight percentage of SnO_2 nanoparticles was ~40% of the total weight of SnO_2-VACNTs, which was obtained by subtracting the final remaining weight of the VACNTs from the final residual weight of SnO_2-VACNTs after 800 °C.

3.1.5 Raman spectroscopy and XRD analysis

Raman spectra displayed in **Fig. 3(b)** revealed an increase in the I_D/I_G ratio from 1.12 to 1.18, where I_D and I_G represent the intensity of D-band and G-band, respectively. This result indicates that the SnO_2 coating increased the defects on the VACNTs [41]. The defects were created on the VACNTs of the SnO_2-VACNTs sample due to the acid treatment of the VACNTs prior to SnO_2 coating. It has been reported that the presence of defects on the surfaces and tips of CNTs, such as vacancies, dangling bonds, edge dislocations, and functionalization sites, can serve as extra sites for Li^+ intercalation and adsorption, thereby increasing their lithium storage capacity [42]. In addition, it has also been reported that defects in the CNTs can lower the energy barrier for the Li^+ diffusion process [43]. These results indicate that the defective VACNTs in the SnO_2-VACNTs anode can potentially improve the overall electrochemical lithiation properties of the SnO_2-VACNTs anode. Furthermore, the functionalization of the VACNTs with oxygen-containing functional groups was essential for promoting the SnO_2 coating procedure. Moreover, as shown in **Fig. 3(c),** the crystal structure of VACNTs and SnO_2-VACNTs was investigated by XRD. The XRD spectrum of the SnO_2-VACNTs demonstrates the peaks related to crystal planes at 2θ positions of ~26.6°, 33.9°, 42.6°, and 51.4°. These peak positions can be assigned to (110), (101), (210), and (211) planes of the t-SnO_2 crystal. This result is consistent with the above TEM results and those reported in a publication [44]. In the XRD spectra shown in **Fig. 3(c)**, the peaks at ~26° and 42° correspond to the graphitic C signal from VACNTs.

3.1.6 FTIR analysis

As shown in **Fig. 3(d)**, FTIR spectra were used to determine the functional groups present on the VACNTs treated with HNO_3 only and coated with SnO_2 nanoparticles. It has been reported that treatment with a strong oxidizing agent such as HNO_3 can create different functional groups at the defect sites of CNTs [45]. The wide-survey FTIR spectra between 4000

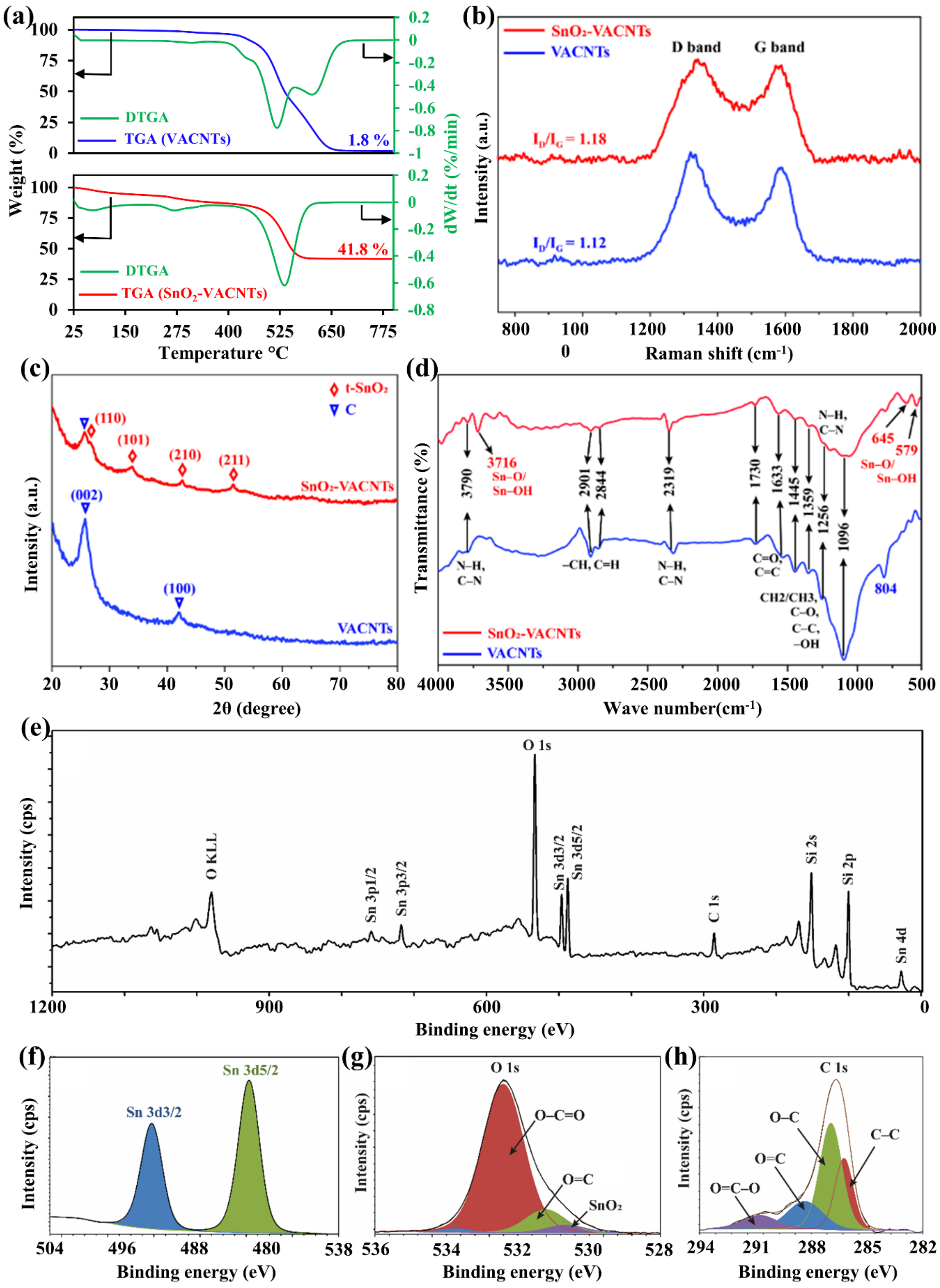

Fig. 3. (a) TGA, (b) Raman, (c) XRD, and (d) FTIR spectra of VACNTs and SnO_2-VACNTs. (e) The wide-survey and (f-h) high-resolution XPS spectra of SnO_2-VACNTs.

cm^{-1} and 500 cm^{-1} of both samples exhibited signals related to the C=C, C=O, C–N, and N–H stretching vibrations. In detail, peaks at wave number positions ~3790 cm^{-1}, 2319 cm^{-1}, and 1256 cm^{-1} are related to N–H and C–N bonds and can be accredited to adsorbed H_2O and NH_3 on the VACNT wall [46]. Moreover, the signals related to the –CH and C=H band stretching vibrations can be observed at 2901 cm^{-1} and 2844 cm^{-1}, respectively [47]. The peaks at ~1730 cm^{-1} and 1633 cm^{-1} can be assigned to the carboxyl (C=O) group and graphene layer (C=C) of VACNTs [45, 48, 49]. Furthermore, the band stretching signals at 1445 cm^{-1}, 1359 cm^{-1}, 1096 cm^{-1}, and 804 cm^{-1} are related to the CH_2/CH_3, C–C, C–O, and –OH group, respectively [50]. The composite material comprised of SnO_2 and carbon materials was further confirmed by the presence of signals at ~3716 cm^{-1}, 645 cm^{-1}, and 579 cm^{-1} [47, 51].

3.1.7 XPS analysis

The surface chemical constituents of the SnO_2-VACNTs were studied using XPS, as shown in **Figs. 3(e-h)**. A wide-survey XPS spectrum of the SnO_2-VACNTs (**Fig. 3(e)**) revealed the presence of C, O, and Sn (3p, 3d, and 4d). The prominent peaks of Sn and O suggested the existence of SnO_2 nanoparticles, whereas the C signal can be attributed to the VACNTs. In addition, the intense peaks of Si are ascribed to the Si substrate on which a thin layer of the SnO_2-VACNTs was deposited for the XPS measurements. The high-resolution Sn, O, and C peaks were analyzed to explain the chemical valence of elements in the SnO_2-VACNTs. As shown in **Fig. 3(f)**, the Sn 3d core level spectrum of SnO_2 demonstrated two distinct peaks centered at 487.7 and 496.2 eV corresponding to Sn $3d_{5/2}$ and Sn $3d_{3/2}$ levels of the energy splitting reported for SnO_2 [52], respectively. This result can be attributed to the Sn^{4+} valence state in the tetragonal rutile structure of the SnO_2 crystal [53]. The binding energy values for the spin-orbit splitting of the Sn 3d level are in close agreement with the binding energy values reported in the literature [52-55]. Detailed analysis of XPS spectra of O 1s for the SnO_2-VACNTs is shown in **Fig. 3(g)**. The high-resolution spectra revealed the presence of oxygen in three chemically nonequivalent states, represented by three well-fitted peaks in the spectrum of O 1s. The peak at a binding energy of 531.3 eV can be ascribed to oxygen in the composition of SnO_2 (i.e., O^{2-} of SnO_2) [53]. Furthermore, the XPS peaks at 532 and 533.5 eV correspond to oxygen in the O=C and O–C=O bonds, respectively, which can be attributed to the oxidation of VACNT sections uncoated by SnO_2 nanoparticles [53]. **Fig. 3(h)** shows the high-resolution XPS spectrum of C 1s, which consists of four well-fitting peaks centered at 284.9, 285.7, 287.4, and 290.2 eV corresponding to the C–C, O–C, C=O, and O=C–O groups, which are in agreement with the previous reports [52, 56].

3.2 Electrochemical lithiation properties

3.2.1 Electrochemical properties test in half-cell configuration

The electrochemical Li^+ storage properties of SnO_2 and SnO_2-VACNTs were investigated using cyclic voltammetry (CV) between 0.01 and 3 V (vs. Li/Li^+) for five cycles, as shown in **Figs. 4(a, b)**. The cell potential was swept at a constant scan rate of 0.2 mV s^{-1}, and the corresponding current was recorded. Sharp irreversible reduction peak at ~1.08 V for SnO_2 and ~0.81 V for SnO_2-VACNTs during the first cycle suggested the solid electrolyte interphase (SEI) formation on the electrode surface due to the decomposition of organic solvents such as EC and DEC. The reduction peaks can also be related to the initial irreversible reduction of SnO_2 to Sn and Li_2O (**Eq. 1**) [57]. The reversible reduction peak at ~0.56 V for the SnO_2 can be attributed to the alloying of Li with Sn. However, this reduction peak emerged at a much lower voltage of ~0.27 V for the SnO_2-VACNTs anode. Another reduction peak for the SnO_2 anode was detected in the range of ~1.5 – 1.67 V, and interestingly, both the peak position and intensity were decreased with the CV cycles. The reversible oxidation peaks at ~1.05 V, 1.41 V, and 2.29 V for the SnO_2 anode can be assigned to the dealloying of Li_xSn (**Eq. 2**) [58] and oxidation of Sn^{+2}. Similar to the reversible reduction peak, these reversible oxidation peaks for the SnO_2-VACNTs anode were observed at lower potentials of ~0.67, 1.32, and 2.01 V, respectively, compared to those for the SnO_2 anode. The shift of these peak positions toward the lower potential side for the SnO_2-VACNTs anode may be attributed to the lower impedance of the anode compared to the SnO_2 anode, as shown in the 1st and 5th impedance spectra in **Figs. 5(a, b)**. The SnO_2-VACNTs anode exhibited stable CV cycles after the first cycle in terms of peak positions and area under the curves, which may indicate long-term cycle stability with good capacity retention. It is well known that CNTs are also electrochemically active materials for Li^+ storage. A detailed description of the CV and galvanostatic charge/discharge potential profiles of VACNTs anodes measured in half-cell configurations is provided in **Fig. S2** (Supplementary Information). Furthermore, we also conducted an in-situ TEM experiment to understand the lithiation process of the SnO_2-VACNTs anode and a detailed explanation is provided in **Fig. S3** and **S4** (Supplementary Information).

Figs. 4(c, d) show the galvanostatic lithiation/delithiation potential profiles of SnO_2 and SnO_2-VACNTs at different cycles measured at a current density of 0.1 A g^{-1} between cut-off potentials of 0.01 V and 3 V (vs. Li/Li^+). The first lithiation and delithiation capacities for the SnO_2 electrode were 3080 mAh g^{-1} and 2160 mAh g^{-1}, respectively. Also, the first lithiation and delithiation capacities for the SnO_2-VACNTs anode were 3530 mAh g^{-1} and 2360 mAh g^{-1}, respectively. Theoretical calculations have implied that reversible capacity exceeding a LiC_2 stoichiometry [59, 60], which is equivalent to ≥1116 mAh g^{-1}, is achievable for CNTs [61]. Also, considering the theoretical specific capacity of SnO_2 as 1493 mAh g^{-1} [12], the theoretical specific capacity of the SnO_2-VACNTs can be calculated as 1267 mAh g^{-1}. That means that the experimental capacities of the SnO_2-VACNTs exceeded the theoretical limit significantly. It is strange, in general, for an electrode to show a higher capacity than the theoretical limit; however,

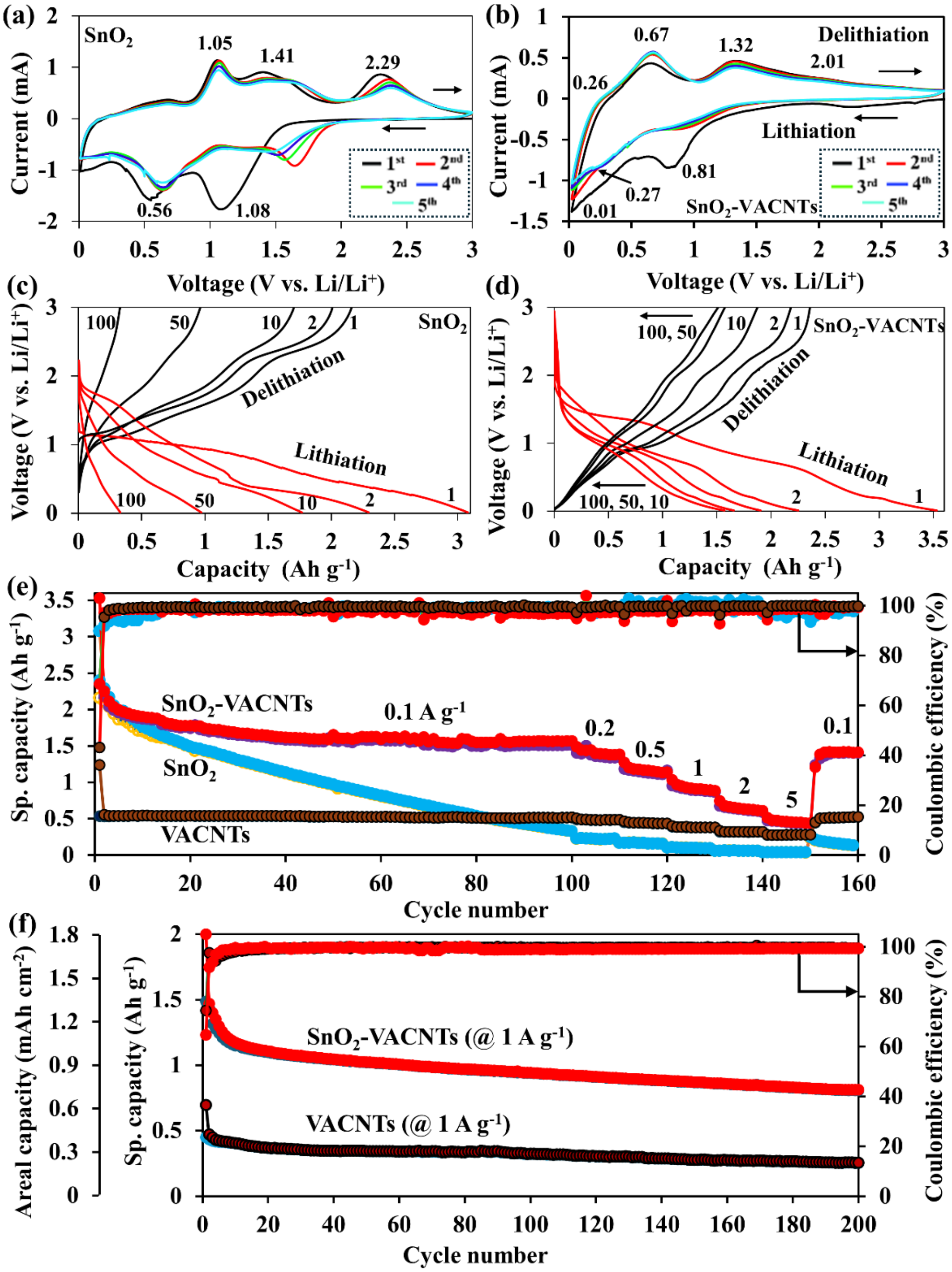

Fig. 4. (a, b) Cyclic voltammograms of SnO_2 and SnO_2-VACNTs scanned at 0.2 mV s^{-1} between 0.01 and 3 V. (c, d) Galvanostatic charge/discharge potential profiles of SnO_2 and SnO_2-VACNTs at the current density of 0.1 A g^{-1} between 0.01 to 3 V. (e) Cyclability and rate performance tests of SnO_2, VACNTs, and SnO_2-VACNTs anodes. (f) Cycling performance of the VACNTs and SnO_2-VACNTs anodes at a high current density of 1 A g^{-1}.

such an anomaly has been encountered in the past only in the case of ultrafine (typically ≤ 10 nm) SnO_2 nanoparticle-based anodes [62, 63]. This anomaly can be accredited to the interfacial storage of Li^+ at the phase boundaries of ultrafine SnO_2 nanoparticles. Theoretical calculations and experimental results have shown that nanocomposites composed of extremely fine nanoparticles with high surface area-to-volume ratios can demonstrate extra lithium storage capacity [64, 65]. Because the size of the SnO_2 nanoparticles in the SnO_2-VACNTs composite was only ~5 nm, they possess an extremely high interfacial surface-to-volume ratio and, thus, a great potential for interfacial Li^+ storage. Furthermore, it should also be noted that the defects on the VACNTs created due to the acid treatment (see **Section 3.1.5**) and the high surface-to-volume ratio of the VACNTs may have provided extra lithium storage capacity. On the other hand, the absence of VACNTs and the difference in SnO_2 morphology may have led to a lower initial capacity of the SnO_2 anode compared to the SnO_2-VACNTs composite anode.

Both electrodes showed initial coulombic efficiencies of about 70%. The specific capacities of both electrodes dropped significantly in the second cycle, suggesting poor capacity retention due to irreversible capacity loss. A plateau at ~1.1 V in the first lithiation curve of the SnO_2 anode is associated with the SEI and amorphous Li_2O matrix formation, and another plateau at ~0.5 V can be related to the alloying of Li with Sn metal [66-68]. In contrast, a plateau at ~1.4 V in the first lithiation curve of the SnO_2-VACNTs anode may be ascribed to the irreversible reduction of oxygen-containing surface species on VACNTs [67]. Also, the plateau that emerged at ~0.8 V can be accredited to the formation of SEI and amorphous Li_2O. These results agree well with the results obtained from the CV measurement, although a reduction peak related to the plateau at ~1.4 V in the first lithiation curve of the SnO_2-VACNTs was not observed in the first CV cycle. The potential profiles at different cycles for the SnO_2 anode displayed continuous capacity degradation as the cycle increased. However, the SnO_2-VACNTs anode exhibited improved stability compared to the SnO_2 anode.

The long-term cycle stability test of the pristine VACNTs, SnO_2, and SnO_2-VACNTs anodes was assessed for 100 cycles of lithiation and delithiation at a current density of 0.1 A g^{-1} followed by rate performance tests after 100 cycles, and the results are shown in **Fig. 4(e)**. The VACNTs anode displayed excellent cyclability with a delithiation capacity of ~535 mAh g^{-1} after 100 cycles, which is ~4% degradation in delithiation capacity with respect to the first cycle. In contrast, the SnO_2 anode showed continuous capacity decay with a low delithiation capacity of ~327 mAh g^{-1} after 100 cycles. The SnO_2-VACNTs anode displayed considerably more stable cycle performance than the SnO_2 anode with a high delithiation capacity of ~1512 mAh g^{-1} after 100 cycles. It should be noted that the SnO_2-VACNTs anode also suffered significant capacity fading during the first 20 cycles, but it became stable after the first 20 cycles. The initial poor cyclability of the SnO_2-VACNTs anode may be attributed to the significant volume alteration and pulverization of SnO_2 nanoparticles, which led to the detachment of the SnO_2 nanoparticles poorly bonded to the VACNT wall. In addition, this significant capacity fading during the initial cycles may also be attributed to the coating of SnO_2 on the bare area of Ni foam where VACNTs were not present. The SnO_2 coated on Ni foam can be easily detached from the Ni foam due to the pulverization during the lithiation/delithiation process. The poor cycle stability of the SnO_2

anode, as shown in **Fig. 4(e)**, further supports this hypothesis. Furthermore, VACNTs and SnO_2-VACNTs anode materials demonstrated excellent rate capability, as shown in **Fig. 4(e)**. At current densities of 0.2, 0.5, 1, 2, and 5 A g^{-1}, the reversible capacities of the SnO_2-VACNTs were ~1382, 1137, 895, 625, and 449 mAh g^{-1}, respectively. Also, the rate performance exhibited that the SnO_2-VACNTs anode retained ~83 % of its reversible capacity at 0.1 A g^{-1} compared to the specific capacity at the 100th cycle at the same rate, as shown in **Fig. 4(e)**. In contrast, the SnO_2 anode exhibited poor rate performance, as shown in **Fig. 4(e)**. In addition, the SnO_2-VACNTs anode showed a stable long-term cycling test with a capacity retention of ~60% and a specific capacity of 813 mAh g^{-1} at a high rate of 1 A g^{-1} after 200 cycles, as shown in **Fig. 4(f)**. Although the capacity retention is lower, the specific capacity of the SnO_2-VACNTs anode at the 200th cycle at the current rate of 1 A g^{-1} is better or comparable compared to similar electrodes reported in the literature [69-71]. Furthermore, **Table 1** compares the half-cell performance of the SnO_2-VACNTs anode with similar anodes reported in various literature.

Table 1. Half-cell performance comparison of the SnO_2-VACNTs anode with similar anodes reported in various literature.

Active material	SnO_2 size (nm)	Half cell performance			Ref.
		Cycle number (n)	Sp. capacity (mAh g^{-1}) at nth cycle	Current rate	
SnO_2	3-8	200	1425	0.1 A g^{-1}	[12]
SnO_2	3-8	350	1062	1 A g^{-1}	[12]
SnO_2	3-10	40	760	0.1 A g^{-1}	[72]
Sn-CNF	100	200	774	0.8 A g^{-1}	[73]
SnO_2@CNTs	4	200	1192	0.223 A g^{-1}	[74]

Fe-doped SnO_2	7-8	50	600	0.05 A g^{-1}	[63]
Sb-doped SnO_2-rGO	3	100	813	1.249 A g^{-1}	[75]
F-doped SnO_2-rGO	5	200	1439	0.2 A g^{-1}	[62]
SnO_2-VACNTs	5	100	1512	0.1 A g^{-1}	This work
SnO_2-VACNTs	5	200	813	1 A g^{-1}	This work

AC impedance measurements of the different electrodes were carried out using electrochemical impedance spectroscopy (EIS). The impedance measurements were conducted in the potentiostatic mode using a sine wave of 5 mV amplitude between 100 kHz and 50 mHz frequency range. The impedance measurements were carried out at different lithiation/delithiation cycles to understand the impedance evolution of electrodes with cycle age. For a fair comparison between different cycles and samples, cells were completely delithiated first and rested for three hours for cell stabilization before the EIS measurements. **Figs. 5(a, b)** show Nyquist plots of the SnO_2 and SnO_2-VACNTs at different cycle ages. The intercept by the EIS spectrum on the Z' axis at high frequencies corresponds to the equivalent series resistance (R_s) related to the total resistance of the electrolyte, separator, and electrical contacts. The spectra also comprise a small semicircle at high frequencies followed by a larger semicircle in the high-to-medium frequency region. Furthermore, the plots show another semicircle in the medium-to-low frequency region, which becomes more prominent as the cell ages (after the 5th cycle), and a straight line inclined to the real axis (Z' axis) at low frequencies. The high-frequency semicircle with a small diameter can be attributed to the impedance related to the SEI (C_{SEI}, R_{SEI}) developed on the electrode surface due to the electrolyte reduction, while the second semicircle with a larger diameter can be attributed to the impedance related to the charge transfer through double layer (C_{DL}, R_{CT}) during the lithiation/delithiation reaction [76-78]. An interesting feature of the impedance spectra shown in **Fig. 5(a, b)** is the presence of the third semicircle in the medium-to-low frequency region. The origin of this semicircle in the EIS spectra is discussed in detail in the following paragraphs. Also, the straight line at the low-frequency region of the impedance spectrum is related to the lithium diffusion process within the electrode [79]. In addition, it should be noted that the size of the semicircles, particularly those related to the charge transfer, decreased significantly until the 50th cycle for both electrodes. After the 50th cycle, it increased substantially up to the 100th cycle for the SnO_2 cell. However, for SnO_2-VACNTs, the semicircles related to the charge transfer and the SEI were almost unchanged from the 50th cycle

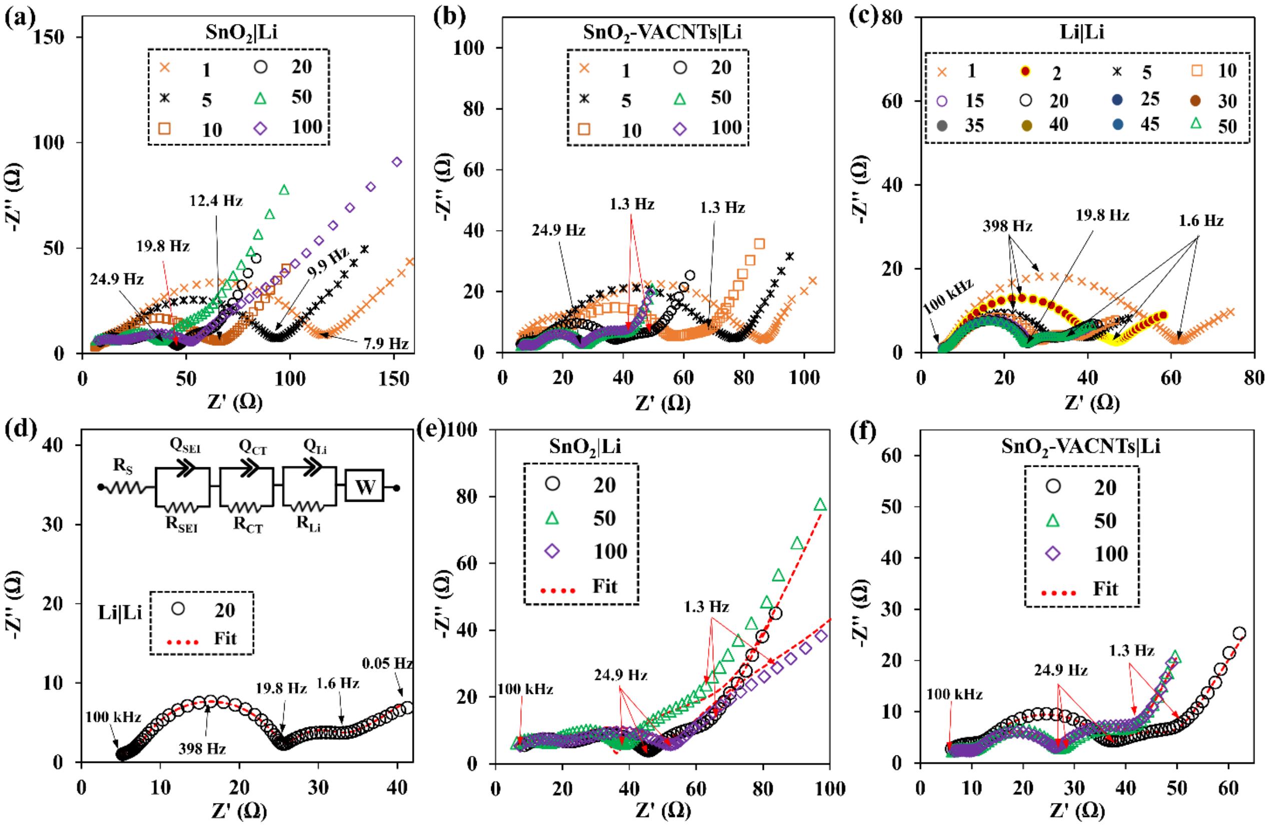

Fig. 5. EIS spectra of (a) SnO_2, (b) SnO_2-VACNTs, and (c) lithium-lithium symmetric cell measured at various cycles. Experimental and fitted EIS spectra of the (d) lithium-lithium symmetric cell at the 20th cycle, (e) SnO_2, and (f) SnO_2-VACNTs measured at the 20th, 50th, and 100th cycles. The inset in panel (d) represents an ECM for fitting measured EIS spectra.

to the 100th cycle, as shown in **Fig. 5(b)**, indicating stable SEI and efficient charge transfer process without a significant increase in the impedance. In this case, it should be noted that the half-cell impedance represents the combination of the interfacial properties of both the working electrode and the lithium counter electrode. Therefore, the EIS spectrum of a half cell does not correctly characterize the interfacial properties of a single working electrode [80, 81].

In order to accurately evaluate and isolate the interfacial electrochemical properties of the working electrode from the counter/reference electrode, a symmetric test cell with identical working and counter electrodes of lithium foil was used [80]. The lithium symmetric cell was polarized (charged and discharged for 30 minutes each) using a current density of 0.1 mA cm^{-2}, and EIS measurements were carried out at various cycles, as shown in **Fig. 5(c)**. The impedance spectra comprise a small semicircle at high frequencies related to the SEI, a large semicircle in the high-to-medium frequency region related to the charge transfer, another semicircle in the medium-to-low frequency (~20 – 1.6 Hz) region, and a Warburg diffusion region. Interestingly, the small semicircle in the medium-to-low frequency region emerged only after the first cycle and gradually evolved with the cell age. Regarding its frequency range and evolution with the cell aging, this result implies that the third semicircle in the EIS can be related to the surface morphology evolution-driven reaction kinetics on the lithium electrode. During the initial few cycles, lithium preferentially deposits on the lithium electrode surface as mossy dendrites that increase the surface area, offering lower-impedance pathways for charged particles [82]. As a result, charge transfer resistance significantly decreased until the 20th cycle (**Fig. 5(c)**). As the cell ages, these mossy dendrites can be mechanically detached and electrically isolated from the bulk lithium surface, creating a tortuous interphase layer (TIL) [54], different from the SEI, between the bulk lithium surface and electrolyte. This TIL can limit mass transport (observable at low frequencies) during cell cycling, and hence, the third semicircle in the EIS spectrum can be associated with this phenomenon.

In addition, the impedance of the symmetric cell stabilized after the 20th cycle and remained similar afterward. Therefore, the decrease in the overall impedance of SnO_2 and SnO_2-VACNTs half cells during the initial 20 cycles can be attributed partially to the lithium counter electrode. Furthermore, the EIS of the symmetric cell at the 20th cycle (**Fig. 5(d)**) is selected to estimate the contribution of the lithium counter electrode in the impedances of SnO_2 and SnO_2-VACNTs half cells. The symmetric cell consists of two similar lithium-electrolyte interfaces. Hence, the impedance of the symmetric cell represents a doubling of a single lithium electrode. The values of circuit components obtained by fitting the EIS spectrum of the symmetric cell at the 20th cycle using an equivalent circuit model (ECM) (inset of **Fig. 5(d))** are presented in **Table 2**.

The ECM comprises serial resistance (R_s), representing the cell's ohmic resistance, and three parallel resistor-constant phase element (R-Q) networks, corresponding to three semicircles in the measured EIS spectra. The ECM uses constant phase elements to simulate depressed semicircles in the EIS spectra [83]. An R-Q parallel network can be estimated with a resistor-capacitor (R-C) parallel network, and the capacitances related to the different electrochemical events in the electrode (C_{SEI}, C_{DL}, C_{Li}) can be calculated using the following equation.[

$$C = [(R^*Q)^{1/\alpha}]/R \qquad (3)$$

where α is a constant with values between 0 and 1 [84].

Table 2. Element values obtained by fitting the EIS spectra of SnO_2, SnO_2-VACNTs, and Li-Li symmetric cells using the ECM shown in the inset of **Fig. 5(d)**.

Electrode	Cycle	R_S (Ω)	R_{SEI} (Ω)	C_{SEI} (μF)	R_{CT} (Ω)	C_{DL} (μF)	R_{Li} (Ω)	C_{Li} (mF)	D_{Li^+} (cm^2 s^{-1})
SnO_2									
	20	4.11	14.95	0.24	18.29	11.82	23.86	6.08	4.3×10^{-13}
	50	3.21	13.75	0.26	16.54	9.94	30.88	3.89	1.9×10^{-13}
	100	4.89	12.22	0.30	35.64	6.35	37.99	7.54	3.9×10^{-14}
SnO_2-VACNTs									
	20	3.81	8.10	0.48	25.33	12.57	10.73	4.53	1.2×10^{-12}
	50	4.16	5.56	0.46	17.65	18.08	12.37	6.80	2.2×10^{-12}
	100	4.34	5.38	0.42	18.49	21.29	13.44	7.03	2.5×10^{-12}
Li-Li									
	20	4.49	3.05	1.78	17.41	17.12	4.76	12.55	2.5×10^{-12}

Figs. 5(e, f) show the experimental and fitted impedance spectra of SnO_2 and SnO_2-VACNTs at the 20th, 50th, and 100th cycles using the ECM, and fitting parameters are shown in **Table 2**. The table shows that resistances, R_{SEI} and R_{CT}, decreased after the 20th cycle up to the 50th cycle for both electrodes, which can be ascribed to the decomposition of the electrolyte on the electrode surface that generates protons, which in turn enhances the conductivity, lowering the impedance of the passivated film and charge transfer [81]. After the 50th cycle, the R_{SEI} and R_{CT} increased significantly for the SnO_2 electrode. This increase can be attributed to the continuous SEI formation and the active material (SnO_2) detachment from the Ni foam due to continuous and significant volume alteration and pulverization during the lithiation/delithiation process [85]. The continuous capacity fading during the cyclability test and poor rate performance at the high current density, as shown in **Fig. 4(e)**, are in agreement with the increased SnO_2 electrode resistances.

On the other hand, the R_{SEI} and R_{CT} values remained nearly similar from the 50th to 100th cycles for the SnO_2-VACNTs electrode, and R_{CT} is significantly smaller compared to the SnO_2 electrode at the 100th cycle, indicating fast electron transport and faradaic reactions at the electrode surface assisted by highly conductive VACNTs, strong adhesion of SnO_2 nanoparticles on the VACNTs aided by the functional groups on the VACNTs wall, and direct connection of VACNTs to the current collector (Ni foam). As a result, the SnO_2-VACNTs electrode exhibited a much better cycle stability and rate performance than the SnO_2 electrode. Also, it should be noted that the capacity fading of the SnO_2-VACNTs during the first few cycles (**Figs. 4(e, f)**) can be ascribed to the resistance increase due to the formation and continuous thickening of SEI along with the loss of SnO_2 active materials. In contrast, the R_{Li} increased continuously from the 20th to the 100th cycle for both electrodes. Furthermore, it should also be noted that the time constants corresponding to the third semicircle ($R_{Li}*C_{Li}$) for the SnO_2 and SnO_2-VACNTs half cells are higher than that for the symmetric lithium-lithium cell. These results indicate that the third semicircles in the frequency range of ~20 – 1.6 Hz in EIS spectra of the SnO_2 and SnO_2-VACNTs may not have originated solely due to the lithium counter electrode, and working electrodes may have contributed to the evolution of the third semicircle. This complicates the isolation of the working electrode impedance entirely from the counter electrode impedance and requires more in-depth study.

Furthermore, the solid-state diffusion property of SnO_2 and SnO_2-VACNTs electrodes was studied using the Li^+ diffusion coefficient (D_{Li^+}) given by the following equations [86].

$$D_{Li^+} = (R^2\, T^2)/(2A^2\, n^4\, F^4\, C^2\, \sigma_w^2) \qquad (4)$$

where R (8.314 J mol^{-1} K^{-1}) is the gas constant, T (298 K) is the absolute room temperature, A (0.785 cm^2) is the area of the electrode, n (4.4, regarding Sn alloying with Li up to a maximum theoretical limit of $Li_{22}Sn_5$ [87]) is the number of electrons per species reaction during the oxidation/reduction reaction, F (96500 C mol^{-1}) is the Faraday constant, σ_w is the Warburg's impedance coefficient, and C (0.001 mol cm^{-3}) is the molar concentration of Li^+ ions. The values of σ_w were determined by fitting the experimental data using Warburg's element in the ECM, as shown in the inset of **Fig. 5(d)**. The Li^+ diffusion coefficients of SnO_2, SnO_2-VACNTs, and lithium-lithium symmetric cells calculated using eq. (4) are presented in **Table 2**. The table shows that the Li^+ diffusion coefficients of the SnO_2-VACNTs electrode are significantly higher than that of the SnO_2 electrode. This result suggests that the ultra-fine SnO_2 particles (< 5 nm) coated on VACNTs with proper inter-tube distance and better electrolyte accessibility could provide more favorable Li^+ transportation kinetics and shorten the Li^+ diffusion pathway at the

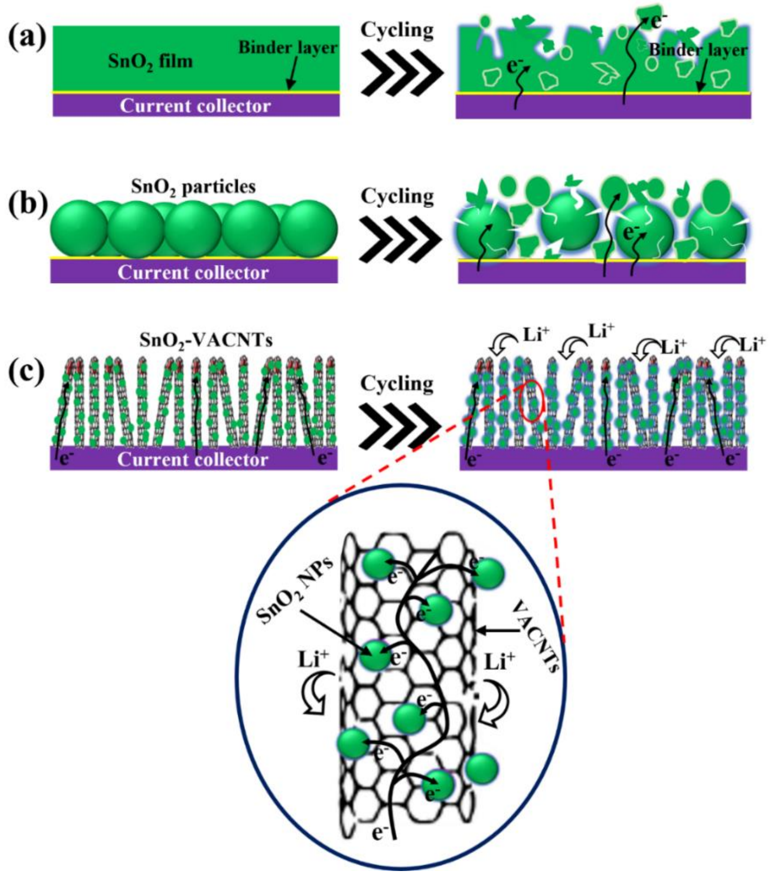

Fig. 6. Schematic representation of morphological changes in SnO_2 (thin film, macro-particles, and nanoparticles on VACNTs) electrodes due to electrochemical cycling.

electrode/electrolyte interfaces. Since Li^+ diffusion is directly related to the rate capability of the electrode, higher reversible capacities with remarkable stability of SnO_2-VACNTs at higher current densities (**Figs. 4(e, f)**) further indicate the faster Li^+ transportation kinetics and shorter Li^+ diffusion pathway compared to the SnO_2 electrode.

The Li^+ storage performance of the SnO_2-VACNTs anode can be described using a schematic, as shown in **Fig. 6**. The SnO_2 electrode undergoes a large volume change during the lithiation process, leading to fracture in bulk or micron/macro-sized materials (**Figs. 6(a, b)**) [88]. Due to this, materials lose connection with the current collector. As a result, electrodes face severe capacity decay as electronic charge carriers should move through interparticle contact areas, as shown in **Figs. 6(a, b)**. Previous reports have recommended a materials-dependent critical particle size below which particles do not pulverize upon lithiation [89]. In addition, binders used for active materials coating on the current collector can seriously undermine the electrode's overall conductivity and add extra weight (so-called dead weight) to the electrode. In contrast, in the case of SnO_2-VACNTs electrodes, VACNTs were synthesized directly on the catalytic metal current collector substrate (3D Ni foam). Each VACNT coated with SnO_2 NPs was electrically connected to the metallic current collector, so all the SnO_2-VACNT nanowires contributed to the capacity. Also, the VACNTs have direct one-dimensional electronic pathways (**Fig. 6(c)**), ensuring efficient charge transport to individual SnO_2 NPs, which can be very important for the high-rate performance of the electrode. Furthermore, an array structure with a regular space between the SnO_2-VACNT nanowires can effectively accommodate the large volume changes due to efficient strain relaxation and significantly improve the electrolyte accessibility during the lithiation/delithiation process.

3.2.2 Cycling test in full-cell configuration

In order to understand the practical applicability of the SnO_2-VACNTs as an anode for LIBs, we assembled a coin-type full cell composed of the SnO_2-VACNTs anode and a $LiNiMnCoO_2$ (NMC) cathode with the positive-to-negative electrode capacity ratio (P/N) of ~1.1. The physical morphology characterization of the NMC cathode by SEM and its electrochemical properties in the half-cell configuration are presented in Supplementary Information (**Section 4, Fig. S5**). A low initial coulombic efficiency (ICE ≤ 80%), which is most prevalent in alloying/dealloying-type electrodes, is one of the reasons for preventing these types of electrodes in practical applications. The low ICE requires an excessive amount of cathode materials (≥10%–15% even for typical graphite anodes) to overcome the low ICE of the anode, resulting in a significant decrease in energy density [90]. A few methods, such as electrolyte optimization and pre-lithiation of the anode by direct contact with lithium metal, have been proposed to improve the ICE of the alloying/dealloying-type anodes composed of nanoparticles [90, 91]. However, the SnO_2-VACNTs electrode in this work was pre-lithiated in a half-cell for three cycles prior to assembly of the full cell to reduce the effect of the poor ICE. Furthermore, the potential profiles of the SnO_2-VACNTs anode (vs. reference), NMC cathode (vs. reference), and full cell were measured using a three-electrode coin-type cell with a lithium reference electrode to determine the cutoff potentials of the full cell, as shown in **Fig. 7(a)**.

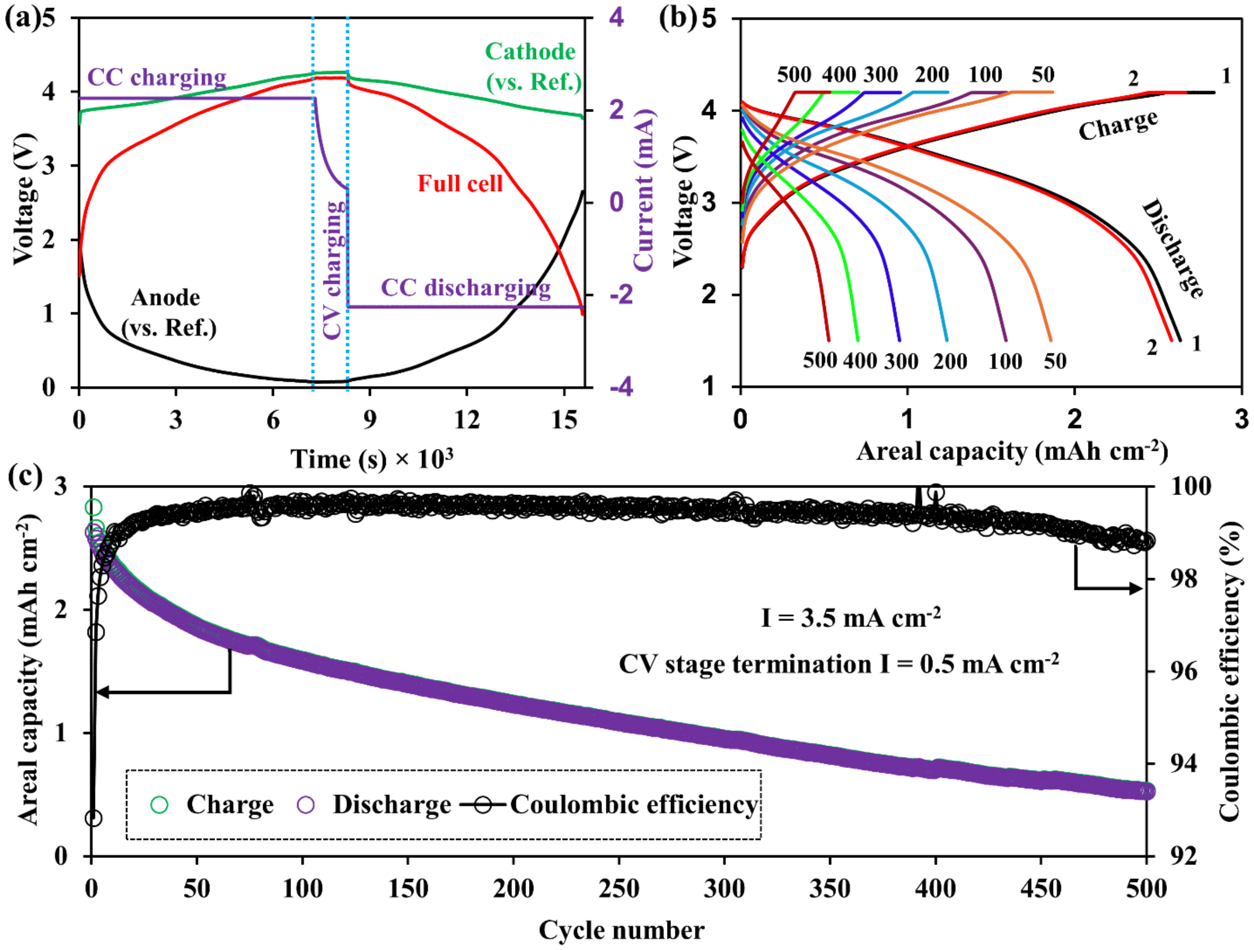

Fig. 7. (a) Current and potential profiles of the SnO_2-VACNTs anode (vs. Li reference), NMC cathode (vs. Li reference) and full cell during the charge/discharge of a three-electrode cell. (b) Charge/discharge potential profiles during different cycles and (c) long-term cycling test of the SnO_2-VACNTs/NMC full cell.

Fig. 7(b) shows the charging and discharging potential profiles of the full cell at different cycles within the potential range of 1.5–4.2 V. During the charging stage, a constant current (CC) of 3.5 mA cm^{-2} was applied until the cell potential reached 4.2 V and then the cell potential was kept constant (CV) until the current reduced to 0.5 mA cm^{-2}. In contrast, the cell was discharged using the constant current (CC) of 3.5 mA cm^{-2} until the cell potential decreased to 1.5 V. The first cycle areal charge and discharge capacities of the full cell were 2.83 mAh cm^{-2}

and 2.63 mAh cm^{-2}, respectively, with an ICE of ~91%, which is much higher than the ICE the SnO_2-VACNTs anode measured in half-cell and can be attributed to the prelithiation. Furthermore, the first areal discharge capacity of the cell is about an industrially acceptable areal capacity level (~3 mAh g^{-1}) [92]. However, the areal capacity rapidly decreased by ~29% after 50 cycles, retained the areal capacity of ~47% after 200 cycles and only ~20% after 500 cycles, as shown in **Figs. 7(c)**, which is significantly low and indicates that the cyclability of the SnO_2-VACNTs anode must be improved for future practical applications. One of the possible reasons for this rapid capacity fade of the SnO_2-VACNTs/NMC full cell can be the detachment of SnO_2 nanoparticles from the VACNTs due to the high charging rate of 2.06 A g^{-1} (or 3.5 mA cm^{-2}). The anode active material loading was significantly increased by increasing the VACNTs growth time and SnO_2 coating time for the full cell testing compared to the anode for half cell testing. The increase in coating time may have increased the SnO_2 coating thickness, making it weakly bonded to the VACNT and vulnerable to detaching from the host VACNT. In addition, it should be noted that the full cell achieved 80, 90, and 100% state of charge in 38, 43, and 56 minutes, respectively, as shown in **Fig. S6** (Supplementary Information). This result indicates that the SnO_2-VACNTs anode may have potential applications in future fast-charging high-energy-density LIBs.

3.3 Anode aging analysis

The SnO_2-VACNTs anode morphology after 500 fast-charged cycles in the full-cell configuration was examined using SEM spectroscopy. As shown in **Figs. 8(a, b)**, the spongy, porous, and aligned morphology of SnO_2-VACNTs remained intact on the Ni foam substrate even after the extended cycling test. This result suggests that VACNTs were strongly connected to the Ni foam current collector as they were directly synthesized on the Ni metal substrate. This inherent connection between the current collector (Ni foam) and active materials (SnO_2-VACNTs) is crucial for developing a binder-free anode. Furthermore, signals related to C, Sn, and O in the SEM-EDS elemental mapping (**Figs. 8(c-e)** and **Fig. 8(h)**) demonstrate the uniform distribution of the active materials and are still available in the electrode even after the long cycling for further electrochemical Li^+ storage reaction. As shown in **Figs. 8(f-h)**, the signals P and F should be from the SEI and $LiPF_6$ electrolyte remanents, although the electrode was thoroughly cleaned using DMC before taking SEM images. Also, the Ni and Al signals, as

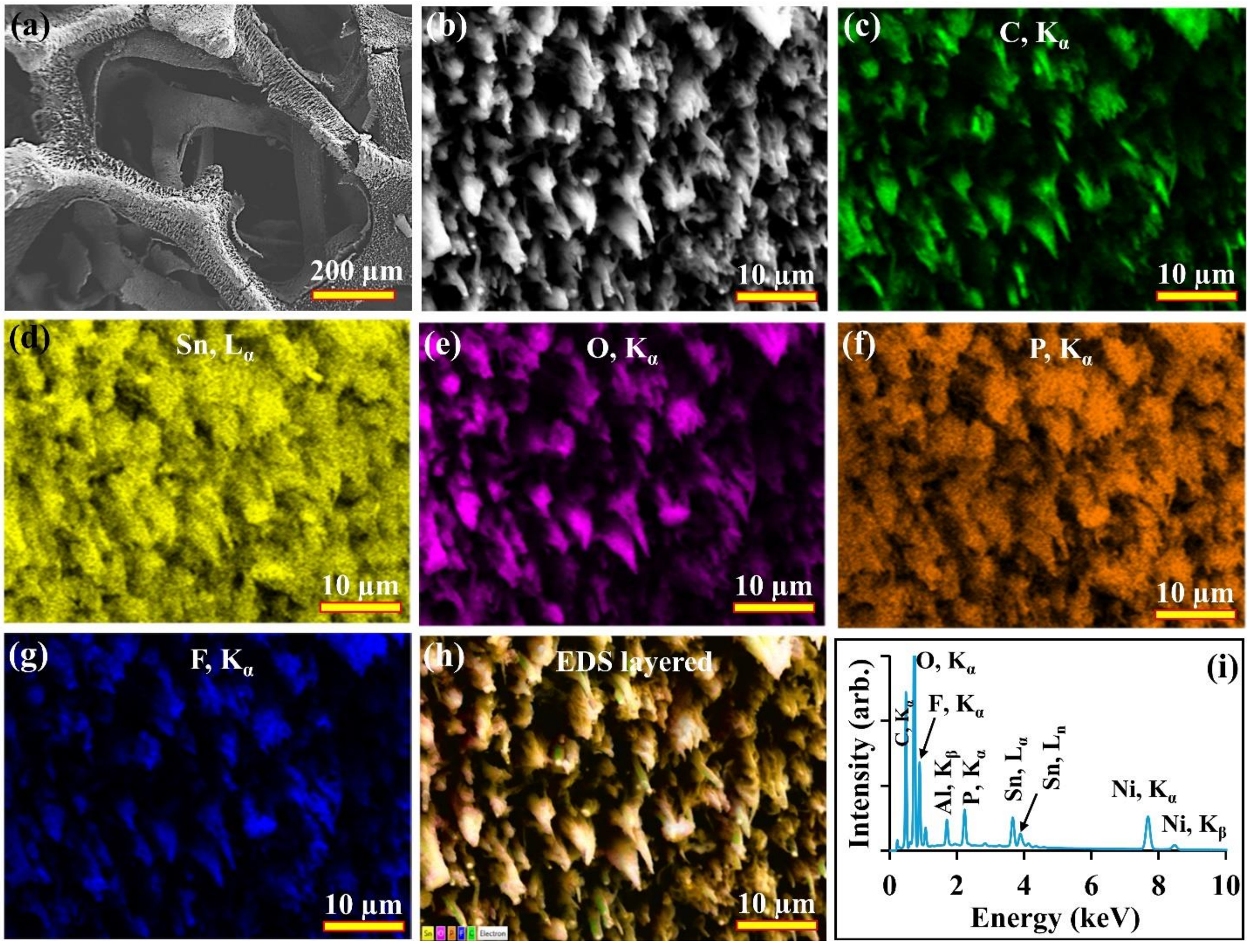

Fig. 8. (a, b) Low and high magnification SEM images, (c-h) SEM-EDS mapping (C, Sn, O, P, F, and their overlap) images, and (i) corresponding EDS spectrum of the SnO_2-VACNTs anode after 500 cycles tested in the full-cell.

shown in **Fig. 8(i)**, can be attributed to the Ni foam substrate and SEM sample holder, respectively.

The excellent performance of the SnO_2-VACNTs anodes can be ascribed to the following factors: (1) 3D Ni foam host for 1D VACNTs array with the regular pore (inter-VACNTs space) for better electrolyte accessibility; (2) ultra-fine SnO_2 nanoparticles, facilitating the Li^+ diffusion and enhancing the reversible electrochemical lithiation/delithiation reaction; (3) highly conductive VACNTs host for high-capacity SnO_2 materials (SnO_2-VACNTs core-shell structure), increasing conductivity and alleviating electrode pulverization from volume expansion; and (4) innate connection between VACNTs and current collector (binder-free anode), facilitating uninterrupted electron conduction during charge/discharge cycling. Therefore, the SnO_2-VACNTs are promising anode materials for high energy and power density LIBs, although the large initial irreversible capacity loss and cycle instability require further improvement.

4. Conclusions

VACNT arrays have been synthesized directly on 3D Ni foam using the PECVD method to develop free-standing, binder-free VACNTs anode materials. The high-capacity SnO_2-VACNTs core-shell anode was developed by coating the VACNTs wall with ultrafine SnO_2 nanoparticles using a wet-chemical method. The electrochemical properties of the SnO_2 and SnO_2-VACNTs anodes were measured using lithium-ion coin cells in a half-cell configuration. The core-shell structured SnO_2-VACNTs exhibited excellent Li^+ storage properties with a high specific capacity of ~1512 mAh g^{-1} after 100 cycles at a current rate of 0.1 A g^{-1}. The SnO_2-VACNTs anode also demonstrated long-term cycle stability for 200 cycles at a current density of 1 A g^{-1} with a reversible capacity of about 800 mAh g^{-1} with excellent coulombic efficiencies.

The excellent Li^+ storage properties of the SnO_2-VACNTs can be attributed to the ultra-fine SnO_2 particles (< 5 nm) that shortened the diffusion routes of Li^+ and mitigated the volume alteration by minimizing the strains during the Li^+ alloying and dealloying. Also, proper inter-tube distance between individual SnO_2-VACNTs buffered the volume instability and offered better electrolyte accessibility during the lithiation/delithiation process. Furthermore, the direct connection of VACNTs to the Ni foam current collector ensured an uninterrupted electron conducting path between the current collector and active material, thereby offering more efficient charge transport kinetics at the electrode/electrolyte interfaces. Furthermore, the as-synthesized SnO_2-VACNTs anode was assessed in a full cell by pairing with an NMC cathode to understand its practical applications. The strategy presented in this work for synthesizing the three-dimensional SnO_2-VACNTs anode material may pave the way for developing high-performance LIBs.

CRediT authorship contribution statement

Arun Thapa: Conceptualization, Methodology, Investigation, Formal analysis, Writing - original draft, Review & Editing. **Amin Rabiei Baboukani:** Methodology, Discussion, Review & Editing. **Prahald Siwakoti**: Investigation, Discussion, Review & Editing. **Katherine L. Jungjohann:** Investigation, Discussion, Review & Editing. **Chinaza E. Nwanno:** Investigation, Discussion, Review & Editing. **Jiandi Zhang:** Investigation, Discussion, Review & Editing. **Chunlei Wang:** Funding acquisition, Supervision, Review & Editing. **Hongwei Gao:** Funding acquisition, Supervision, Review & Editing. **Wenzhi Li:** Conceptualization, Methodology, Discussion, Validation, Funding acquisition, Supervision, Review & Editing.

Declaration of competing interest

The authors declare the following financial interests/personal relationships which may be considered as potential competing interests:

Wenzhi Li and Arun Thapa have a patent, "**Coated vertically aligned carbon nanotubes on nickel foam**" (US patent 11,476,464). https://patents.google.com/patent/US11476464B1/en).

Acknowledgment

Synthesis of vertically aligned carbon nanotubes (VACNTs), Tin Oxide nanoparticles (SnO_2), and SnO_2 coated VACNTs, characterization of VACNTs and SnO_2-VACNTs by Atomic Force Microscopy, Scanning Electron Microscopy, X-ray Diffraction, Thermogravimetry, Fourier Transform Infrared Spectroscopy, Raman Spectroscopy, fabrication of coin cells at Florida International University, and Cyclic Voltammetry and Charge/Discharge testing of the coin cells were supported by the National Science Foundation under grants 1506640, 2134375, and 2213923 to Florida International University.

Fabrication of coin cells at Montana State University, Electrochemical Impedance Spectroscopy, Charge/Discharge, and Cyclic Voltammetry tests of the cells, and post-analysis of electrodes of the cells by Scanning Electron Microscopy were supported by the financial support from the DEVCOM Army Research Laboratory (ARL) under Cooperative Agreement (CA) Number W911NF-20-2-0284. The views and conclusions contained in this document are those of the authors and should not be interpreted as representing the official policies, either expressed or implied, of the DEVCOM Army Research Laboratory or the U.S. Government. The U.S. Government is authorized to reproduce and distribute reprints for Government purposes notwithstanding any copyright notation hereon.

Transmission Electron Microscopy was performed at the Center for Integrated Nanotechnologies, an Office of Science User Facility operated for the U.S. Department of Energy (DOE) Office of Science. Sandia National Laboratories is a multi-mission laboratory managed and operated by National Technology and Engineering Solutions of Sandia, LLC., a wholly owned subsidiary of Honeywell International, Inc., for the U.S. DOE's National Nuclear Security Administration under contract DE-NA-0003525. This paper describes objective technical results and analysis. Any subjective views or opinions that might be expressed in the paper do not necessarily represent the views of the U.S. Department of Energy or the United States Government.

Post-analysis of electrodes by Scanning Electron Microscopy was performed at the Montana Nanotechnology Facility, a member of the National Nanotechnology Coordinated Infrastructure (NNCI), which is supported by the National Science Foundation (Grant # ECCS-2025391).

The authors would also like to acknowledge the support from the Advanced Materials Engineering Research Institutes (AMERI) at Florida International University (FIU).

Data availability

The raw/processed data required to reproduce these findings cannot be shared at this time as the data also forms part of an ongoing study.

References

1. M.V. Reddy, A. Mauger, C.M. Julien, A. Paolella, and K. Zaghib *Brief History of Early Lithium-Battery Development*. Materials, 2020. **13**. https://doi.org/10.3390/ma13081884
2. M. Li, J. Lu, Z. Chen, and K. Amine, *30 Years of Lithium-Ion Batteries*. **Advanced Materials**, **2018**. 30(33): p. 1800561. https://doi.org/10.1002/adma.201800561

3. T. Kim, W. Song, D.-Y. Son, L.K. Ono, and Y. Qi, *Lithium-ion batteries: outlook on present, future, and hybridized technologies.* **Journal of Materials Chemistry A**, **2019**. 7(7): p. 2942-2964. https://doi.org/10.1039/C8TA10513H

4. W. Cai, Y.-X. Yao, G.-L. Zhu, C. Yan, L.-L. Jiang, C. He, J.-Q. Huang, and Q. Zhang, *A review on energy chemistry of fast-charging anodes.* **Chemical Society Reviews**, **2020**. 49(12): p. 3806-3833. https://doi.org/10.1039/C9CS00728H

5. Y. Li, Y. Lu, P. Adelhelm, M.-M. Titirici, and Y.-S. Hu, *Intercalation chemistry of graphite: alkali metal ions and beyond.* **Chemical Society Reviews**, **2019**. 48(17): p. 4655-4687. https://doi.org/10.1039/C9CS00162J

6. B. Zhao, Z. Wang, S. Wang, J. Jiang, J. Si, S. Huang, Z. Chen, W. Li, and Y. Jiang, *Sandwiched spherical tin dioxide/graphene with a three-dimensional interconnected closed pore structure for lithium storage.* **Nanoscale**, **2018**. 10(34): p. 16116-16126. https://doi.org/10.1039/C8NR03776K

7. P. Wang, M. Gao, H. Pan, J. Zhang, C. Liang, J. Wang, P. Zhou, and Y. Liu, *A facile synthesis of Fe3O4/C composite with high cycle stability as anode material for lithium-ion batteries.* **Journal of Power Sources**, **2013**. 239: p. 466-474. https://doi.org/10.1016/j.jpowsour.2013.03.073

8. C.-L. Zhang, B.-R. Lu, F.-H. Cao, Z.-L. Yu, H.-P. Cong, and S.-H. Yu, *Hierarchically structured Co3O4@carbon porous fibers derived from electrospun ZIF-67/PAN nanofibers as anodes for lithium ion batteries.* **Journal of Materials Chemistry A**, **2018**. 6(27): p. 12962-12968. 10.1039/C8TA03397H

9. T. Chen, Y. Hu, B. Cheng, R. Chen, H. Lv, L. Ma, G. Zhu, Y. Wang, C. Yan, Z. Tie, Z. Jin, and J. Liu, *Multi-yolk-shell copper oxide@carbon octahedra as high-stability anodes for lithium-ion batteries.* **Nano Energy**, **2016**. 20: p. 305-314. https://doi.org/10.1016/j.nanoen.2015.12.024

10. F. Xie, M. Sun, X. Sheng, Q. Zhang, Z. Ling, S. Hao, F. Diao, and Y. Wang, *Graphene-wrapped Fe2TiO5 nanoparticles with enhanced performance as lithium-ion battery anode.* **Materials Letters**, **2024**. 358: p. 135877. https://doi.org/10.1016/j.matlet.2024.135877

11. S. Hao, X. Sheng, F. Xie, M. Sun, F. Diao, and Y. Wang, *Electrospun carbon nanofibers embedded with heterostructured NiFe2O4/Fe0.64Ni0.36 nanoparticles as an anode for high-performance lithium-ion battery.* **Journal of Energy Storage**, **2024**. 80: p. 110412. https://doi.org/10.1016/j.est.2023.110412

12. Y. Pang, J. Wang, J. Yang, F. Fang, D. Sun, and S. Zheng, *Fully reversible lithium storage of tin oxide enabled by self-doping and partial amorphization.* **Nanoscale**, **2019**. 11(27): p. 12915-12923. https://doi.org/10.1039/C9NR03445E

13. C.-M. Wang, W. Xu, J. Liu, J.-G. Zhang, L.V. Saraf, B.W. Arey, D. Choi, Z.-G. Yang, J. Xiao, and S. Thevuthasan, *In situ transmission electron microscopy observation of microstructure and phase evolution in a SnO2 nanowire during lithium intercalation.* **Nano Letters**, **2011**. 11(5): p. 1874-1880. https://doi.org/10.1021/nl200272n

14. R. Demir-Cakan, Y.-S. Hu, M. Antonietti, J. Maier, and M.-M. Titirici, *Facile One-Pot Synthesis of Mesoporous SnO2 Microspheres via Nanoparticles Assembly and Lithium*

Storage Properties. **Chemistry of Materials**, **2008**. 20(4): p. 1227-1229. https://doi.org/10.1021/cm7031288

15. Z. Chen, M. Zhou, Y. Cao, X. Ai, H. Yang, and J. Liu, *In Situ Generation of Few-Layer Graphene Coatings on SnO2-SiC Core-Shell Nanoparticles for High-Performance Lithium-Ion Storage.* **Advanced Energy Materials**, **2012**. 2(1): p. 95-102. https://doi.org/10.1002/aenm.201100464

16. B. Huang, X. Li, Y. Pei, S. Li, X. Cao, R.C. Massé, and G. Cao, *Novel Carbon-Encapsulated Porous SnO2 Anode for Lithium-Ion Batteries with Much Improved Cyclic Stability.* **Small**, **2016**. 12(14): p. 1945-1955. https://doi.org/10.1002/smll.201503419

17. X. Wang, X. Cao, L. Bourgeois, H. Guan, S. Chen, Y. Zhong, D.-M. Tang, H. Li, T. Zhai, L. Li, Y. Bando, and D. Golberg, *N-Doped Graphene-SnO2 Sandwich Paper for High-Performance Lithium-Ion Batteries.* **Advanced Functional Materials**, **2012**. 22(13): p. 2682-2690. https://doi.org/10.1002/adfm.201103110

18. L. Zhang, H.B. Wu, B. Liu, and X.W. Lou, *Formation of porous SnO2 microboxes via selective leaching for highly reversible lithium storage.* **Energy & Environmental Science**, **2014**. 7(3): p. 1013-1017. https://doi.org/10.1039/C3EE43305F

19. W. Yue, S. Jiang, W. Huang, Z. Gao, J. Li, Y. Ren, X. Zhao, and X. Yang, *Sandwich-structural graphene-based metal oxides as anode materials for lithium-ion batteries.* **Journal of Materials Chemistry A**, **2013**. 1(23): p. 6928-6933. https://doi.org/10.1039/C3TA11012E

20. X. Han, X. Wu, Y. Deng, J. Liu, J. Lu, C. Zhong, and W. Hu, *Ultrafine Pt Nanoparticle-Decorated Pyrite-Type CoS2 Nanosheet Arrays Coated on Carbon Cloth as a Bifunctional Electrode for Overall Water Splitting.* **Advanced Energy Materials**, **2018**. 8(24): p. 1800935. https://doi.org/10.1002/aenm.201800935

21. J.-H. Lee, G.-S. Kim, Y.-M. Choi, W.I. Park, J.A. Rogers, and U. Paik, *Comparison of multiwalled carbon nanotubes and carbon black as percolative paths in aqueous-based natural graphite negative electrodes with high-rate capability for lithium-ion batteries.* **Journal of power sources**, **2008**. 184(1): p. 308. https://doi.org/10.1016/j.jpowsour.2008.05.090

22. X.M. Liu, Z.D. Huang, S.W. Oh, B. Zhang, P.C. Ma, M.M. Yuen, and J.K. Kim, *Carbon nanotube (CNT)-based composites as electrode material for rechargeable Li-ion batteries: a review.* **Composites Science and Technology**, **2012**. 72(2): p. 121. https://doi.org/10.1016/j.compscitech.2011.11.019

23. W. Zhang, Y. Liu, Z.-q. Ye, M. Yang, Q. Luo, J. Dai, Q.-f. Wang, and L. Liu, *Porous nitrogen-doped FeP/C nanofibers as promising anode for potassium-ion batteries.* **Journal of Central South University**, **2023**. 30(10): p. 3248-3259. https://doi.org/10.1007/s11771-023-5380-y

24. C.E. Nwanno and W. Li, *Aligned carbon nanotubes for lithium-ion batteries: A review.* **Nano Research**, **2023**. 16(11): p. 12384-12410. https://doi.org/10.1007/s12274-023-6006-2

25. T. Li, S. Gao, K. Li, G. Liu, X. Sheng, D. Shang, L. Wu, S. Chen, Y. Wang, and S. Wu, *Tailoring the phase evolution of molybdenum-based nanocrystals in carbon nanofibers for*

enhanced performance of lithium-ion batteries. **Journal of Alloys and Compounds**, **2023**. 934: p. 168042. https://doi.org/10.1016/j.jallcom.2022.168042

26. W.-Q. Han and A. Zettl, *Coating Single-Walled Carbon Nanotubes with Tin Oxide.* **Nano Letters**, **2003**. 3(5): p. 681-683. https://doi.org/10.1021/nl034142d

27. J. Wang, X. Sheng, S. Hao, G. Liu, R. Cai, X. Xue, and Y. Wang, *Construction of Fe0.64Ni0.36@graphite nanoparticles via corrosion-like transformation from NiFe2O4 and surface graphitization in flexible carbon nanofibers to achieve strong wideband microwave absorption.* **Journal of Colloid and Interface Science**, **2024**. 657: p. 193-207. https://doi.org/10.1016/j.jcis.2023.11.145

28. L. Noerochim, J.Z. Wang, S.L. Chou, D. Wexler, and H.K. Liu, *Free-standing single-walled carbon nanotube/SnO2 anode paper for flexible lithium-ion batteries.* **Carbon**, **2012**. 50(3): p. 1289. https://doi.org/10.1016/j.carbon.2011.10.049

29. B. Zhang, J. Huang, and J.K. Kim, *Ultrafine Amorphous SnOx Embedded in Carbon Nanofiber/Carbon Nanotube Composites for Li-Ion and Na-Ion Batteries.* **Advanced Functional Materials**, **2015**. 25(32): p. 5222. https://doi.org/10.1002/adfm.201501498

30. C. Ma, W. Zhang, Y.-S. He, Q. Gong, H. Che, and Z.-F. Ma, *Carbon coated SnO 2 nanoparticles anchored on CNT as a superior anode material for lithium-ion batteries.* **Nanoscale**, **2016**. 8(7): p. 4121. https://doi.org/10.1039/C5NR07996A

31. B.J. Landi, M.J. Ganter, C.D. Cress, R.A. DiLeo, and R.P. Raffaelle, *Carbon nanotubes for lithium ion batteries.* **Energy & Environmental Science**, **2009**. 2(6): p. 638. https://doi.org/10.1039/B904116H

32. L. Sun, X. Wang, R.A. Susantyoko, and Q. Zhang, *High performance binder-free Sn coated carbon nanotube array anode.* **Carbon**, **2015**. 82: p. 282-287. https://doi.org/10.1016/j.carbon.2014.10.072

33. R.A. Susantyoko, X. Wang, L. Sun, K.L. Pey, E. Fitzgerald, and Q. Zhang, *Germanium coated vertically-aligned multiwall carbon nanotubes as lithium-ion battery anodes.* **Carbon**, **2014**. 77: p. 551-559. https://doi.org/10.1016/j.carbon.2014.05.060

34. Y. Fan, Q. Zhang, Q. Xiao, X. Wang, and K. Huang, *High performance lithium ion battery anodes based on carbon nanotube–silicon core–shell nanowires with controlled morphology.* **Carbon**, **2013**. 59: p. 264-269. https://doi.org/10.1016/j.carbon.2013.03.017

35. J. Xia, L. Liu, S. Jamil, J. Xie, H. Yan, Y. Yuan, Y. Zhang, S. Nie, J. Pan, X. Wang, and G. Cao, *Free-standing SnS/C nanofiber anodes for ultralong cycle-life lithium-ion batteries and sodium-ion batteries.* **Energy Storage Materials**, **2019**. 17: p. 1-11. https://doi.org/10.1016/j.ensm.2018.08.005

36. A. Thapa, S. Neupane, R. Guo, K.L. Jungjohann, D. Pete, and W. Li, *Direct growth of vertically aligned carbon nanotubes on stainless steel by plasma enhanced chemical vapor deposition.* **Diamond and Related Materials**, **2018**. 90: p. 144. https://doi.org/10.1016/j.diamond.2018.10.012

37. S. Talapatra, S. Kar, S.K. Pal, R. Vajtai, L. Ci, P. Victor, M.M. Shaijumon, S. Kaur, O. Nalamasu, and P.M. Ajayan, *Direct growth of aligned carbon nanotubes on bulk metals.* **Nature Nanotechnology**, **2006**. 1(2): p. 112-116. https://doi.org/10.1038/nnano.2006.56

38. E. Piperopoulos, L. Calabrese, A. Khaskhoussi, E. Proverbio, and C. Milone *Thermo-Physical Characterization of Carbon Nanotube Composite Foam for Oil Recovery Applications*. Nanomaterials, 2020. **10**. https://doi.org/10.3390/nano10010086

39. L. Noerochim, J.-Z. Wang, S.-L. Chou, H.-J. Li, and H.-K. Liu, *SnO2-coated multiwall carbon nanotube composite anode materials for rechargeable lithium-ion batteries.* **Electrochimica Acta**, **2010**. 56(1): p. 314-320. https://doi.org/10.1016/j.electacta.2010.08.078

40. R.S. Hsu, D. Higgins, and Z. Chen, *Tin-oxide-coated single-walled carbon nanotube bundles supporting platinum electrocatalysts for direct ethanol fuel cells.* **Nanotechnology**, **2010**. 21(16): p. 165705. https://doi.org/10.1088/0957-4484/21/16/165705

41. M.S. Dresselhaus, G. Dresselhaus, R. Saito, and A. Jorio, *Raman spectroscopy of carbon nanotubes.* **Physics reports**, **2005**. 409(2): p. 47. https://doi.org/10.1016/j.physrep.2004.10.006

42. Z. Xiong, Y.S. Yun, and H.-J. Jin *Applications of Carbon Nanotubes for Lithium Ion Battery Anodes*. Materials, 2013. **6**, 1138-1158. https://doi.org/10.3390/ma6031138

43. C. Garau, A. Frontera, D. Quiñonero, A. Costa, P. Ballester, and P.M. Deyà, *Lithium diffusion in single-walled carbon nanotubes: a theoretical study.* **Chemical Physics Letters**, **2003**. 374(5): p. 548-555. https://doi.org/10.1016/S0009-2614(03)00748-6

44. K.M. Lee, D.J. Lee, and H. Ahn, *XRD and TEM studies on tin oxide (II) nanoparticles prepared by inert gas condensation.* **Materials Letters**, **2004**. 58(25): p. 3122. https://doi.org/10.1016/j.matlet.2004.06.002

45. T.W. Ebbesen, H. Hiura, M.E. Bisher, M.M. Treacy, J.L. Shreeve-Keyer, and R.C. Haushalter, *Decoration of carbon nanotubes.* **Advanced Materials**, **1996**. 8(2): p. 155. https://doi.org/10.1002/adma.19960080212

46. K. Balasubramanian and M. Burghard, *Chemically functionalized carbon nanotubes.* **small**, **2005**. 1(2): p. 180. https://doi.org/10.1002/smll.200400118

47. R. Pandiyan, S. Mahalingam, and Y.H. Ahn, *Antibacterial and photocatalytic activity of hydrothermally synthesized SnO2 doped GO and CNT under visible light irradiation.* **Journal of Photochemistry and Photobiology B: Biology**, **2019**. 191: p. 18. https://doi.org/10.1016/j.jphotobiol.2018.12.007

48. Z. Ling, F. Diao, X. Sheng, T. Li, R. Cai, and Y. Wang, *Chemical reaction and phase transformation mechanism of electrospun iron (III) acetylacetonate-polyacrylonitrile fibers during pre-oxidation process.* **Chemical Physics Letters**, **2023**. 832: p. 140866. https://doi.org/10.1016/j.cplett.2023.140866

49. F. Xie, X. Sheng, Z. Ling, S. Hao, Q. Zhang, M. Sun, G. Liu, F. Diao, and Y. Wang, *Flexible electrospun iron/manganese-based compounds/carbon fibers: Phase transformation and electrochemical properties.* **Electrochimica Acta**, **2023**. 470: p. 143288. https://doi.org/10.1016/j.electacta.2023.143288

50. S. Motshekga, S.K. Pillai, and S.S. Ray, *Conventional wet impregnation versus microwave-assisted synthesis of SnO 2/CNT composites.* **Journal of Nanoparticle Research**, **2011**. 13(3): p. 1093. https://doi.org/10.1007/s11051-010-0098-9

51. J. Zhu, Z. Lu, S. Aruna, D. Aurbach, and A. Gedanken, *Sonochemical synthesis of SnO2 nanoparticles and their preliminary study as Li insertion electrodes.* **Chemistry of Materials**, **2000**. 12(9): p. 2557. https://doi.org/10.1021/cm990683l

52. B. Huang, J. Yang, Y. Zou, L. Ma, and X. Zhou, *Sonochemical synthesis of SnO2/carbon nanotubes encapsulated in graphene sheets composites for lithium ion batteries with superior electrochemical performance.* **Electrochimica Acta**, **2014**. 143: p. 63-69. https://doi.org/10.1016/j.electacta.2014.07.119

53. V. Kumar, V. Kumar, S. Som, J.H. Neethling, E. Olivier, O.M. Ntwaeaborwa, and H.C. Swart, *The role of surface and deep-level defects on the emission of tin oxide quantum dots.* **Nanotechnology**, **2014**. 25(13): p. 135701. https://doi.org/10.1088/0957-4484/25/13/135701

54. X. Liu, Y. Jiang, K. Li, F. Xu, P. Zhang, and Y. Ding, *Electrospun free-standing N-doped C@SnO2 anode paper for flexible Li-ion batteries.* **Materials Research Bulletin**, **2019**. 109: p. 41-48. https://doi.org/10.1016/j.materresbull.2018.09.023

55. Q. Tian, F. Zhang, W. Zhang, and L. Yang, *Non-smooth carbon coating porous SnO2 quasi-nanocubes towards high lithium storage.* **Electrochimica Acta**, **2019**. 307: p. 393-402. https://doi.org/10.1016/j.electacta.2019.04.004

56. B. Zhou, S. Yang, L. Wu, W. Wu, W. Wei, L. Chen, H. Zhang, J. Pan, and X. Xiong, *Amorphous carbon framework stabilized SnO2 porous nanowires as high performance Li-ion battery anode materials.* **RSC Advances**, **2015**. 5(62): p. 49926-49932. https://doi.org/10.1039/C5RA05372B

57. D. Hernandez, F. Mendoza, E. Febus, B.R. Weiner, and G. Morell, *Binder free SnO2-CNT composite as anode material for Li-Ion battery.* **Journal of Nanotechnology**, **2014**. 2014: p. 381273. https://doi.org/10.1155/2014/381273

58. J. Zhang, Y. Zhu, C. Cao, and F.K. Butt, *Microwave-assisted and large-scale synthesis of SnO 2/carbon-nanotube hybrids with high lithium storage capacity.* **RSC Advances**, **2015**. 5(72): p. 58568. https://doi.org/10.1039/C5RA10314B

59. J. Zhao, A. Buldum, J. Han, and J. Ping Lu, *First-Principles Study of Li-Intercalated Carbon Nanotube Ropes.* **Physical Review Letters**, **2000**. 85(8): p. 1706-1709. https://doi.org/10.1103/PhysRevLett.85.1706

60. K. Nishidate and M. Hasegawa, *Energetics of lithium ion adsorption on defective carbon nanotubes.* **Physical Review B**, **2005**. 71(24): p. 245418. https://doi.org/10.1103/PhysRevB.71.245418

61. B.J. Landi, M.J. Ganter, C.D. Cress, R.A. DiLeo, and R.P. Raffaelle, *Carbon nanotubes for lithium ion batteries.* **Energy & Environmental Science**, **2009**. 2(6): p. 638-654. https://doi.org/10.1039/B904116H

62. H. Xu, L. Shi, Z. Wang, J. Liu, J. Zhu, Y. Zhao, M. Zhang, and S. Yuan, *Fluorine-Doped Tin Oxide Nanocrystal/Reduced Graphene Oxide Composites as Lithium Ion Battery*

Anode Material with High Capacity and Cycling Stability. **ACS Applied Materials & Interfaces**, **2015**. 7(49): p. 27486-27493. https://doi.org/10.1021/acsami.5b09538

63. F. Mueller, D. Bresser, V.S.K. Chakravadhanula, and S. Passerini, *Fe-doped SnO2 nanoparticles as new high capacity anode material for secondary lithium-ion batteries.* **Journal of Power Sources**, **2015**. 299: p. 398-402. https://doi.org/10.1016/j.jpowsour.2015.08.018

64. Y.F. Zhukovskii, E.A. Kotomin, P. Balaya, and J. Maier, *Enhanced interfacial lithium storage in nanocomposites of transition metals with LiF and Li2O: Comparison of DFT calculations and experimental studies.* **Solid State Sciences**, **2008**. 10(4): p. 491-495. https://doi.org/10.1016/j.solidstatesciences.2007.12.030

65. M.R. Smith, P.L. Johnson, and D. Teeters, *Interfacial storage of lithium in the nanostructure of SnO2 nanobaskets for capacities exceeding theoretical values.* **Solid State Ionics**, **2012**. 225: p. 680-684. https://doi.org/10.1016/j.ssi.2011.11.022

66. L. Ji, Z. Tan, T. Kuykendall, E.J. An, Y. Fu, V. Battaglia, and Y. Zhang, *Multilayer nanoassembly of Sn-nanopillar arrays sandwiched between graphene layers for high-capacity lithium storage.* **Energy & Environmental Science**, **2011**. 4(9): p. 3611. https://doi.org/10.1039/C1EE01592C

67. W. Lu, A. Goering, L. Qu, and L. Dai, *Lithium-ion batteries based on vertically-aligned carbon nanotube electrodes and ionic liquid electrolytes.* **Physical Chemistry Chemical Physics**, **2012**. 14(35): p. 12099. https://doi.org/10.1039/c2cp40726d

68. Z. Wang, G. Chen, and D. Xia, *Coating of multi-walled carbon nanotube with SnO2 films of controlled thickness and its application for Li-ion battery.* **Journal of power sources**, **2008**. 184(2): p. 432. https://doi.org/10.1016/j.jpowsour.2008.03.028

69. J. Gao, R. Huang, D. Yang, K. Wu, D. Xiong, Z. Feng, M. He, and Y. Feng, *Molybdenum-fluorine-doped SnO2 nanoparticles based on 3D interconnected carbon structure as matrix as high-performance lithium-ion anode material.* **Ionics**, **2022**. 28(10): p. 4587-4597. https://doi.org/10.1007/s11581-022-04717-x

70. Y. Guo, Y. Hu, Q. Zhang, G. Ruan, Y. Mao, H. Zhang, R. Wang, P. Zhao, M. Li, H. Tang, D. Zhang, L. Xu, M. Jin, K. Ding, and B. Wang, *Fabrication of SnO2 micron-rods embedding in 3D composite of graphene oxide@MWNTs as high-performance anode for lithium-ion batteries.* **Journal of Energy Storage**, **2023**. 74: p. 109479. https://doi.org/10.1016/j.est.2023.109479

71. C. Zhao, Z. Wei, J. Zhang, P. He, X. Huang, X. Duan, D. Jia, and Y. Zhou, *Ultrafine SnO2 nanoparticles on delaminated MXene nanosheets as an anode for lithium-ion batteries.* **Journal of Alloys and Compounds**, **2022**. 907: p. 164428. https://doi.org/10.1016/j.jallcom.2022.164428

72. D. Jiang, C. Wang, L. Sun, X. Xu, B. Wu, and X. Chen, *Facile Hydrothermal Synthesis of SnO2 Nanoparticles with Enhanced Lithium Storage Performance.* **Chemistry Letters**, **2017**. 46(11): p. 1639-1642. https://doi.org/10.1246/cl.170757

73. Z. Shen, Y. Hu, Y. Chen, X. Zhang, K. Wang, and R. Chen, *Tin nanoparticle-loaded porous carbon nanofiber composite anodes for high current lithium-ion batteries.* **Journal of Power Sources**, **2015**. 278: p. 660-667. https://doi.org/10.1016/j.jpowsour.2014.12.106

74. B. Han, W. Zhang, D. Gao, C. Zhou, K. Xia, Q. Gao, and J. Wu, *Encapsulating tin oxide nanoparticles into holey carbon nanotubes by melt infiltration for superior lithium and sodium ion storage.* **Journal of Power Sources**, **2020**. 449: p. 227564. https://doi.org/10.1016/j.jpowsour.2019.227564

75. F. Zoller, K. Peters, P.M. Zehetmaier, P. Zeller, M. Döblinger, T. Bein, Z.k. Sofer, and D. Fattakhova-Rohlfing, *Making Ultrafast High-Capacity Anodes for Lithium-Ion Batteries via Antimony Doping of Nanosized Tin Oxide/Graphene Composites.* **Advanced Functional Materials**, **2018**. 28(23): p. 1706529. https://doi.org/10.1002/adfm.201706529

76. F. Kenji, K. Kazuhiko, I. Kennichi, and Y. Masaki, *Foliated natural graphite as the anode material for rechargeable lithium-ion cells.* **Journal of Power Sources**, **1997**. 69(1): p. 165-168. https://doi.org/10.1016/S0378-7753(97)02568-8

77. S. Zhang and P. Shi, *Electrochemical impedance study of lithium intercalation into MCMB electrode in a gel electrolyte.* **Electrochimica Acta**, **2004**. 49(9): p. 1475-1482. https://doi.org/10.1016/j.electacta.2003.10.033

78. D. Chen, S. Sun, G. Yu, L. Qin, W. Wang, M. Jiang, and J. Chen, *In-situ thermally fabricated porous and heterogeneous yolk-shell selenides wrapped in carbon as anode for high-performance hybrid lithium-ion capacitors.* **Carbon**, **2020**. 166: p. 91-100. https://doi.org/10.1016/j.carbon.2020.05.008

79. L.G. Bulusheva, A.V. Okotrub, A.G. Kurenya, H. Zhang, H. Zhang, X. Chen, and H. Song, *Electrochemical properties of nitrogen-doped carbon nanotube anode in Li-ion batteries.* **Carbon**, **2011**. 49(12): p. 4013. https://doi.org/10.1016/j.carbon.2011.05.043

80. J. Guo, A. Sun, X. Chen, C. Wang, and A. Manivannan, *Cyclability study of silicon–carbon composite anodes for lithium-ion batteries using electrochemical impedance spectroscopy.* **Electrochimica Acta**, **2011**. 56(11): p. 3981-3987. https://doi.org/10.1016/j.electacta.2011.02.014

81. J.Y. Song, H.H. Lee, Y.Y. Wang, and C.C. Wan, *Two- and three-electrode impedance spectroscopy of lithium-ion batteries.* **Journal of Power Sources**, **2002**. 111(2): p. 255-267. https://doi.org/10.1016/S0378-7753(02)00310-5

82. K.-H. Chen, K.N. Wood, E. Kazyak, W.S. LePage, A.L. Davis, A.J. Sanchez, and N.P. Dasgupta, *Dead lithium: mass transport effects on voltage, capacity, and failure of lithium metal anodes.* **Journal of Materials Chemistry A**, **2017**. 5(23): p. 11671-11681. https://doi.org/10.1039/C7TA00371D

83. C.-H. Kim, S.-I. Pyun, and J.-H. Kim, *An investigation of the capacitance dispersion on the fractal carbon electrode with edge and basal orientations.* **Electrochimica Acta**, **2003**. 48(23): p. 3455-3463. https://doi.org/10.1016/S0013-4686(03)00464-X

84. V.J. Ovejas and A. Cuadras *Impedance Characterization of an LCO-NMC/Graphite Cell: Ohmic Conduction, SEI Transport and Charge-Transfer Phenomenon*. Batteries, 2018. **4**. https://doi.org/10.3390/batteries4030043

85. L. Wang, B. Zhang, Y. Hu, X. Li, and T. Zhao, *Failure analysis of LiNi0·83Co0·12Mn0·05O2/graphite–SiOx pouch batteries cycled at high temperature.*

Journal of Power Sources, **2021**. 482: p. 228978. https://doi.org/10.1016/j.jpowsour.2020.228978

86. M. Ma, A.N. Mansour, J.K. Ko, G.H. Waller, and C.E. Hendricks, *Characterization of Li Diffusion and Solid Electrolyte Interface for Li4Ti5O12 Electrode Cycled with an Organosilicon Additive Electrolyte.* **Journal of The Electrochemical Society**, **2020**. 167(11): p. 110549. https://doi.org/10.1149/1945-7111/aba5d3

87. I.A. Courtney and J. Dahn, *Electrochemical and in situ X-ray diffraction studies of the reaction of lithium with tin oxide composites.* **Journal of the Electrochemical Society**, **1997**. 144(6): p. 2045. https://doi.org/10.1149/1.1837740

88. T. Brousse, R. Retoux, U. Herterich, and D.M. Schleich, *Thin-Film Crystalline SnO2-Lithium Electrodes.* **Journal of The Electrochemical Society**, **1998**. 145(1): p. 1. https://doi.org/10.1149/1.1838201

89. R.A. Huggins and W.D. Nix, *Decrepitation model for capacity loss during cycling of alloys in rechargeable electrochemical systems.* **Ionics**, **2000**. 6(1): p. 57-63. https://doi.org/10.1007/BF02375547

90. X. Li, X. Sun, X. Hu, F. Fan, S. Cai, C. Zheng, and G.D. Stucky, *Review on comprehending and enhancing the initial Coulombic efficiency of anode materials in lithium-ion/sodium-ion batteries.* **Nano Energy**, **2020**. 77: p. 105143. https://doi.org/10.1016/j.nanoen.2020.105143

91. C. Zhao, Z. Yang, X. Zhou, Z. Hao, J. Chen, Z. Wang, X. Chen, X. Wu, L. Li, L. Li, L. Jiao, and S. Chou, *Recent Progress on Electrolyte Boosting Initial Coulombic Efficiency in Lithium-Ion Batteries.* **Advanced Functional Materials**, **2024**. 34(5): p. 2303457. https://doi.org/10.1002/adfm.202303457

92. M. Ge, C. Cao, G.M. Biesold, C.D. Sewell, S.-M. Hao, J. Huang, W. Zhang, Y. Lai, and Z. Lin, *Recent Advances in Silicon-Based Electrodes: From Fundamental Research toward Practical Applications.* **Advanced Materials**, **2021**. 33(16): p. 2004577. https://doi.org/10.1002/adma.202004577

Checklist for battery-related manuscripts submitted to

Journal of Power Sources / Journal of Power Sources Advances

When submitting a manuscript to *Journal of Power Sources* or *Journal of Power Sources Advances* dealing with any type of battery, authors are requested to include the following checklist as supplemental information.

Please, confirm that each information in Table 1 is present in the manuscript by checking the corresponding box.

Table 1. Information Checklist	
Electrodes and Cells	
Cell type and configuration	x
Electrodes’ geometry and size	x
Description of electrode preparation (including post-coating treatments such as compression/calendering)	x
Electrode’s active material areal mass loading (or areal capacity)	x
Composition of the electrodes including supplier and purity of pursued components	x
Apparent electrode density (calculated as the ratio of areal mass loading and thickness)	x
Current collector type and thickness (if not flat, also weight)	x
Separator type & thickness	x
Electrolyte composition and volume/weight used in the cell	x
Ratio of N/P capacities (for full cells only)	
Areal capacity of the counter electrode (for half cells only)	x
Electrolyte/Sulfur (E/S) weight ratio (for Li-S batteries only)	
Thickness and carbon mass loading of the air electrode (for metal air batteries only)	
Electrochemical testing	
Testing temperature	x
Voltage (or potential) range	x
Theoretical capacity and specified C-rate	x
Charge / discharge program (CC, CV, combination)	x
C-rate for each electrochemical measurement	x
Initial electrochemical profile	x
Cycling performance	x
Coulombic efficiency associated with cycling data	x
Additional checklist for redox flow batteries	
Active material concentration in anolyte and catholyte	x
Electrode material (e.g., carbon felt, metal mesh) and thickness	x
Flow field type, if any	
Anolyte / catholyte flow rate	
Active material solubility limits (both redox forms) for anolyte and catholyte	

Please, indicate in Table 2 the electrochemical data reported in the manuscript by checking the corresponding box.

Table 2. Performance Reporting

Cell type		Coin cell	x	Pouch cell		Other	
Cell configuration		2-electrode cell	x	3-electrode cell			
Mass loading of active material		Coin cell		Pouch cell		Other	
	<2 mg cm^{-2}	x					
	2-5 mg cm^{-2}						
	5-8 mg cm^{-2}						
	>8 mg cm^{-2}						
Number of cycles at ≤1C (Note: We tested according to active materials wt. @0.1 A/g).		Metal anode/battery (incl. half cells)		Full cell			
	<50						
	50-200	x					
	>200						
Number of cycles at >1C (Note: We tested according to active materials wt. @ 1 A/g).		Metal anode/battery (incl. half cells)		Full cell			
	<100						
	100-300	x					
	300-500						
	>500						

If you answered with NA to any request, please, explain the reason below:

References:

J. Li *et al*, *Good practice guide for papers on batteries for the Journal of Power Sources*, Journal of Power Sources 452 (2020) 227824. DOI: 10.1016/j.jpowsour.2020.227824

A.K. Stephan, *Standardized Battery Reporting Guidelines*, Joule 5, (2021) 1-2. DOI: 10.1016/j.joule.2020.12.026